



### 저작자표시-비영리-동일조건변경허락 2.0 대한민국

이용자는 아래의 조건을 따르는 경우에 한하여 자유롭게

- 이 저작물을 복제, 배포, 전송, 전시, 공연 및 방송할 수 있습니다.
- 이차적 저작물을 작성할 수 있습니다.

다음과 같은 조건을 따라야 합니다:



저작자표시. 귀하는 원저작자를 표시하여야 합니다.



비영리. 귀하는 이 저작물을 영리 목적으로 이용할 수 없습니다.



동일조건변경허락. 귀하가 이 저작물을 개작, 변형 또는 가공했을 경우에는, 이 저작물과 동일한 이용허락조건하에서만 배포할 수 있습니다.

- 귀하는, 이 저작물의 재이용이나 배포의 경우, 이 저작물에 적용된 이용허락조건을 명확하게 나타내어야 합니다.
- 저작권자로부터 별도의 허가를 받으면 이러한 조건들은 적용되지 않습니다.

저작권법에 따른 이용자의 권리는 위의 내용에 의하여 영향을 받지 않습니다.

이것은 [이용허락규약\(Legal Code\)](#)을 이해하기 쉽게 요약한 것입니다.

[Disclaimer](#)

공학박사학위논문

폐열 회수 장치를 이용한 대형 직렬형 하이브리드  
전기 자동차의 연비 향상에 관한 연구

Study on the Improvement in Fuel Economy with the Waste  
Heat Recovery System in Heavy-duty Series HEVs

2013 년 8 월

서울대학교 대학원

기계항공공학부

정 대 봉

폐열 회수 장치를 이용한 대형 직렬형 하이브리드  
전기 자동차의 연비 향상에 관한 연구

Study on the Improvement in Fuel Economy with the Waste  
Heat Recovery System in Heavy-duty Series HEVs

지도교수 민 경 덕

이 논문을 공학박사 학위논문으로 제출함

2013 년 8 월

서울대학교 대학원

기계항공공학부

정 대 봉

정대봉의 공학박사 학위논문을 인준함

2013 년 6 월

위 원 장 이 경 수 (인)

부위원장 민 경 덕 (인)

위 원 차 석 원 (인)

위 원 송 한 호 (인)

위 원 박 성 진 (인)

## Acknowledgements

First of all, I would like to express my respect and gratitude to my advisor, Professor Kyoungdoug Min. His guidance, assistance, patience, and encouragement have been of enormous importance to my research and the completion of the thesis. In addition, my knowledge and personality were grown up with his invaluable advices. I would also like to thank my other committee members, Professor Kyoung-su Lee, Professor Suk-won Cha, Professor Han Ho song, and Professor Sungjin Park, for their helpful advices.

I had joyful and impressive lab life with my labmates. Especially, I would like thank to BCS members, Sangkyu Kang, Junhyun Cho, Jaeman Park, and Namho Kim. They gave me deep friendship and I never forget them forever. Also, I would like thank to HEV team member, Minjae Kim, Minje Park, Hyuncheol Ahn. They gave me huge help to complete my thesis. I extended my thanks to Junyong Lee, Wona Park, Joohan Kim, Jeongwoo Lee, Seungha Lee, Gyujin Kim, Seunghyun Lee, Dongsu Kim, Seokwon Cho, Jinhee Kim, Jungyeon Lee, Yoonwoo Lee, Insuk Ko, Jongwon Jung, and Cheolhwan Lee. I would like thank former my team members, Sungwoo Cho, and Jinwoo Yong.

Finally, I would like to present my earnest respect and gratitude to my parents, Changhae Jung and Seongrye Ree, for their great sacrifice, thoughtful consideration, and endless love. I extended my thanks to my lovely sister, Hyemin Jung for her thoughtful consideration.

## **Abstract**

# **Study on the Improvement in Fuel Economy with the Waste Heat Recovery System in Heavy-duty Series HEVs**

Daebong Jung

Department of Mechanical and Aerospace Engineering

The Graduate School

Seoul National University

Recently, the oil price hike and the stringent emission regulations are great issues in the automotive industry. Thus, there are efforts to develop high efficiency and low emission vehicles. These efforts achieved outstanding improvements. However, in conventional powertrain systems such as an internal combustion engine and a hybrid powertrain, maximum fuel conversion efficiency is limited as 40 %. In other words, 60 % of fuel energy is rejected into coolant and exhaust gas. Thus, there is huge challenge to improve fuel conversion efficiency more than theoretical limitation without using rejected energy. The Waste Heat Recovery System (WHRS) is a kind of technologies which use wasted energy to drive vehicles or to generate electric energy. In this paper, to improve fuel economy of series hybrid electric vehicle (SHEV), Rankine cycle is adapted as WHRS and is applied to the target vehicle.

First, thermodynamic analysis on various heat sources was conducted. The exhaust gas, the coolant and the charged air were taken into account as heat sources. By this analysis, exergy and available energy of heat sources according to the engine operation were analyzed. Based on this result, the condition of the

engine operation for WHRS operation was investigated. Moreover, possibility to be used as heat source for the WHRS according to the engine operation is analyzed.

Second, optimizing a design and a control of the WHRS for applying to the target system was conducted. The cycle efficiency according to various working fluids was investigated to determine optimal working fluid. Then, a turbine was designed with consideration of the working condition and the limitation. In addition, optimization of geometrical characteristics of turbine and heat exchanger was conducted. To optimize the control algorithm, Dynamic Programming (DP) which is global optimization method was used and Equivalent Consumption Minimization Strategy (ECMS) which is local optimization method was implemented for application to real system. In addition, simple on/off control strategy, thermostatic control strategy, was implemented and applied, too.

Third, because the exhaust gas state is important to the WHRS, the transient behavior of exhaust gas at cold start was estimated by using 1-D engine model and engine thermal management model. Based on the results, it was known that the WHRS should be operated at 80 seconds after the engine started.

In this research, the design and the optimization method to apply WHRS to vehicle was suggested. This method can be adapted to design and control new hybrid power system and achieve the most efficient system.

Keywords: Waste heat recovery system (WHRs), organic Rankine cycle (ORC), optimal control, optimization, heavy-duty series hybrid electric vehicle (HSHEV)

Student Number: 2007-20848

# Contents

<b>Chapter 1. Introduction .....</b>	<b>1</b>
<b>1.1 Motivation .....</b>	<b>1</b>
<b>1.2 Literature Review .....</b>	<b>4</b>
1.2.1 Thermo-electric generation (TEG) .....	4
1.2.2 Turbo-compound.....	5
1.2.3 Rankine cycle.....	7
<b>1.3 Objective.....</b>	<b>14</b>
<b>Chapter 2. Thermodynamic analysis on the heat sources .</b>	<b>17</b>
<b>2.1 Exergy and available energy .....</b>	<b>17</b>
<b>2.2 Engine and WHRS operation in SHEV.....</b>	<b>28</b>
<b>Chapter 3. Development and validation of models .....</b>	<b>30</b>
<b>3.1 System configuration.....</b>	<b>30</b>
<b>3.2 Powertrain model .....</b>	<b>32</b>
3.2.1 Engine model .....	32
3.2.1.1 1-D engine model.....	33
3.2.1.2 Thermal management model.....	43
3.2.1.3 0-D engine model.....	49
3.2.2 Motor and generator (M/G) models.....	50
3.2.3 Battery model.....	52

3.2.4 Model of waste heat recovery .....	63
3.2.4.1 Heat exchanger model.....	63
3.2.4.2 Turbine model .....	67
3.2.4.3 Condenser and pump models .....	70
<b>3.3 Vehicle model .....</b>	<b>71</b>
3.3.1 Vehicle longitudinal dynamic model .....	71
3.3.2 Regenerative braking algorithm.....	73
<b>3.4 Validation of vehicle model.....</b>	<b>77</b>
<b>Chapter 4. Optimization .....</b>	<b>82</b>
<b>4.1 Optimization of system design.....</b>	<b>82</b>
4.1.1 Optimization of the working fluid type .....	82
4.1.2 Suggestion of optimizing the working condition.....	92
4.1.3 Optimization of the geometric specification.....	95
4.1.3.1 Turbine .....	95
4.1.3.1.1 Design of the single-stage turbine .....	98
4.1.3.1.2 Design of the multi-stage turbine .....	110
4.1.3.2 Heat exchanger.....	117
4.1.4 Simulation on the WHRS model.....	124
<b>4.2 Optimization of system control .....</b>	<b>126</b>
4.2.1 Dynamic programming .....	126
4.2.2 ECMS .....	129
4.2.3 Simple strategy (Thermostatic control strategy).....	132
<b>Chapter 5. Simulation results .....</b>	<b>134</b>

<b>5.1 Results of engine transient simulation.....</b>	<b>134</b>
<b>5.2 Results of vehicle simulation .....</b>	<b>137</b>
5.2.1 Test cycles.....	137
5.2.2 Results of Dynamic Programming.....	140
5.2.3 Results of ECMS application.....	150
5.2.4 Results of thermostatic control strategy.....	160
<b>Chapter 6. Conclusion.....</b>	<b>162</b>

## List of Tables

Table 1. Results of previous studied concerned with various Rankine cycle applications [36] .....	13
Table 2. The specifications of the target vehicle .....	31
Table 3. Parameters for the 1-D engine model .....	39
Table 4. Comparison between experiment and simulation (1200 rpm – 100 % load, fuel injection 5.24 g/s).....	40
Table 5. Comparison between experiment and simulation (1400 rpm – 100 % load, fuel injection 6.89 g/s).....	40
Table 6. Comparison between experiment and simulation (1600 rpm – 100% load, fuel injection 7.62 g/s).....	41
Table 7. Comparison between experiment and simulation (1800 rpm – 100% load, fuel injection 8.89 g/s).....	41
Table 8. Comparison between experiment and simulation (2000 rpm – 100% load, fuel injection 9.55 g/s).....	42
Table 9. Comparison between experiment and simulation (2300 rpm – 100% load, fuel injection 10.18 g/s).....	42
Table 10. Battery parameters.....	59
Table 11. Validation results of energy balance of each component.....	80
Table 12. Properties of various working fluids at 1 atm, 393.15 K.....	87
Table 13. The assumed working condition at the condenser.....	91

Table 14. Optimization cases of the turbine geometry (diameter).....	98
Table 15. Optimal design of the single turbine (R245fa) .....	104
Table 16. Optimal design of the single turbine (water) .....	109
Table 17. The results of the multi-stage turbine design (R245fa, outlet temperature 318.1 K) .....	111
Table 18. The results of the multi-stage turbine design (R245fa, outlet temperature 352.4 K) .....	113
Table 19. Optimal combination of multi stage turbine for R245fa.....	115
Table 20. The results of the multi-stage turbine design (Water, outlet dryness 85 %).....	116
Table 21. The results of the multi-stage turbine design (Water, outlet dryness 100 %).....	116
Table 22. Optimal combination of multi stage turbine for water .....	117
Table 23. The characteristics of various plat fin type heat exchanger .....	118
Table 24. Design results of type 5.3 for R245fa.....	121
Table 25. Design results of type 14.77 for R245fa.....	122
Table 26. Design results of type 10.27T for R245fa.....	122
Table 27. Design results of type 30.33T for R245fa.....	123
Table 28. Design result of the heat exchanger for water .....	124

Table 29. Simulation results of turbine and heat exchanger combined model .	125
Table 30. Specifications of the test cycles.....	140
Table 31. The results of Dynamic Programming.....	149
Table 32. $SC_{eng}$ values according to test cycles and configurations.....	150
Table 33. Results of forward simulation with ECMS.....	159
Table 34. Results of forward simulation with thermostatic control strategy ....	161

## List of Figures

Figure 1. Regulation of fuel economy .....	1
Figure 2. Regulation of emission .....	2
Figure 3. Energy flow in vehicles.....	3
Figure 4. Typical TEG module [3] .....	4
Figure 5. Turbo-compound system diagram [7] .....	6
Figure 6. A schematic of the swash plate type expander [30] .....	10
Figure 7. A schematic of the scroll type expander [31] .....	10
Figure 8. A schematic of the rotary vane type expander [32].....	11
Figure 9. A schematic of the gerotor type expander [33] .....	11
Figure 10. Temperature of the charged air.....	20
Figure 11. Mass flow rate of charged air .....	20
Figure 12. Exergy of charged air .....	21
Figure 13. Available energy of charged air.....	21
Figure 14. Temperature of exhaust gas.....	24
Figure 15. Mass flow rate of exhaust gas .....	24
Figure 16. Exergy of exhaust gas .....	25

Figure 17. Available energy of exhaust gas .....	25
Figure 18. Temperature of coolant outlet from the engine .....	26
Figure 19. Mass flow rate of coolant outlet from the engine .....	26
Figure 20. Exergy of coolant outlet from the engine.....	27
Figure 21. Available energy of coolant outlet from the engine .....	27
Figure 22. Optimal operating line of the target engine.....	29
Figure 23. A configuration of the target system .....	30
Figure 24. 1-D engine model implemented in AMESim.....	36
Figure 25. A schematic of gas injection system, Mixer.....	37
Figure 26. A schematic of coherent flame model [52] .....	38
Figure 27. Ignition and propagation of flame front in the model [52] .....	38
Figure 28. Thermal management model for 6-cylinder CNG engine.....	44
Figure 29. A schematic of ETM model .....	45
Figure 30. A schematic of the cooling circuit.....	47
Figure 31. The distribution of temperature of each part at 2300 rpm – 100 % ..	48
Figure 32. Implemented 0-D engine model in Matlab/Simulink.....	49
Figure 33. PM type generator efficiency .....	51

Figure 34. ID type traction motor efficiency.....	52
Figure 35. A schematic of the Li-Ion electrochemical model.....	57
Figure 36. A boundary condition of electrochemical battery model .....	58
Figure 37. Validation of the averaged electrochemical Li ion battery model.....	62
Figure 38. Schematic of quasi-1D heat exchanger model.....	63
Figure 39. Heat exchanger model implemented in Matlab/Simulink.....	66
Figure 40. Velocity diagram of the radial type turbine.....	69
Figure 41. The turbine model implemented in Matlab/Simulink .....	70
Figure 42. Hyperbolic tangent function for braking force gain.....	73
Figure 43. Forces acting on a vehicle during braking process [64].....	74
Figure 44. Braking force distribution strategy for the target vehicle .....	76
Figure 45. Validation result of vehicle speed in KATECH G mode.....	78
Figure 46. Validation results of the engine speed and torque in KATECH G mode.....	78
Figure 47. Validation results of the generator electric power and speed in KATECH G mode .....	79
Figure 48. Validation results of the motor speed and electric power in KATECH G mode .....	79
Figure 49. Validation result of SOC trajectory in KATECH G mode .....	80

Figure 50. Validation results of fuel consumption in KATECH G mode.....	81
Figure 51. T-S diagram of R245fa.....	88
Figure 52 . T-S diagram of R1234yf.....	88
Figure 53. T-S diagram of toluene.....	89
Figure 54. T-S diagram of water.....	89
Figure 55. T-S diagram of ethanol.....	90
Figure 56. A T-S diagram of superheated Rankine cycle .....	90
Figure 57. Rankine cycle efficiency according to the working fluids and the pressure ratio .....	91
Figure 58. Rankine efficiency of water according to the temperature at the turbine inlet .....	94
Figure 59. Rankine efficiency of R245fa according to the temperature at the turbine inlet .....	94
Figure 60. Specific speed vs. Efficiency (Rohlick, 1975).....	96
Figure 61. An efficiency of the turbine according to the inlet angle and a specific speed (R245fa, outlet temperature 318.1 K) .....	99
Figure 62. An inlet temperature of the turbine according to the inlet angle and a specific speed (R245fa, outlet temperature 318.1 K).....	99
Figure 63. A maximum pressure ratio of the turbine according to the inlet angle and a specific speed (R245fa, outlet temperature 318.1 K).....	100

Figure 64. A work of the turbine according to the inlet angle and a specific speed (R245fa, outlet temperature 318.1 K).....	100
Figure 65. A speed of the turbine according to the inlet angle and a specific speed (R245fa, outlet temperature 318.1 K) .....	101
Figure 66. A diameter of the turbine according to the inlet angle and a specific speed (R245fa, outlet temperature 318.1 K) .....	101
Figure 67. An inlet temperature of the turbine according to the inlet angle and a specific speed (R245fa, outlet temperature 352.4 K) .....	102
Figure 68. A maximum pressure ratio of the turbine according to the inlet angle and a specific speed (R245fa, outlet temperature 352.4 K).....	103
Figure 69. A work of the turbine according to the inlet angle and a specific speed (R245fa, outlet temperature 352.4 K).....	103
Figure 70. An inlet temperature of the turbine according to the inlet angle and a specific speed (water, outlet dryness 85 %) .....	105
Figure 71. A maximum pressure ratio of the turbine according to the inlet angle and a specific speed (water, outlet dryness 85 %).....	106
Figure 72. A work of the turbine according to the inlet angle and a specific speed (water, outlet dryness 85 %).....	106
Figure 73. A speed of the turbine according to the inlet angle and a specific speed (water, outlet dryness 85 %).....	107
Figure 74. A diameter of the turbine according to the inlet angle and a specific speed (water, outlet dryness 85 %).....	107

Figure 75. An inlet temperature of the turbine according to the inlet angle and a specific speed (water, outlet dryness 100 %)	108
Figure 76. A maximum pressure ratio of the turbine according to the inlet angle and a specific speed (water, outlet dryness 100 %)	108
Figure 77. A work of the turbine according to the inlet angle and a specific speed (water, outlet dryness 100 %)	109
Figure 78. $StPr^{2/3}$ and friction factor of 5.3 type Heat exchanger	119
Figure 79. $StPr^{2/3}$ and friction factor of 14.77 type Heat exchanger	119
Figure 80. $StPr^{2/3}$ and friction factor of 10.27T type Heat exchanger	120
Figure 81. $StPr^{2/3}$ and friction factor of 30.33T type Heat exchanger	120
Figure 82. Comparison of BSFC between with and without BSFC	126
Figure 83. Finding out optimal trajectory based on Bellman`s optimality [67]	128
Figure 84. Determination of $SC_{eng}$ factor from slope value	131
Figure 85. A flow chart of the thermostatic control strategy	133
Figure 86. A schematic of semi-iterative simulation method	134
Figure 87. Transient simulation result of engine metal parts with 1-D engine model and ETM model under 1200 rpm – 100 % condition at cold start	136
Figure 88. Transient simulation result of exhaust gas with 1-D engine model and ETM model under 1200 rpm – 100 % condition at cold start	136

Figure 89. A speed profile of KATECH 150 .....	137
Figure 90. A speed profile of KATECH G .....	138
Figure 91. A speed profile of Braunschweig cycle.....	138
Figure 92. A speed profile of heavy-duty UDDS .....	139
Figure 93. A speed profile of JE05 .....	139
Figure 94. A SOC trajectory in KATCH 150.....	141
Figure 95. Engine operation power in KATCH 150 (1300~1750 sec).....	141
Figure 96. WHRS operation power in KATCH 150 (1300~1750 sec).....	142
Figure 97. A SOC trajectory in KATCH G.....	142
Figure 98. Engine operation power in KATCH G (1075~1500 sec).....	143
Figure 99. WHRS operation power in KATCHE G (1075~1500 sec) .....	143
Figure 100. A SOC trajectory in Braunschweig .....	144
Figure 101. Engine operation power in Braunschweig (1200 ~ 1510 sec) .....	144
Figure 102. WHRS operation power in Braunschweig (1200 ~ 1510 sec) .....	145
Figure 103. A SOC trajectory in Heavy-duty UDDS .....	145
Figure 104. Engine operation power in Heavy-duty UDDS (600 ~ 930 sec)...	146
Figure 105. WHRS operation power in Heavy-duty UDDS (600 ~ 930 sec) ..	146

Figure 106. A SOC trajectory in JE05 .....	147
Figure 107. Engine operation power in JE05 (1280 ~ 1650 sec) .....	147
Figure 108. WHRS operation power in JE05 (1280 ~ 1650 sec) .....	148
Figure 109. A relation between the engine generation energy and improvement .....	149
Figure 110. Determining a $SC_{eng}$ value without WHRS (a) and with WHRS (b) in KATECH 150 .....	151
Figure 111. Determining a $SC_{eng}$ value without WHRS (a) and with WHRS (b) in KATECH G .....	151
Figure 112. Determining a $SC_{eng}$ value without WHRS (a) and with WHRS (b) in Braunschweig .....	152
Figure 113. Determining a $SC_{eng}$ value without WHRS (a) and with WHRS (b) in Heavy-duty UDDS .....	152
Figure 114. Determining a $SC_{eng}$ value without WHRS (a) and with WHRS (b) in JE05 .....	153
Figure 115. ECMS map without WHRS in KATECH 150 .....	154
Figure 116. ECMS map with WHRS in KATECH 150.....	154
Figure 117. ECMS map without WHRS in KATECH G.....	155
Figure 118. ECMS map with WHRS in KATECH G.....	155
Figure 119. ECMS map without WHRS in Braunschweig .....	156

Figure 120. ECMS map with WHRS in Braunschweig .....	156
Figure 121. ECMS map without WHRS in Heavy-duty UDDS .....	157
Figure 122. ECMS map with WHRS in Heavy-duty UDDS .....	157
Figure 123. ECMS map without WHRS in JE05 .....	158
Figure 124. ECMS map with WHRS in JE05 .....	158

## Acronym

WHRS	Waste Heat Recovery System
SHEV	Series type Hybrid Electric Vehicle
PM	Particulate Matter
NO <sub>x</sub>	Nitrogen oxides
TEG	Thermo-Electric Generation
OOL	Optimal Operating Line
CNG	Compressed Natural Gas
LiB	Lithium Ion Battery
SI	Spark Ignition
PM type	Permanent Magnetic type
ID type	Induction type
ETM	Engine Thermal Management
Temp.	Temperature
Exh.	Exhaust gas
ECMS	Equivalent Consumption Minimization Strategy
FTP	Federal Test Procedure
Max.	Maximum
Ave.	Average
SOC	State of Charge

# Chapter 1. Introduction

## 1.1 Motivation

Recently, the oil price hike and the stringent emission regulations are great issues in the automotive industry. As shown in Figure 1, it is required to satisfy the target value legislated by governments. Especially, in USA, the average fuel economy of vehicles has to be improved by 66 % compared to the average fuel economy of 2010 until 2025. Thus, it is necessary to investigate and develop various technologies such as hybrid electric vehicle to achieve the goal.

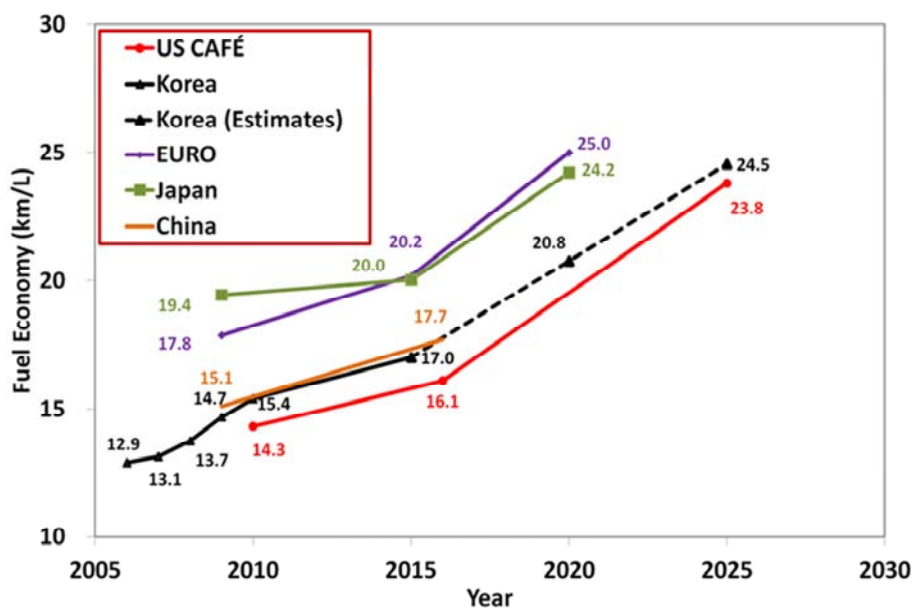


Figure 1. Regulation of fuel economy

In addition, the emission regulations which are shown in Figure 2 should be satisfied with achievement of improvement in fuel economy. EURO 6 emission regulation will be applied to PM emission as well as NO<sub>x</sub> emission in 2014. Thus, there were efforts to develop high efficiency and low emission vehicles. For instance, Direct Injection system for gasoline and diesel fuel, variable valve timing and lift system, exhaust after-treatment system, and hybrid electric vehicle have been developed and applied. These technologies have achieved outstanding improvements in fuel economy and emissions. However, especially in a perspective of fuel economy, previous methods to improve fuel economy have limitation.

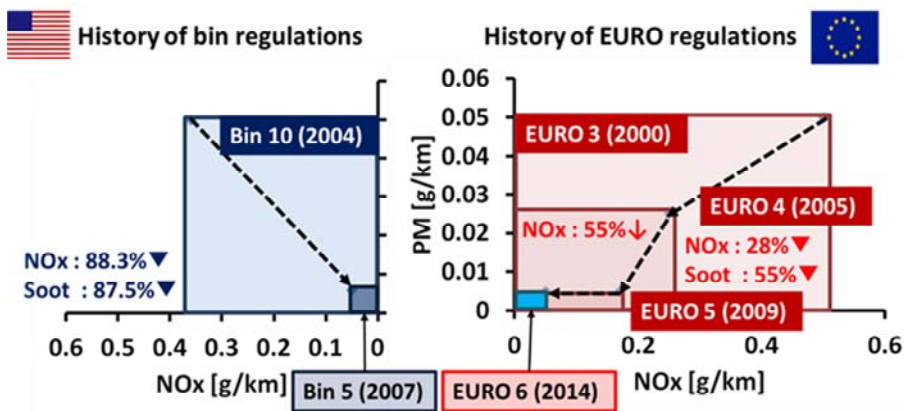


Figure 2. Regulation of emission

In conventional powertrain systems such as an internal combustion engine and a hybrid powertrain, maximum fuel conversion efficiency is limited by 40 % as shown in Figure 3 [1]. In other words, 60 % of fuel energy is rejected into coolant and exhaust gas. Thus, it is impossible to improve fuel conversion efficiency more than limitation without utilizing rejected energy. The energy of exhaust gas is high level enough to be used as heat source for other thermal

dynamic cycle, such as Rankine cycle. Moreover, the energy of charged air in intercooler which should be cooled down and the energy of coolant are sufficient as heat sources for the organic Rankine cycle. Rankine cycle is a kind of Waste Heat Recovery System (WHRS) technologies which recover wasted energy and use it to drive vehicles or to generate electric energy.

A series hybrid electric vehicle (SHEV) received attention as next generation vehicle system. In SHEV, only the traction motors are used to drive the vehicle while the engine is used to generate electric energy. It means that the engine can be operated regardless of vehicle driving state. Thus, the engine can be operated as a steady state at optimal operating point where the efficiency is the highest. Because the WHRS is operated with wasted heat from the engine, the steady state operation of the engine means the steady state supplement of heat source to the WHRS. Thus, SHEV offers very favorable environment to the WHRS compared to other powertrain configurations such as parallel HEV and conventional powertrain.

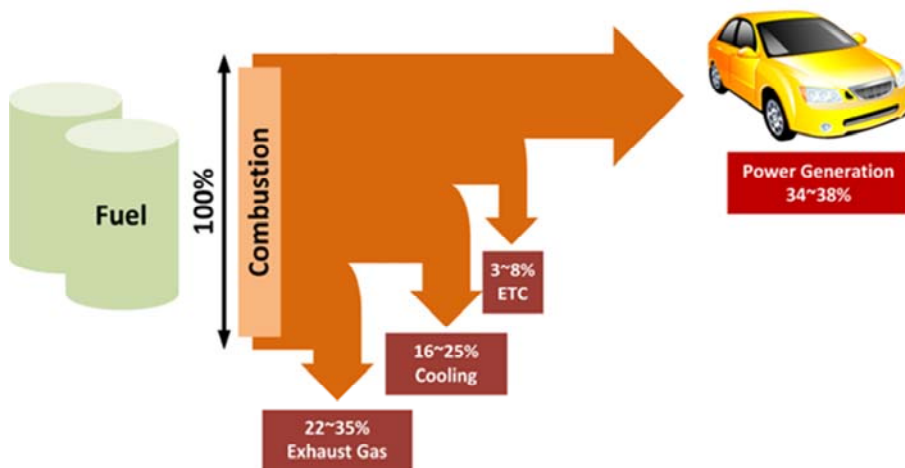


Figure 3. Energy flow in vehicles

## 1.2 Literature Review

In generally, there are three representative technologies to recover waste energy from the vehicle. Three technologies use exhaust gas as main heat source because it has the highest level energy compared to other waste heat sources such as charged air and coolant. In this research, it is assumed that recovered energy is applied only to drive vehicle or to generate electric energy. Thus, other technologies which use recovered energy to warm the coolant or transmission oil up at cold start condition are not considered.

### 1.2.1 Thermo-electric generation (TEG)

The thermo-electric generation (TEG) uses Seebeck effect to generate electric energy from heat energy, directly [2]. Typical TEG module is shown in Figure 4.

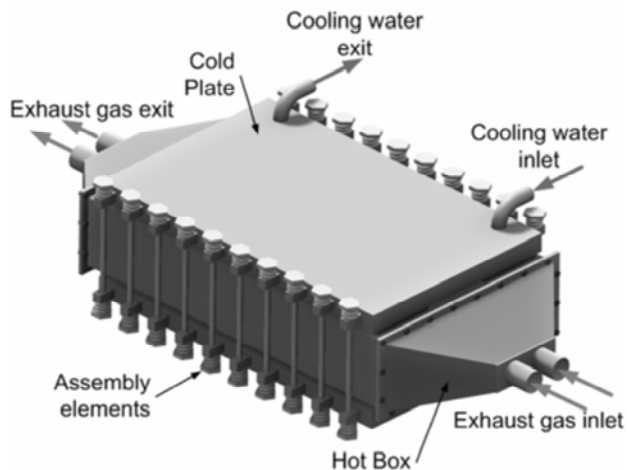


Figure 4. Typical TEG module [3]

Ikoma et al. obtained 35.6 W electric energy with 3000 cc gasoline engine [4]. In the study, Si-Ge module has been suggested and the experiment has been conducted with 72 modules. The length and the width of the system are 440 mm and 180 mm, respectively. Bass et al. studied to develop 1 kW thermoelectric generation system which was equipped in class eight diesel engine truck [5]. In the study, 72 Hi-Z's 13 Watt bismuth-telluride thermoelectric modules were applied. The length is 482.6 mm and the diameter is 228.6 mm. The experiment was conducted with 14 L Commins NTC 325 engine. To improve efficiency of the system, the geometry of the heat exchanger was optimized. However, it showed about 4.5 % conversion efficiency. Thacher et al. studied about 300 W TEG system [6]. The conversion efficiency of the system was 2.9 %.

The researches of TEG focused on the overall system experiment and thermoelectric device. Especially, development of new device which shows higher fuel conversion efficiency is main stream in TEG researches. In addition, optimization of the heat exchanger is another issue to improve efficiency of the TEG system. However, TEG system requires higher cost compared to other WHRS whereas the conversion efficiency is low. In addition, TEG system requires large temperature difference to achieve high efficiency, which can be implemented with additional cooling system.

### **1.2.2 Turbo-compound**

The turbo-compound technology uses the kinetic energy of the exhaust gas to generate electric energy. The architecture of the turbo-compound is shown in Figure 5. Turbo-compound system has similar architecture compared to the turbocharger. An electric machine is installed between the turbine and the compressor to generate electric energy or to supply additional energy to compress intake air as like supercharger.

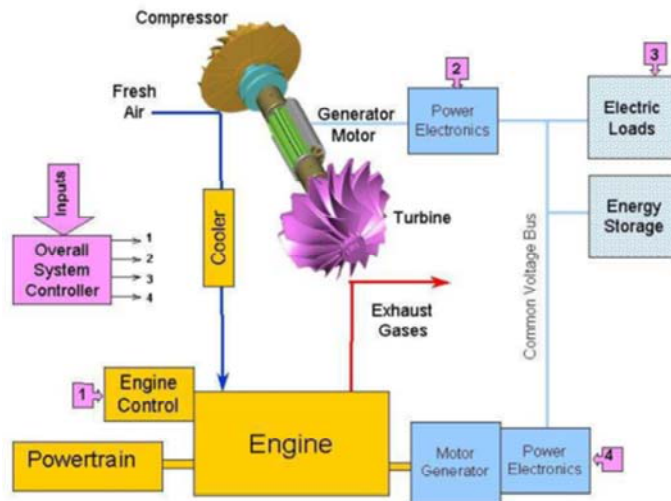


Figure 5. Turbo-compound system diagram [7]

Algrain [7] has studied on the control of turbo-compound system with diesel engine. Class-8 on-highway truck engine was selected as the target engine, and the simulation was conducted on steady state. In the study, at maximum load condition, 10 % reduction of fuel consumption has been achieved. When the engine load fluctuated between 25 % and 50 % (main operation range), the fuel economy was reduced about 5 %.

Eriksson et al. [8] have suggested various configurations of turbo-compound system. Turbo-compound system was operated in different modes : normal turbocharger mode, e-boosting mode, and exhaust heat recovery mode which uses electric machine and provides additional torque to the crank shaft according to the engine operation state.

Ismail et al. [9] have simulated turbo-compound system using AMESim software. The engine was implemented based on 1D engine model. In order to investigate precise effect of turbo-compound on engine performance, the exhaust

line was validated with the experimental data. The back pressure effect was also reflected by applying the throttle model. Various effect caused by turbo-compound was estimated and the optimization of the combustion was conducted by adjusting injection timing, EGR valve open rate, etc. In the study, the main focus was to stabilize the engine combustion with turbo-compounding system.

Turbo-compound is cost-effective compared to other systems because it can use turbocharger architecture. It means that additional part is only electric machine which is installed between the turbine and the compressor. Moreover, it shows remarkable improvement in fuel economy. However, it can cause instability of the combustion in the engine. In addition, the total amount energy which can be recovered from heat sources is smaller than other technologies because it just uses the kinetic energy of the exhaust gas.

### **1.2.3 Rankine cycle**

Rankine cycle has been used in electric power generation plant and ship propulsion system to generate electric energy as a main cycle or bottoming cycle for upper cycle such as Brayton cycle. Especially in power plant fields, Rankine cycle is combined with Brayton cycle to improve fuel conversion efficiency. In automotive industry, a possibility of combined cycle which consists of Diesel cycle and Rankine cycle has been investigated and suggested [10].

These days, requirement of waste heat recovery in vehicle to improve fuel economy, many studies which focus on Rankine cycle have been conducted. Although the Rankine cycle requires additional components such as a pump, a heat exchanger, an expander, and a condenser, it showed the highest potential to improve fuel economy [3, 7].

The previous researches of Rankine cycle can be classified into selecting a working fluid, analyzing thermodynamic performance, and designing optimal components. In part of designing optimal components, a heat exchanger, an expander, a pump, and a condenser were taken into account. Among components, a heat exchanger and an expander have main effect on performance of Rankine cycle. Thus, various heat exchangers and expanders have been studied in previous studies.

Endo et al. [11] and Kadota et al. [12] studied on Rankine cycle which uses swash plate type expander. Heat exchanger, expander, condenser, and pump were designed and implemented. That system was installed in parallel HEV to generate electric energy. At 100 km/h constant speed condition, the thermal efficiency was improved by 13.2 %.

Ringler et al. [13] analyzed performance of the various Rankine cycle configurations and working fluids. Ethanol, water, and toluene were adopted as working fluids and various combinations of heat sources were investigated. Consequently, water and ethanol were selected for single heat source and double heat sources system. In double heat sources system, coolant and exhaust gas were selected as heat sources. By using the system, they improved engine performance about 10 % at steady state condition.

Chammas et al. [14] investigated on working condition of Rankine cycle according to working fluids such as water, R245fa, and isopentane. Cycle efficiency of each working fluid was evaluated according to turbine inlet temperature and pressure. High pressure steam cycle, low pressure steam cycle, and organic Rankine cycle were compared. As the results, it was suggested that high pressure steam cycle could improve fuel economy by 13 %.

Teng et al. [1, 15] have investigated on organic Rankine cycle for application to heavy duty vehicle. They constructed various Rankine loop by adopting exhaust gas, charged air, and EGR as heat sources. A supercritical reciprocating Rankine engine was used as an expander. Thermodynamic analysis was conducted with various working fluids. Especially, they investigated about mixture which consists of different organic fluid. As the results, their system improved fuel economy about 15 ~ 20 %.

Yamada et al. [16] researched into open steam Rankine cycle with hydrogen internal combustion engine. A characteristic of hydrogen engine was considered to be combined with Rankine steam cycle. They analyzed Rankine cycle output according to engine operation condition. By combining Rankine cycle with hydrogen internal combustion engine, overall thermal efficiency was improved by 2.9 ~ 3.7 %.

In addition, previous studies on the various system configurations, the working fluid types, and the expander types have been conducted [17-29] . In these studies, 6 types of expander were considered : swash plate, scroll, reciprocating Rankine engine, Rotary vane, turbine and gerotor. Swash plate, scroll, rotary vane and gerotor were used as hydraulic compressor, generally. Thus, the methods to design and to implement those expanders were well-known. Reciprocating Rankine engine was also used to assist crank torque because it can be operated in similar speed range compared to the internal combustion engine. Turbine was also used as expander to generate additional electric energy in Rankine cycle. Schematics of Swash plate type, scroll type, rotary vane type and gerotor type expanders are shown in Figures 6 ~ 9.

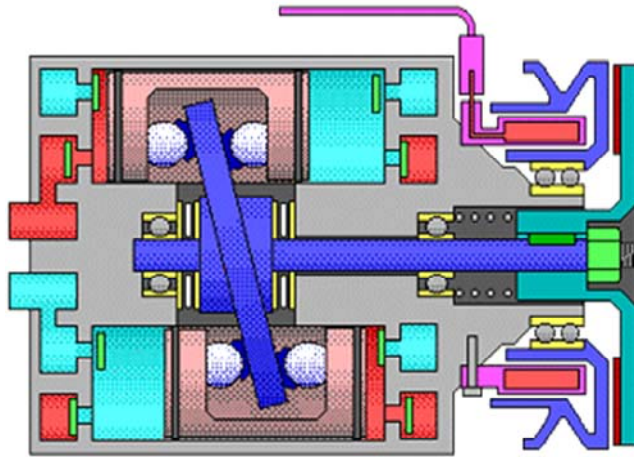


Figure 6. A schematic of the swash plate type expander [30]

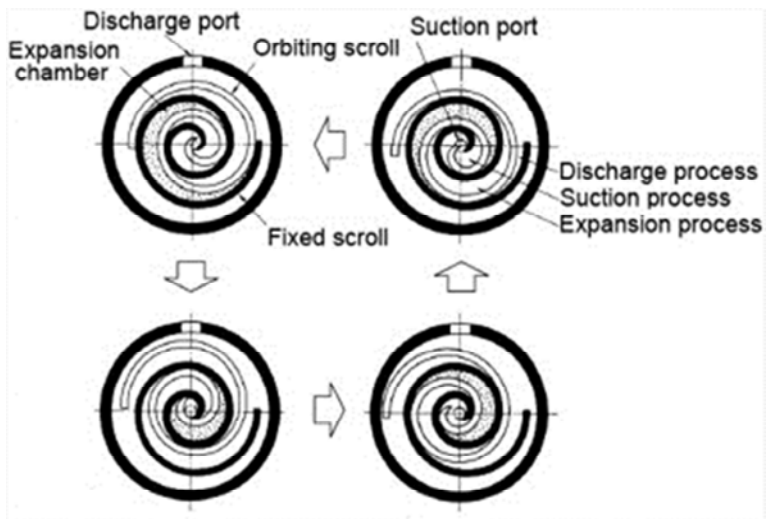


Figure 7. A schematic of the scroll type expander [31]

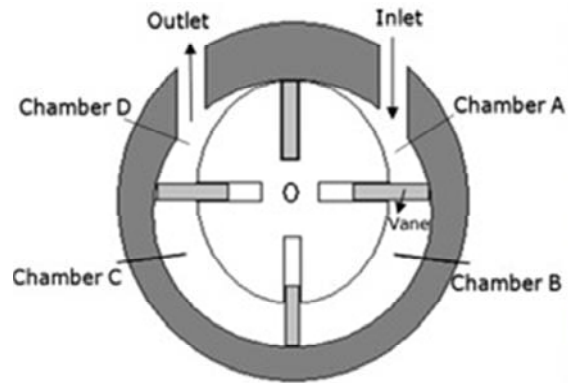


Figure 8. A schematic of the rotary vane type expander [32]



Figure 9. A schematic of the gerotor type expander [33]

Diego et al. [34] have developed Rankine cycle model and applied to vehicle simulation. Recovered energy by Rankine cycle during FTP-72 cycle was estimated. This paper suggested optimizing a working fluid type, designs of heat exchanger and turbine, and an engine cooling system as future work.

Marvridou et al. [35] studied on the various heat exchanger. They developed model to evaluate performance of heat exchanger. In heat exchanger model, simulating a boiling process is very important calculation process because that process includes two-phase state. In the study, boiling which affects heat transfer coefficient was adopted in the model. In addition, pressure drops in various heat exchangers were compared. The most effective heat exchanger type that was recommended in this paper was plate fin type and metal form type because they showed lower pressure drop and higher heat transfer coefficient than other types.

Lopes et al. have compared results of previous researches [36]. In this paper, researches concerned with automotive application of Rankine cycle were arranged. Table 1 shows the results of previous researches.

From previous researches, it is obvious that they did not consider practical application and control of the overall system. In other words, optimization which considers real environment application has not been conducted. However, to implement system in real application, it is important to consider the limitation of the system. In addition, in order to achieve high fuel economy with a specific target system, the optimal control strategy is required.

Table 1. Results of previous studied concerned with various Rankine cycle applications [36]

Type	$P_{in,exp}$ [bar]	PR	$T_{in,exp}$ [C]	$W_{exp}$ [kW]	N [rpm]	fluid	$\eta_{cycle}$	year	ref.
Turbine	7.3	4.1	85	32.7	20,000	R245fa	6.1	2011	[37]
	2.2	1.1	70	-	60,000	HFE-301	7.6	2006	[38]
	2.7	1.1	95	-	60,000	n-Pentane	5	2006	[38]
	3.4	2	70	0.15	35,000	R123	-	2001	[39]
	25	25	220	6.03	4,000	Water	13.3	2005	[14]
	22.5	8	143	6.66	4,000	R245fa	8.7	2005	[14]
	19	8	151	6.63	4,000	i-Pentane	9	2005	[14]
Swash plate	80	-	500	2.98	1,500	Water	13	2007	[11]
Rotary vane	-	-	90	0.03	2,095	R245fa	3.8	2010	[40]
	6.3	-	170	0.82	-	R123	-	2011	[41]
	7	-	170	1.93	6,500	R123	-	2011	[41]
Gerotor	4.1	3	84	0.67	3,670	R123	-	2009	[42]
	18.8	8.3	146	2.67	3,670	R123	-	2009	[42]
	7.2	3	130	1.38	3,670	R123	-	2009	[42]
	12.3	4.2	150	5.3	3,670	R123	-	2009	[42]
	11.2	3.4	157	2.63	3,670	R123	-	2009	[42]
	10.9	5.3	160	2.96	3,670	R123	-	2009	[42]
Scroll	10	5	142	-	2,296	R123	-	2009	[43]
	9.4	8.6	136	0.35	2,800	R113	7	2009	[31]
	5.5	3.9	174	0.19	1,053	R123	6.8	2008	[44]
	6.1	3.9	173	0.22	1,223	R123	6.6	2008	[44]
	6.4	3.8	169	0.26	1,287	R123	7.2	2008	[44]
	-	4	-	1	3,600	R245fa	-	2010	[45]
	13.5	8.8	127	1.46	3,670	R123	-	2009	[42]

18.2	5.5	149	2.12	3,670	R123	-	2009	[42]
11.9	3	120	1.53	3,670	R123	-	2009	[42]
17.9	3.1	155	2.4	3,670	R123	-	2009	[42]
12.7	5.6	128	2.58	3,670	R123	-	2009	[42]
15	6.1	137	2.65	3,670	R123	-	2009	[42]
20.4	8.2	154	3.95	3,670	R123	-	2009	[42]
3.3	-	70	0.21	891	R134a	4.7	2009	[46]
13	-	65	2.05	2,000	R134a	7.5	2009	[46]
13	11.4	145	11	1,400	Water	-	2007	[47]
32.8	2	120	1.7	4,500	R1234yf	6.4	2011	[48]
25	10	160	2.88	-	R234fa	5.8	2011	[49]
12	7.2	75	1.75	2,500	R234fa	8.6	2011	[50]

### 1.3 Objective

Many researches have been conducted to study waste heat recovery system, especially Rankine cycle. However, practical implementation and control method for overall system has not been considered. Thus, this study aims to overcome those limitations and to suggest a method to develop optimal WHRS and how to control the system.

The objective of this research is described as below:

1. By using simulation, a method to optimize components of Rankine cycle was suggested with consideration of practical implementation. In order to optimize Rankine cycle, optimal working fluid, working condition was defined. In addition, heat exchanger and turbine which are core components of Rankine cycle was optimized to achieve high efficiency.

2. In previous researches, pressure ratio of working fluid was determined without consideration of expander operation. However, pressure ratio is limited by expander design. In this study, turbine was adopted as expander and pressure ratio was limited by sound of speed of working fluid in turbine. Thus, if it is not considered, real implementation can be impossible and the system efficiency can be misestimated. Thus, design of turbine was conducted to ensure real implementation and precise estimation. Moreover, in order to achieve high pressure ratio with turbine, multi-stage design was applied to the system.
3. The WHRS used exhaust gas as main heat source in previous studies. However, there is no consideration of exhaust gas behavior at cold start. It is obvious that the temperature of exhaust gas at cold start has lower value compared to fully warmed-up state. Thus, WHRS operation at cold start state should be different because normal operation is set to fully warmed-up state. Therefore, it is necessary to estimate the behavior of exhaust gas temperature at cold start state. Thus, 1-D engine model and engine thermal management model was applied to simulate transient behavior of exhaust gas. As the results, WHRS working condition at cold start was able to be defined.
4. There were many researches to investigate improvement in fuel economy of conventional vehicle and parallel hybrid vehicle with WHRS. However, there was no research about application of WHRS to series HEV. In this study, the method to apply WHRS optimally to series HEV was suggested in respect of control strategy and system design.

5. Once the system configuration is determined, the system performance is affected by control strategy, mainly. It is important to determine proper and optimal control strategy for the overall system. However, there was no study about control strategy for WHRS with overall vehicle system. Therefore, global optimal control strategy such as dynamic programming, local optimal control strategy such as equivalent consumption minimization strategy, and simple on/off control strategy were applied to the overall system in order to suggest optimal control strategy.

## **Chapter 2. Thermodynamic analysis on the heat sources**

In this chapter, the analysis on the heat sources is described. Because there are many heat sources in the internal combustion engine of the series HEV, it is necessary to calculate recoverable energy level of each heat source. Thus, two thermodynamic values were calculated (exergy and available energy). By conducting a calculation of exergy and available energy, the operation point of the engine where the total exergy and available energy of heat sources has the highest level could be found out. Based on the results, selecting heat sources and determining operation point of engine for WHRS was conducted.

### **2.1 Exergy and available energy**

In thermodynamics, it is important to define the maximum useful work of system. By calculating maximum useful work, it is possible to predict recoverable energy level which can be extracted from wasted heat. The maximum useful work of the system is defined as the exergy. It is calculated by assuming the outlet state of the system is the same to atmospheric pressure and temperature. The available energy is reversible energy which is generated when the system interacts with the atmosphere.

In open system, the differences between inlet and outlet of enthalpy and entropy are determined as below equations [51].

$$\dot{m}(h_e - h_i) = (-\dot{Q}_{atm}) - \dot{W}_{ie} \quad (2.1)$$

$$\dot{m}(s_e - s_i) = -\frac{\dot{Q}_{atm}}{T} + \dot{\Theta} \quad (2.2)$$

where,  $\dot{\Theta}$  is the formation entropy which includes entropy generated by process in the system and by difference temperature between the system and atmosphere.  $h$ ,  $T$ ,  $s$ ,  $\dot{Q}_{atm}$  and  $\dot{m}$  are the enthalpy, temperature, entropy, heat transfer rate to the atmosphere and mass flow rate, respectively. Subscript *atm* means atmospheric state. Above equations can be reduced as below equations with assumption of ideal case,  $\dot{\Theta} = 0$ .

$$\dot{W}_{ie} = \dot{m}[(h_i - T_{atm}s_i) - (h_e - T_{atm}s_e)] - T_{atm}\dot{\Theta} \quad (2.3)$$

$$\dot{W}_{revie} = \dot{m}[(h_i - T_{atm}s_i) - (h_e - T_{atm}s_e)] \quad (2.4)$$

It is available energy of open system between state *i* and state *e*. The available energy can be maximized when the state *e* is the same to atmospheric state, and that maximized available energy is the exergy. In the open system, the specific exergy can be defined as below equation.

$$\phi = (h - T_{atm}s) - (h_{atm} - T_{atm}s_{atm}) = C_p(T - T_{atm}) - T_{atm}(s - s_{atm}) \quad (2.5)$$

where,  $C_p$  is the constant pressure specific heat capacity. By defining the exergy, the available energy can be determined as difference between exergy of inlet and outlet as below equation.

$$\dot{W}_{ie} = \dot{m}(\phi_i - \phi_e) - T_{atm}\dot{\Theta} \quad (2.6)$$

The reversible available energy can be determined as below equation.

$$\dot{W}_{ie} = \dot{m}(\phi_i - \phi_e) \quad (2.7)$$

Between the exergy and available energy, the available energy is more proper to calculate the generated energy in the WHRS because the exergy assumes that the outlet state is an atmospheric state. In other words, it is impossible to implement exergy condition in real application. Thus, the engine operation points should be determined based on the available energy.

In this study, a charged air, an exhaust gas and a coolant were considered as heat sources for the WHRS. The temperature, mass flow rate, exergy and available energy of charged air are shown in Figures 10 ~ 13. The physical properties of exhaust gas, coolant and charged air were based on Cantera which was developed by Stanford University. In the case of coolant, properties of pure water were assumed. As shown in Figure 10, a temperature of the charged air at the high load and high speed region of the engine is higher than other operating points. In addition, the exergy and flow rate show similar distribution compared to the temperature. Although the temperature and exergy is relative high in middle speed and middle load region, the available energy is low in this region, because of the low flow rate. In other words, the flow rate affects the available energy significantly. It means that available energy level at high load and high speed region is greater than that other regions. Thus, the charged air can be used as heat source when the engine operates in high load and high speed region.

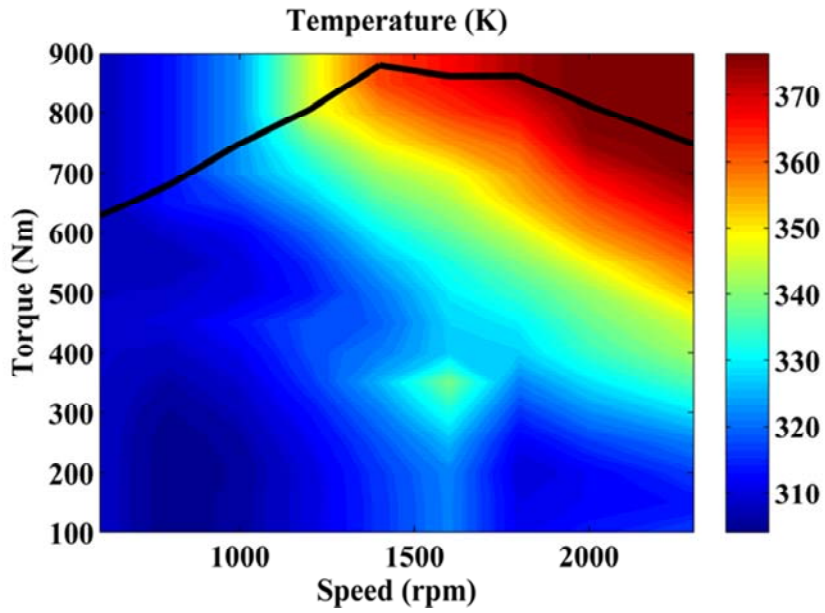


Figure 10. Temperature of the charged air

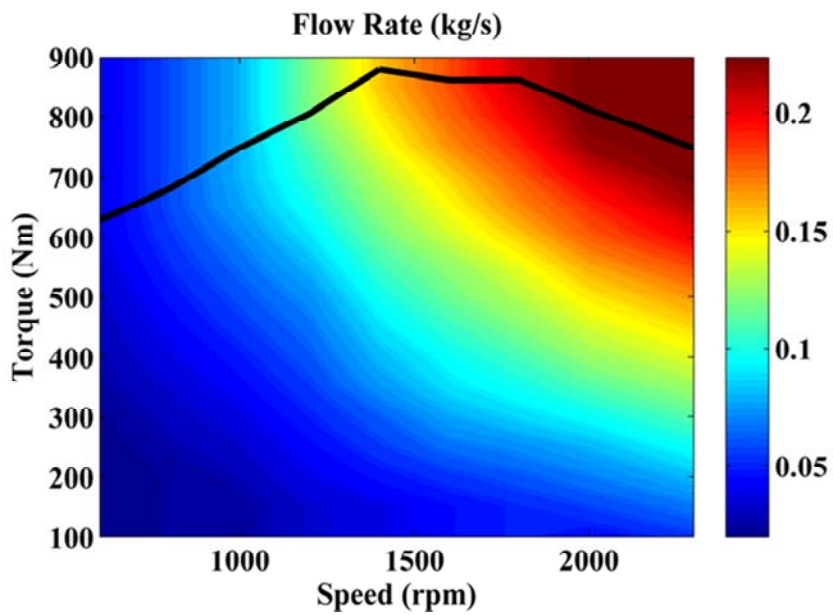


Figure 11. Mass flow rate of charged air

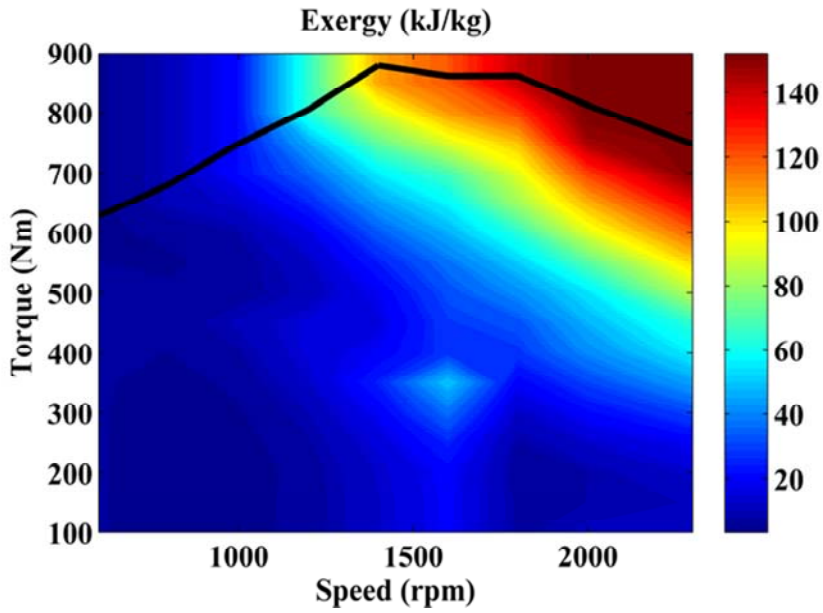


Figure 12. Exergy of charged air

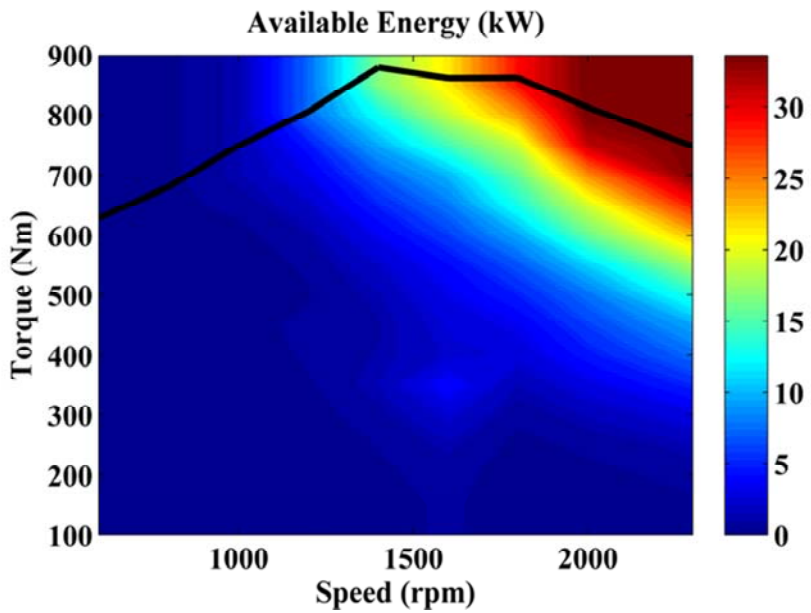


Figure 13. Available energy of charged air

The temperature, mass flow rate, exergy and available energy of the exhaust gas are shown in Figures 14 ~ 17. The temperature is high in high load and high speed region. It should be noted that the temperature of exhaust gas in low load and low speed region is higher than that in middle load and low speed region, and low load and high speed region. It can be estimated that is caused by activation of turbocharger. The temperature of exhaust gas was measured at the downstream of the turbine. It means that the temperature of exhaust gas is decreased when the turbocharger is activated because expansion work which causes decrease of temperature occurs in the turbine. Thus, a reason why the temperature of the exhaust gas is high in low load and low speed region is that the turbine is not working in that region. This deduction is reasonable because the intake air pressure shows the same value compared to the atmosphere pressure.

The exergy of exhaust gas shows similar distribution compared to that of the temperature. However, the available energy has high values in high load and high speed region because the flow rate has significant effect on the available energy as described above. Because the flow rate in high load and high speed region is much greater than in low load and low speed region, the available energy has high level in the region.

The temperature, mass flow rate, exergy and available energy of the coolant are shown in Figures 18 ~ 21. The temperature becomes high as engine operated in high load and high speed region. The distribution of exergy shows similar trend compared to that of temperature. However, it should be noted that the absolute difference of temperature is small. It means that the difference of temperature and the exergy on overall operation range is not great compared to other heat sources. Moreover, the mass flow rate is linear function of the engine speed because the coolant pump is connected with crank shaft mechanically.

Thus, the flow rate is increased as the engine speed is increased. Because the distributions of the exergy and the mass flow rate show similar trend, the distribution of available energy is similar to that of the exergy and the mass flow rate. However, it should be noted that the absolute values of the temperature and exergy on overall operation range are almost the same. Thus, the difference of the available energy value is caused by the mass flow rate which has various values according to the operation point.

The maximum values of available energy of charged air, exhaust gas and coolant are 33 kW, 74 kW and 29 kW, respectively. The available energy of the coolant is smaller than that of the charged air and exhaust gas because the inlet and the outlet temperature of them have small differences. In case of charged air, it is assumed that the 100 °C charged air is cooled down to 30 °C. In the same sense, it is assumed that the exhaust gas is cooled down from 550 °C to 30 °C. However, the coolant is just cooled down from 90 °C to 85 °C. Thus, the coolant has relative low available energy.

From the results, the engine operation point where is able to maximize the recovered energy can be estimated. That operation point is maximum power region (2300 rpm and 100 % load). In this operation point, 132 kW wasted energy can be recovered to drive vehicle or to generate electric energy. However, it is just theoretical value. The maximum energy that can be recovered by the WHRS is predicted by 40 kW with 30 % cycle efficiency of the WHRS. However, in respect of overall system, this operation cannot be optimal operating point, because this result focuses on maximum recovered energy. Selecting optimal operating point with consideration of overall system will be described in next chapter. However, it is meaningful result because the maximum energy which can be recovered by WHRS is estimated.

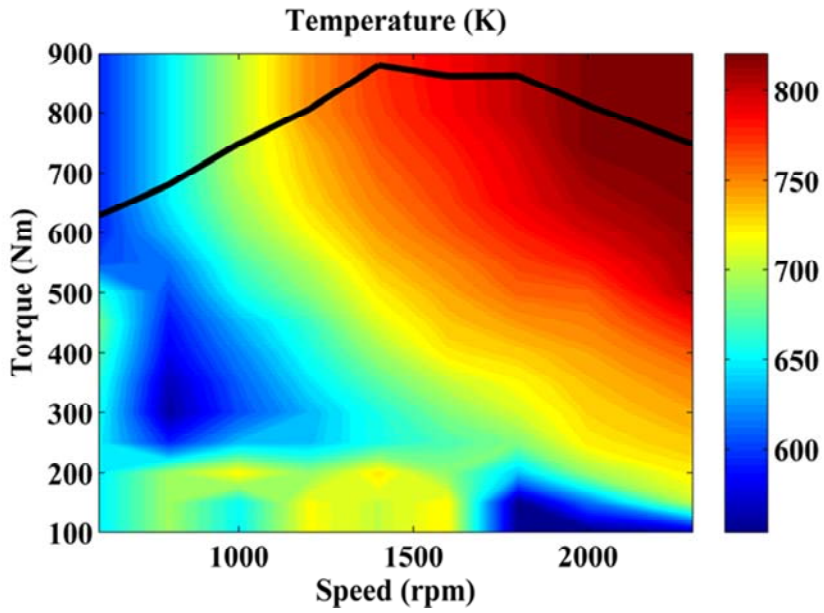


Figure 14. Temperature of exhaust gas

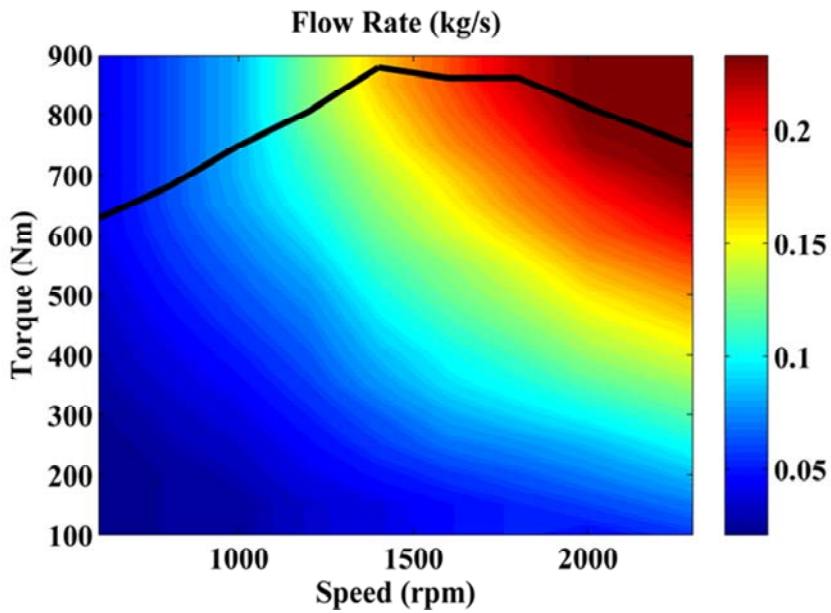


Figure 15. Mass flow rate of exhaust gas

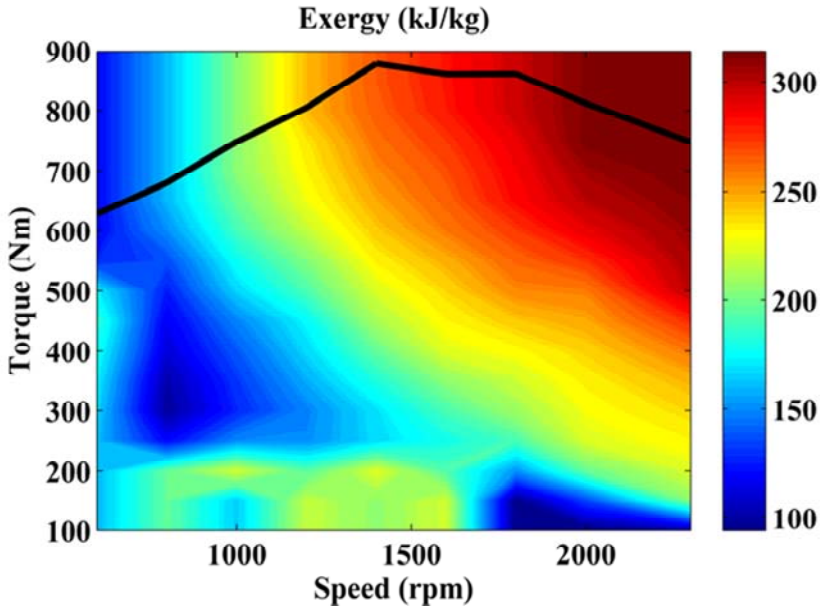


Figure 16. Exergy of exhaust gas

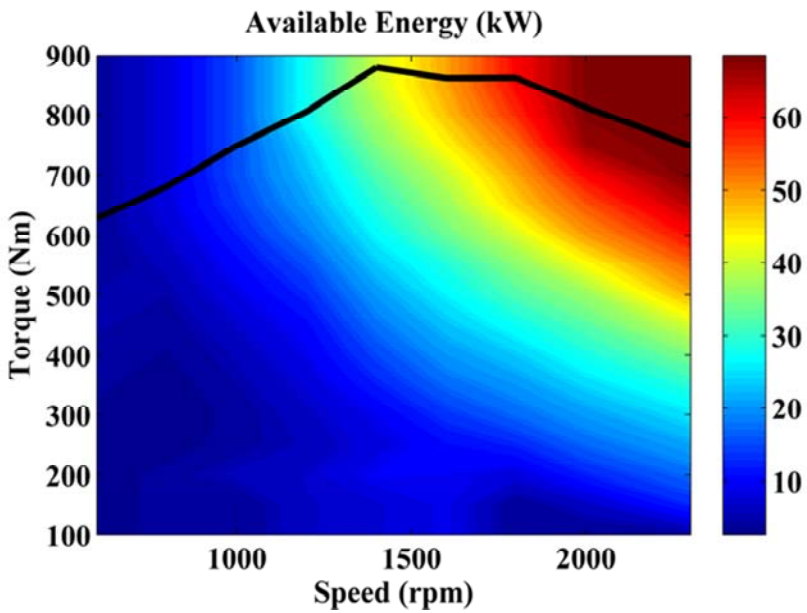


Figure 17. Available energy of exhaust gas

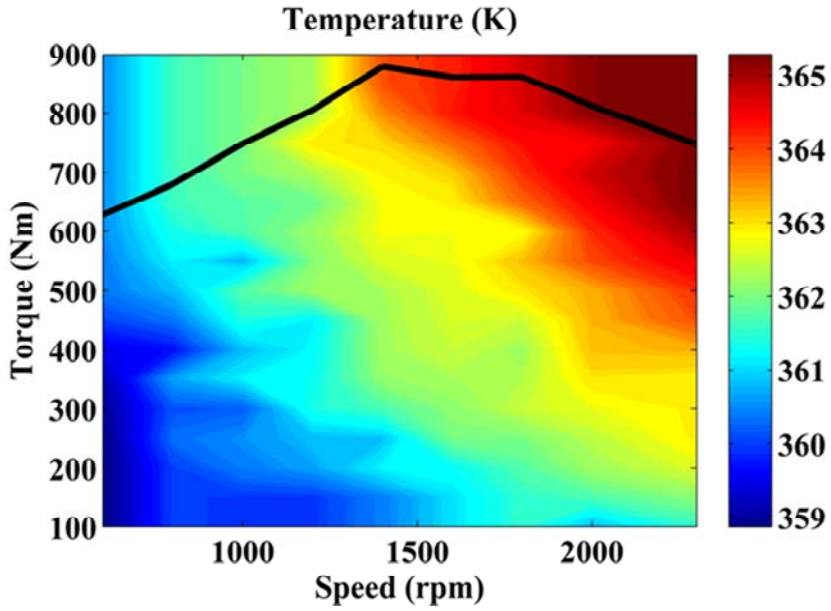


Figure 18. Temperature of coolant outlet from the engine

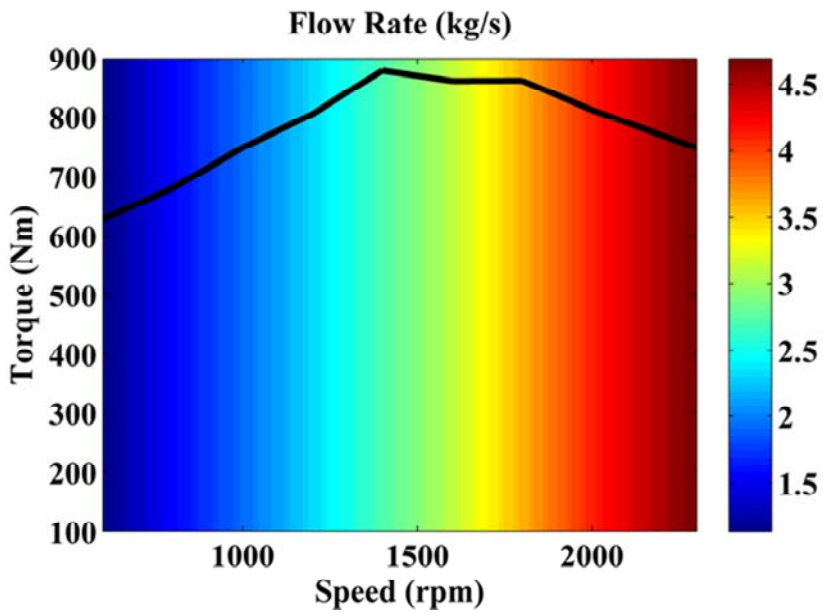


Figure 19. Mass flow rate of coolant outlet from the engine

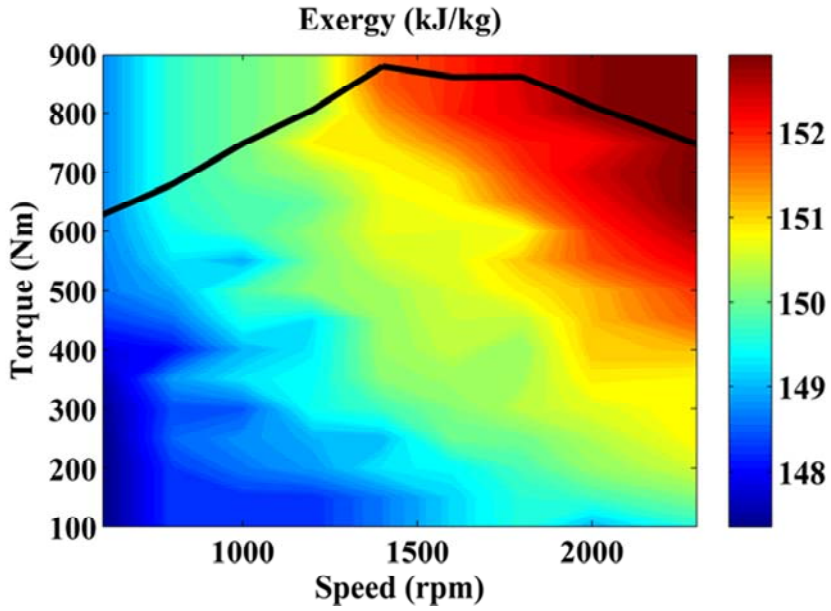


Figure 20. Exergy of coolant outlet from the engine

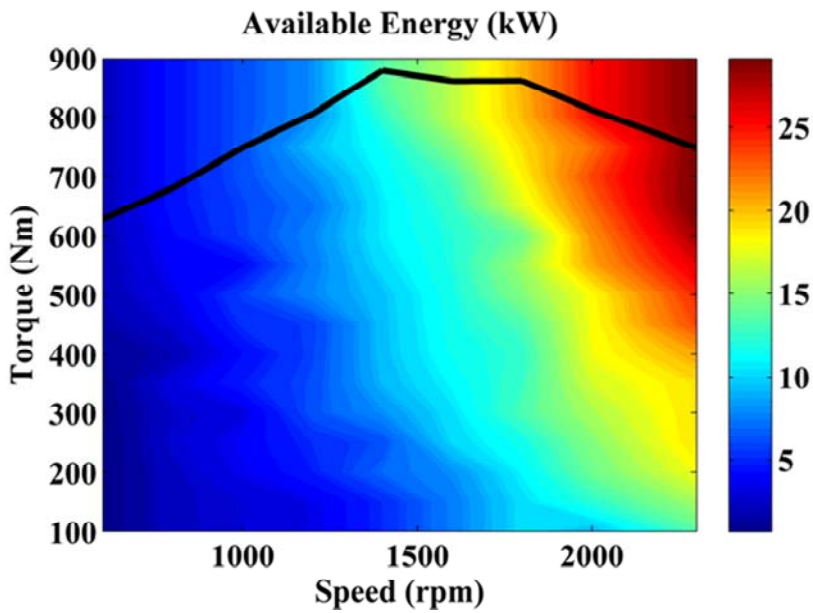


Figure 21. Available energy of coolant outlet from the engine

## 2.2 Engine and WHRS operation in SHEV

The configuration of the target vehicle is series HEV. It means that the engine operation is decoupled with driveshaft. Thus, the engine can be operated along with optimal operating line (OOL) which consists of the best bsfc points at specific output power values. The OOL of the target engine is shown in Figure 22. In the figure, a red line is maximum torque and black dot line is OOL. The OOL shows similar operating points compared to maximum torque. From the OOL and results of exergy and available energy, WHRS can use charged air, coolant, and exhaust gas simultaneously as heat sources when the engine operates over 1500 rpm. However, the temperatures of coolant and charged air are low to heat water up to superheated state. In this case, the charged air and the coolant can be used as pre-heater which heat the liquid state working fluid. If the working fluid of which boiling temperature is low is selected, the coolant and charged air can heat it up to superheated state. When the engine operates under 1500 rpm, the temperatures of coolant and charged air are low to heat the working fluid up to superheated state even the low boiling point working fluid is used. Thus, in this case, they are used as just pre-heater. Consequently, the working fluid properties and the engine operation points should be considered carefully to design Rankine cycle.

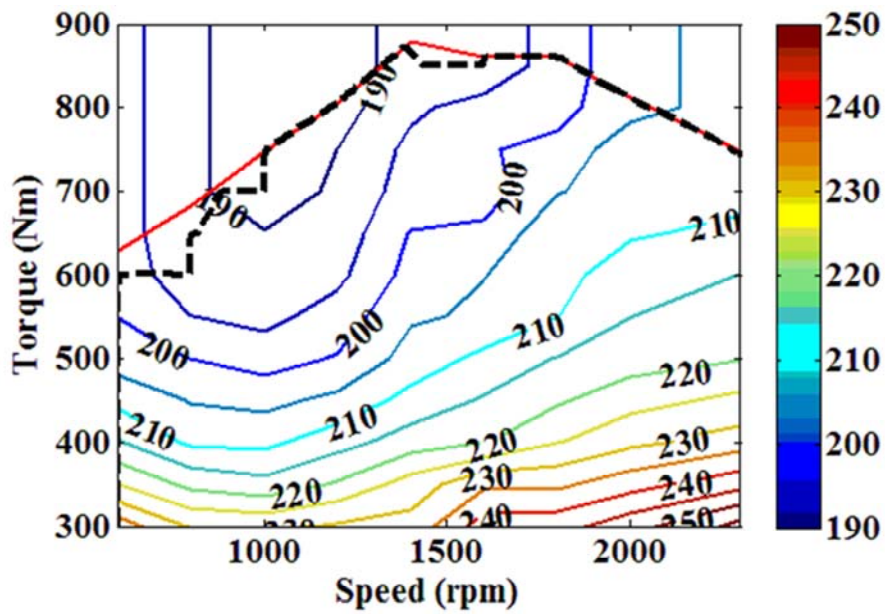


Figure 22. Optimal operating line of the target engine

## Chapter 3. Development and validation of models

### 3.1 System configuration

The configuration of the target system is similar to that of the conventional SHEV. A difference in the configuration is that the target system has WHRS to use rejected thermal energy such as exhaust gas, coolant, charged air and so on. The target system uses the generation system to supply electric energy with the battery according to the vehicle state. In target system, WHRS generates electric energy from rejected heat. The configurations of the target system are shown in Figure 23.

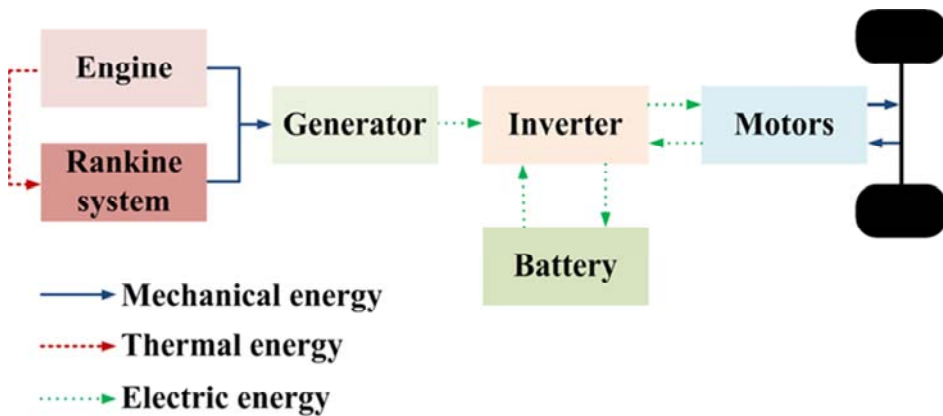


Figure 23. A configuration of the target system

The specifications of the target vehicle are listed in Table 2. The components of the conventional HEV system were applied to the target system because sizes and capacities of the engine, the motor, the generator and the battery have been optimized to achieve the best fuel economy by using an optimal control theory.

Table 2. The specifications of the target vehicle

Hybrid Type	Series
Engine	SI In-line 6 cylinders CNG 8070 cc (Lean-burn) (883 Nm / 1380 rpm) (176 kW / 2300 rpm)
Generator	PM type 180 kW
Motor	ID type 120 kW x 2
Battery	LiB 670 V (36 Ah)
Vehicle Mass (GVW)	15,500 kg
WHRS	Rankine Cycle (25 kW)

## **3.2 Powertrain model**

The powertrain model consists of the engine, the motor, the battery and the waste heat recovery model. Because the target vehicle is SHEV, the transmission model is not required. It is assumed that a final reduction gear has constant efficiency.

### **3.2.1 Engine model**

In general vehicle simulation, a simple 0-D engine model is adopted because the objective of the simulation is to calculate fuel consumption during a specific driving cycle. However, in this study, the rejected heat in the exhaust gas, the coolant and the charged air can be used as heat sources. Thus, a cold start condition should be considered because heat sources show different states at cold start condition compared to fully warmed-up state. For example, in cold start condition, exhaust gas and coolant temperatures are lower than those in warmed-up condition. However, charged air temperature shows similar at the same operation condition regardless of cold start and warmed-up conditions. Thus, the WHRS should be controlled with consideration of cold state. This is because that the 1-D simulation is needed in this research. By using 1-D engine simulation, it is possible to estimate the states of the exhaust gas, coolant and charged air even in cold start condition. Therefore, 1-D engine was developed based on the experimental results. However, it is hard to apply 1-D engine model to vehicle model because calculation time steps are greatly different compared to that of vehicle simulation. The calculation time step of 1-D engine model is  $10^{-5}$  second order, while that of vehicle model is  $10^{-3} \sim 10^0$  second order. Thus, in this study, 0-D engine model was developed and modified based on the result of the 1-D engine model to estimate the cold start condition.

### 3.2.1.1 1-D engine model

1-D engine model consists of intake system, combustion system, exhaust system and mechanical power system. It was developed based on a commercial simulation program AMESim<sup>®</sup> which is used in various applications [52]. Overall 1-D engine model is shown in Figure 24.

The target engine uses compressed natural gas (CNG) as fuel. A mixer system is adopted for an injection system in the target engine to promote mixing of air and fuel since the fuel is injected in gas state. A schematic of a mixer system is shown in Figure 25. A gas is injected to the mixer, then, it is mixed with fresh air. Fresh air path is surrounded with gas path holes to make homogeneous mixture. For implementation of mixer system, a gas mass flow rate from fuel source model was adjusted to set equivalent ratio.

The intake system model consists of intake pipes, a compressor, an intercooler, a mixer, a manifold, and ports model. In each model, pressure drop was calculated from friction factor of pipe and geometrical shape. The compressor and turbine of turbocharger were implemented based on the map data. The map consists of the pressure ratio between upstream and downstream, efficiency and mass flow rate. It is important to correlate a turbine rotational speed and mass flow rate according to the temperature and pressure of working fluids because the base map data was measured in standard state. Thus, the correlation equations were adopted as bellows.

$$\omega_{corr} = \frac{\omega_{real}}{\sqrt{T/T_{st}}} \quad (3.2.1.1)$$

$$\dot{m}_{corr} = \frac{\sqrt{T/T_{st}}}{P/P_{st}} \dot{m}_{real} \quad (3.2.1.2)$$

where, subscripts of *corr*, *real* and *st* mean the corrected value, real value and standard, respectively.

Combustion model, 1-D CFM, is based on the 3D CFD ECFM (Extended Coherent Flame Model) model [52]. This model can estimate combustion phenomena more precisely compared with simple combustion model such as Wiebe model, because equations that reflect physical phenomena are used. The CFM model is specialized to the flamelet regime. This method can describe premixed combustion process which is the main oxidation mechanism in SI engines with good agreement. As described in Figure 26, combustion chamber is divided into two zones : fresh and burned gases zones. They are divided by a propagated flame front from the burned gases towards the fresh mixture. Fuel oxidation which is combustion occurs in a very thin layer (the flame front). Because 1-D CFM is based on 3-D CFM, in order to modify 1-D CFM, some assumptions are considered.

- All gases are considered as perfect gas.
- In each zone, all physical state and condition are homogeneous.
- In combustion chamber, it is assumed that the pressure is constant.

The heat release rate is calculated as below equation.

$$\frac{dQ}{dt} = LHV \cdot \dot{\omega}_{fuel} \quad (3.2.1.3)$$

where,  $LHV$  is the lower heating value of the fuel and  $\dot{\omega}_f$  is the rate of fuel consumption during combustion process. The rate of fuel consumption depends on the flame surface and the fresh gases properties as below equation.

$$\dot{\omega}_{fuel} = \rho_{fg} Y_{fg}^f U_l S_f \quad (3.2.1.4)$$

where,  $\rho_{fg}$ ,  $Y_{fg}^f$ ,  $U_l$  and  $S_f$  are the fresh gases density, fuel mass fraction in the fresh gases, laminar flame speed which is correlated with the experimental results and the flame surface, respectively. The laminar flame speed is computed based on Metghalchi and Keck's correlation [53]. The flame surface is calculated using a mean surface,  $S_m$  and the flame front wrinkling,  $\Xi$ .

$$S_f = \Xi S_m \quad (3.2.1.5)$$

Because the target engine has the plane head and piston surface, a mean flame surface is calculated assuming a spherical flame propagates and is changed into cylinder shape when the flame reaches the piston and the head wall. This propagation process is shown in Figure 27.

This combustion model is expected to be very representative of the real processes. Thus, combustion parameters which affect combustion performance such as wrinkling constant, flame wrinkling, and flame initial volume are not required to be adjusted. Only the turbulence model which is calculated from initial tumble number should be adjusted. The initial tumble number at IVC was modified to match the experimental results, because simple Damköhler's formulation [54] was used for the flame wrinkling in this study. Parameter set which was used in the model is listed in Table 3.

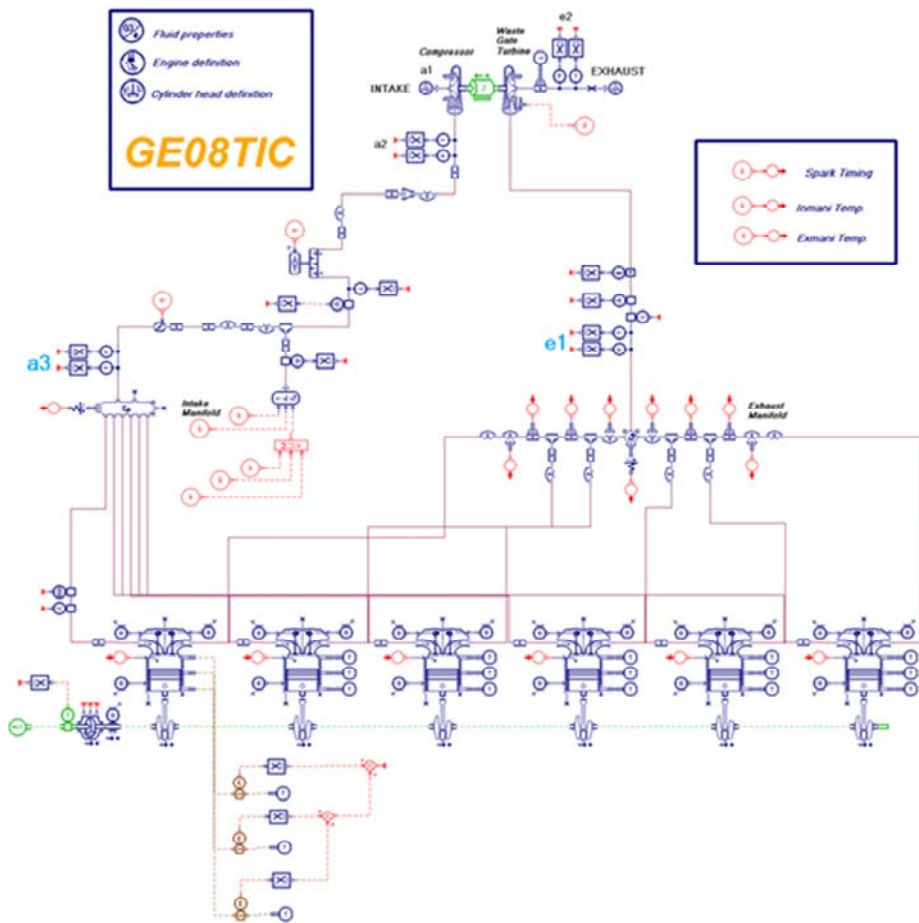


Figure 24. 1-D engine model implemented in AMESim

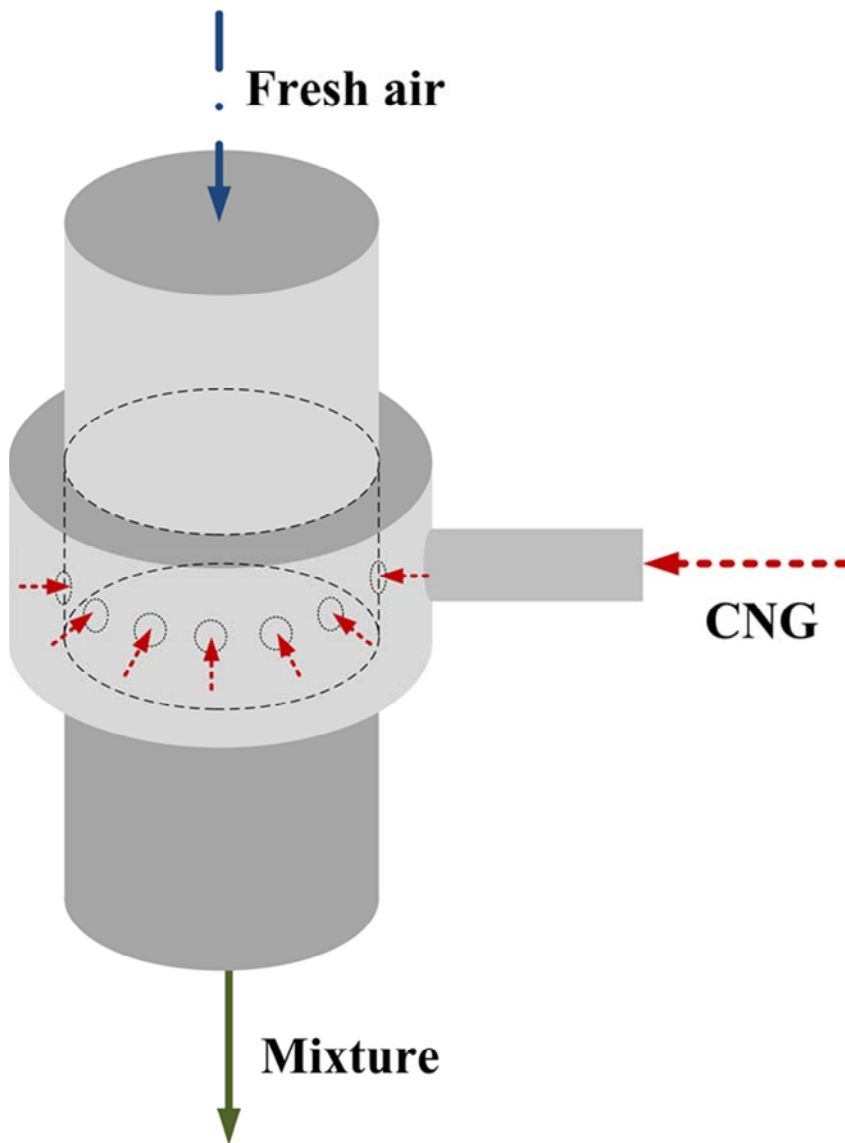


Figure 25. A schematic of gas injection system, Mixer

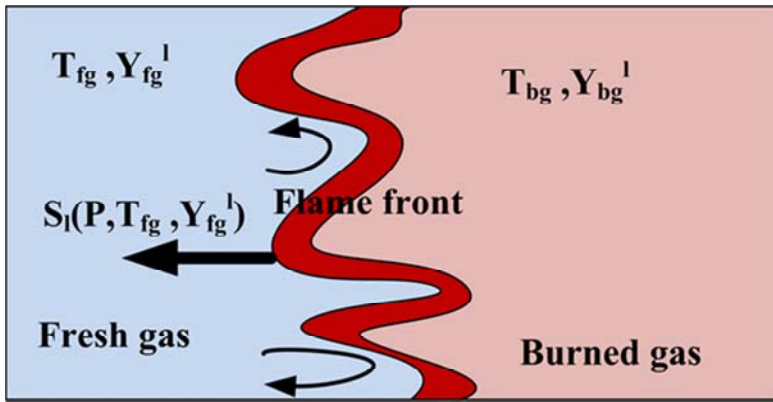


Figure 26. A schematic of coherent flame model [52]

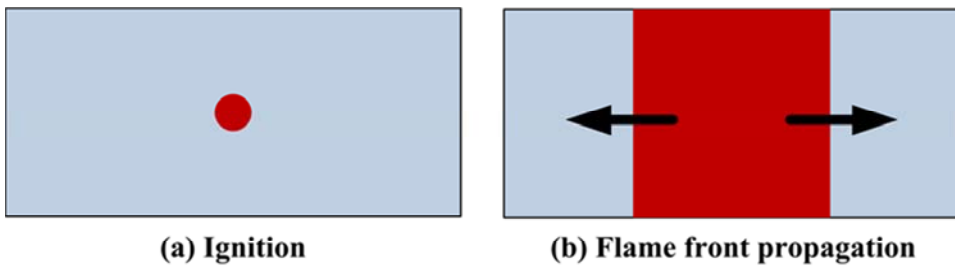


Figure 27. Ignition and propagation of flame front in the model [52]

Table 3. Parameters for the 1-D engine model

Parameter	Value
C <sub>turb</sub>	1
C <sub>diss</sub>	150
Flame initial volume (m <sup>3</sup> )	10 <sup>-6</sup>
Flame wrinkling	10
Tumble value	$\eta_{vol} \times 0.6$
Cut-off length (cm)	0.5

The results of the 1-D engine model were compared with the experimental results as listed in Tables 4 ~ 9. The engine operated on the OOL because the best fuel economy can be achieved on OOL. In fact, it is hard to operate the engine on the OOL in the conventional vehicle and parallel type HEVs because the engine is coupled with the driveshaft. However, in the series type HEVs, the engine is decoupled with the driveshaft, which enables the engine to be operated regardless to the vehicle speed and load. Thus, in this study, a validation was conducted about 6 points on the OOL. In order to determine FEMP according to engine operation speed, below equation was adopted [10].

$$FMEP = 0.97 + 0.15\left(\frac{N}{1000}\right) + 0.05\left(\frac{N}{1000}\right)^2 \quad (3.2.1.6)$$

where,  $N$  is the engine operation speed in rpm.

Table 4. Comparison between experiment and simulation (1200 rpm – 100 % load, fuel injection 5.24 g/s)

	Unit	Exp.	Sim.	Error (abs.)	Error (%)
Int. air flow	g/s	120.75	124.30	-3.55	-2.94
Exh. gas temperature	K	820.7	845.9	-25.2	-3.1
Int. air pressure	Bar (abs)	1.68	1.67	0.01	0.73
Exh. gas pressure	Bar (abs)	1.05	1.03	0.01	1.08
IMEP	bar	13.76	12.96	0.80	5.80
FMEP	bar	1.22	1.22	0.00	0.00
BMEP	bar	12.54	11.74	0.80	6.36

Table 5. Comparison between experiment and simulation (1400 rpm – 100 % load, fuel injection 6.89 g/s)

	Unit	Exp.	Sim.	Error (abs.)	Error (%)
Int. air flow	g/s	164.86	170.02	-5.16	-3.13
Exh. gas temperature	K	830.3	809.8	20.4	2.5
Int. air pressure	bar (abs)	2.00	1.99	0.00	0.07
Exh. gas pressure	bar (abs)	1.06	1.05	0.01	1.28
IMEP	bar	14.97	15.13	-0.17	-1.11
FMEP	bar	1.28	1.28	0.00	0.00
BMEP	bar	13.69	13.86	-0.17	-1.22

Table 6. Comparison between experiment and simulation (1600 rpm – 100% load, fuel injection 7.62 g/s)

	Unit	Exp.	Sim.	Error (abs.)	Error (%)
Int. air flow	g/s	184.17	181.61	2.56	1.39
Exh. gas temperature	K	845.4	842.8	2.5	0.3
Int. air pressure	bar (abs)	1.99	1.94	0.06	2.92
Exh. gas pressure	bar (abs)	1.07	1.06	0.02	1.60
IMEP	bar	14.75	14.41	0.34	2.31
FMEP	bar	1.34	1.34	0.00	0.00
BMEP	bar	13.41	13.07	0.34	2.54

Table 7. Comparison between experiment and simulation (1800 rpm – 100% load, fuel injection 8.89 g/s)

	Unit	Exp.	Sim.	Error (abs.)	Error (%)
Int. air flow	g/s	211.39	216.85	-5.46	-2.58
Exh. gas temperature	K	855.4	859.8	-4.4	-0.5
Int. air pressure	bar (abs)	2.06	2.14	-0.07	-3.50
Exh. gas pressure	bar (abs)	1.09	1.08	0.01	1.03
IMEP	bar	14.81	15.03	-0.22	-1.50
FMEP	bar	1.40	1.40	0.00	0.00
BMEP	bar	13.41	13.63	-0.22	-1.66

Table 8. Comparison between experiment and simulation (2000 rpm – 100% load, fuel injection 9.55 g/s)

	Unit	Exp.	Sim.	Error (abs.)	Error (%)
Int. air flow	g/s	227.51	228.18	-0.68	-0.30
Exh. gas temperature	K	868.5	876.3	-7.9	-0.9
Int. air pressure	bar (abs)	2.09	2.11	-0.02	-0.76
Exh. gas pressure	bar (abs)	1.10	1.09	0.01	1.08
IMEP	bar	14.11	14.31	-0.20	-1.38
FMEP	bar	1.47	1.47	0.00	0.00
BMEP	bar	12.64	12.84	-0.20	-1.54

Table 9. Comparison between experiment and simulation (2300 rpm – 100% load, fuel injection 10.18 g/s)

	Unit	Exp.	Sim.	Error (abs.)	Error (%)
Int. air flow	g/s	240.00	244.38	-4.39	-1.83
Exh. gas temperature	K	882.0	888.9	-6.9	-0.8
Int. air pressure	bar (abs)	2.15	2.12	0.03	1.20
Exh. gas pressure	bar (abs)	1.11	1.10	0.01	0.80
IMEP	bar	13.22	12.98	0.24	1.82
FMEP	bar	1.58	1.58	0.00	0.00
BMEP	bar	11.64	11.40	0.24	2.07

### **3.2.1.2 Thermal management model**

The thermal management model is used to estimate the temperature of metal part of the engine, coolant and exhaust gas. In addition, this model was used to estimate the temperature of exhaust gas at cold state. In warm up process, the heat flow from the combustion chamber to the wall is changed because the surface temperature is changed. Thus, the temperature of the exhaust gas during warming up process shows different value compared to fully warmed-up state. Moreover, a temperature drop in catalyst is greater than fully warmed-up state. To estimate these phenomena, the thermal management model was implemented in AMESim as shown in Figure 28.

The thermal management model consists of the thermal mass model, the coolant model, the lubricant model and the exhaust model. In thermal management model, heat transfer between metal parts, coolant, exhaust gas, and lubricant occur through conduction, convection, and radiation. Thus, it is very important to set up proper parameters which are related with heat transfer phenomena. In conduction, thermal conductivity and distance between each metal part are main parameters. In convection, heat transfer coefficient which is calculated from non-dimensional values such as Re and Pr and heat transfer area are main parameters. These values were determined based on architecture of the engine cooling circuit, the coolant flow rate, and the physical properties. In this study, the architecture of the cooling circuit and geometry specification were calibrated from the smaller engine. To obtain reasonable input data, the shape of the combustion chamber, total mass and length of the engine were compared and corrected. Coolant flow rate was calculated from coolant pump map, and input/output temperatures were validated with the experimental result. The overall schematic of the ETM model is described in Figure 29.

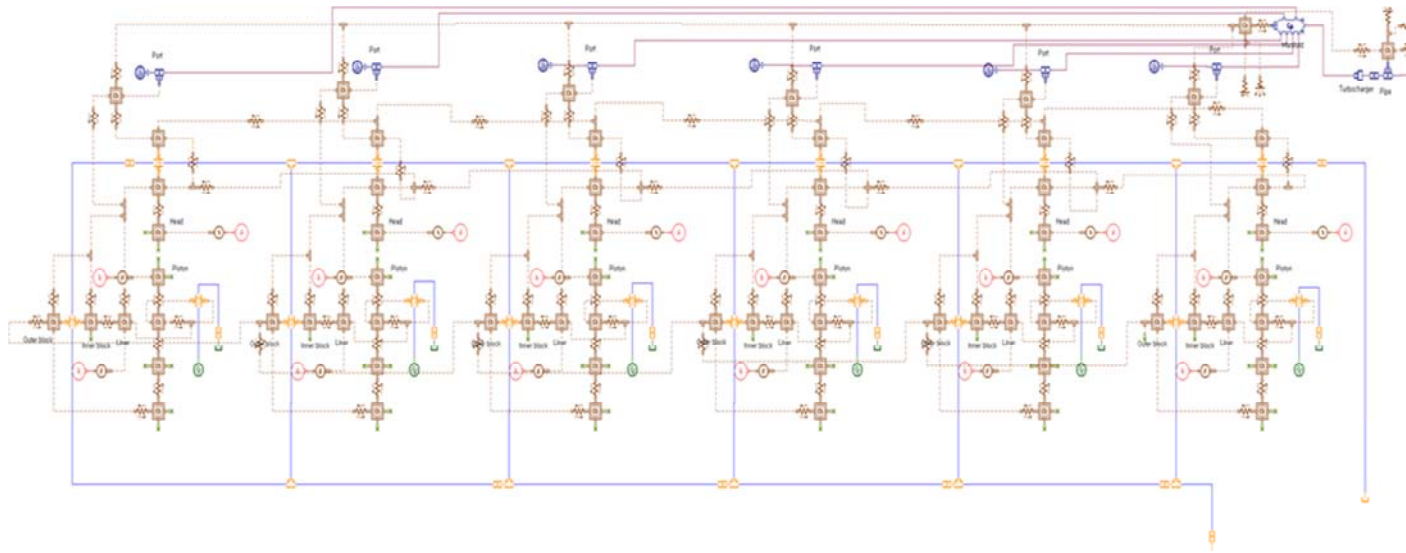


Figure 28. Thermal management model for 6-cylinder CNG engine

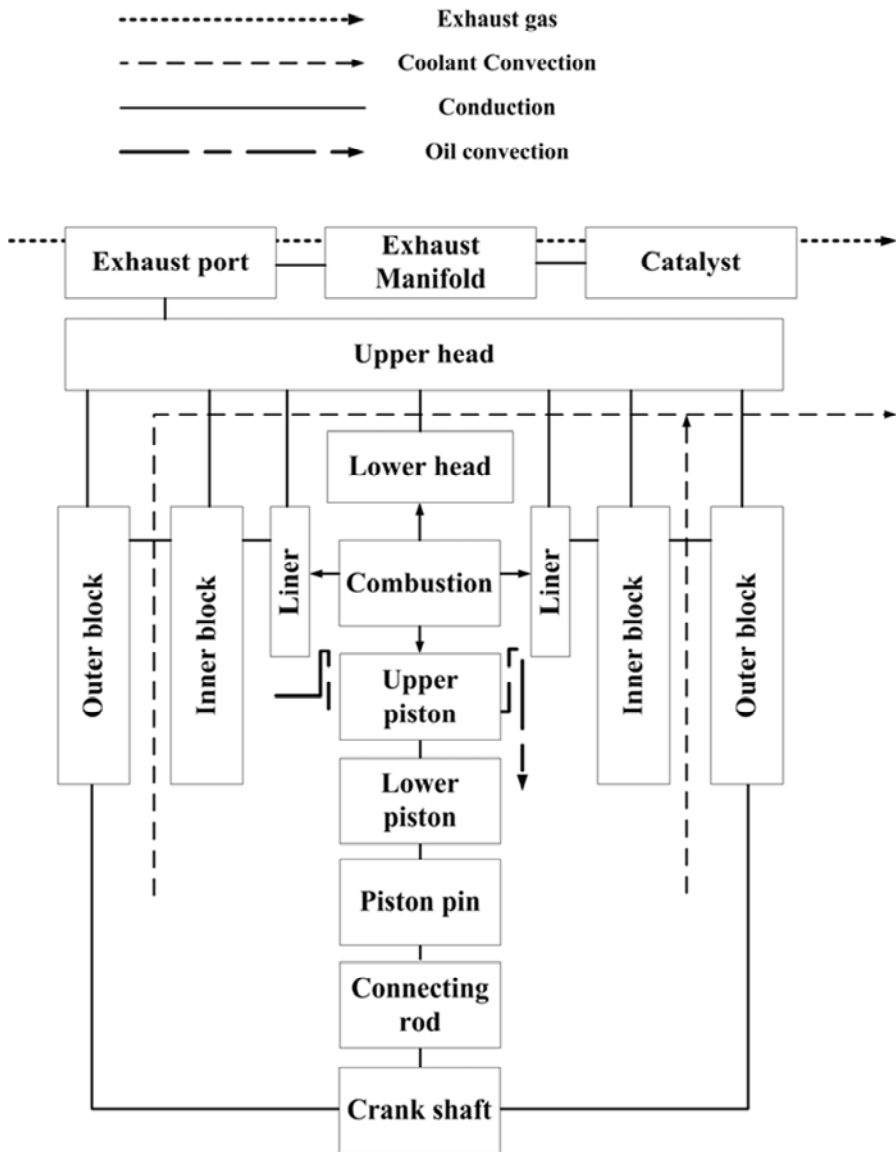


Figure 29. A schematic of ETM model

Thermal mass model consists of piston, head, liner, inner/outer block, port, crank shaft, connecting rod, exhaust manifold, and catalyst. Each part is connected with other parts through conduction model. Moreover, to investigate more detail temperature distribution, head and piston were separated into two parts, respectively. The lower part of the head is exposed to combustion heat while the upper part is exposed to the coolant. Thus, the temperature of lower part is much higher than that of the upper part. In the same sense, the upper part of piston which is exposed to combustion heat shows higher temperature than that of the lower part. The liner is surrounded with inner block. Thus liner is exposed to combustion heat directly like as the upper part of the piston and the lower part of the head. The conduction in the same part and between different parts is defined as below equations, each other [55].

$$q = \frac{Ak(T_2 - T_1)}{dist} \quad (3.2.1.7)$$

$$q = \frac{T_2 - T_1}{\frac{dist_1}{k_1 A} + \frac{dist_2}{k_2 A} + R_C} \quad (3.2.1.8)$$

In the case of the same part, the contact thermal resistance,  $R_C$ , was not considered.

A heat transfer in coolant was calculated with assumption of pipe flow. The convection heat transfer in coolant is defined as follow equations [56].

$$Nu = C_{convec} Re^{0.8} Pr^{0.33} \quad (3.2.1.9)$$

$$h_{convec} = \frac{Nu \times \lambda}{D_h} \quad (3.2.1.10)$$

where,  $Nu$  is the Nusselt number,  $\lambda$  is the thermal conductivity of the fluid and  $D_h$  is the hydraulic diameter. The heat transfer between the wall and the fluid is defined as below equation.

$$q = Ah_{convec} (T_f - T_s) \quad (3.2.1.11)$$

where,  $A$  is the heat exchange area,  $T_f$  is the fluid temperature, and  $T_s$  is the surface temperature. In addition, in this study, because a multi-cylinder engine was considered, heat transfer by convection to coolant was not the same at each cylinder. As shown in Figure 30, coolant enters at 6<sup>th</sup> cylinder block from coolant tank, and it is distributed to each cylinder based on calculation from the friction factor. Thus, the flow rate in the block of the 1<sup>st</sup> cylinder is smaller than other cylinder blocks because the length of that path is the longest. Because as the length of the coolant path increases, friction value becomes large, it is certain that the result is reasonable.

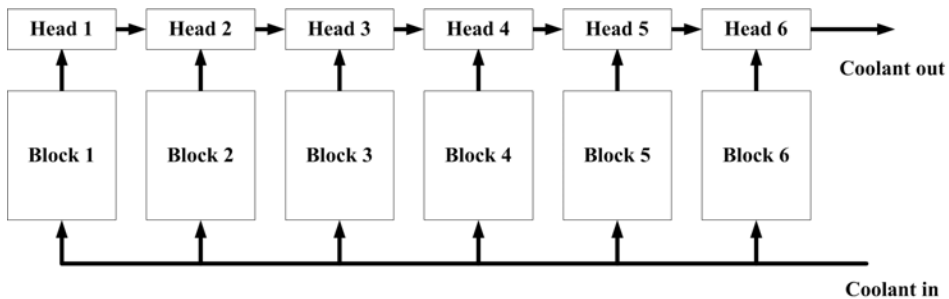


Figure 30. A schematic of the cooling circuit

The piston jet was implemented in the lubricant model. The heat transfer was calculated based on the same process of the coolant. The simulation was conducted at 2300 rpm – 100 % load point where is the maximum power. Because the heat transfer from the combustion chamber is affected by the surface temperature of the piston, the head, and the liner, iterative calculation between 1-D engine model and ETM model is needed to obtain accurate heat transfer value. Iteration process was conducted and it was confirmed that the temperature values were converged after iterations. The ETM model results at maximum power point are shown in Figure 31.

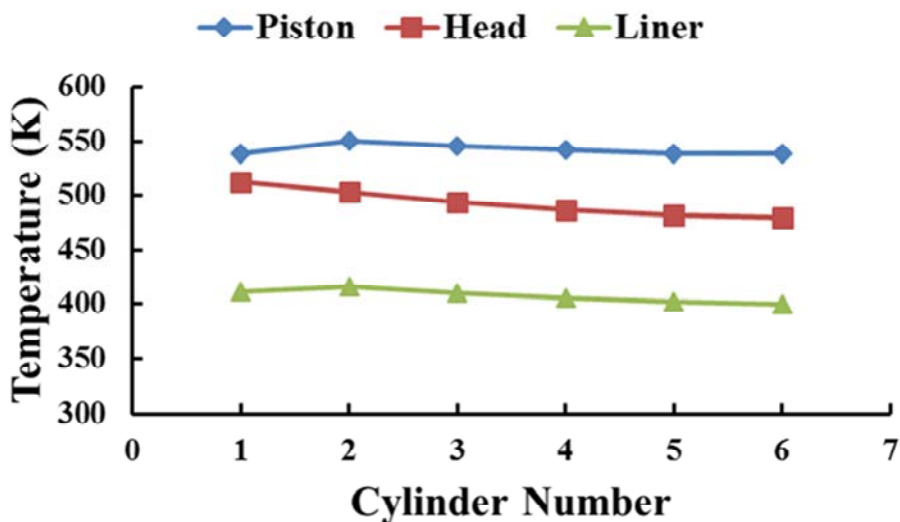


Figure 31. The distribution of temperature of each part at 2300 rpm – 100 %

As shown in Figure 31, the head shows the highest temperature difference. It is reasonable results because other similar engine has about 25 K difference temperature value of the head [57] . In this study, it showed about maximum 32

K difference. The input coolant temperature was 360.7 K and the output coolant temperature was 365.8 K. The experimental result of the output coolant temperature was 366.5 K.

### 3.2.1.3 0-D engine model

0-D engine model was used with the vehicle model. Because the computation load of the 1-D model and the ETM model is too large to be used with the vehicle model, simple 0-D model which is based on the map data was adopted. The difference compared to the conventional 0-D engine model is that the model can calculate the flow rate and the temperature of the exhaust gas for the WHRS. To simulate a delay response of the engine, first order delay model was applied. 0-D model implemented in Matlab/Simulink is shown in Figure 32.

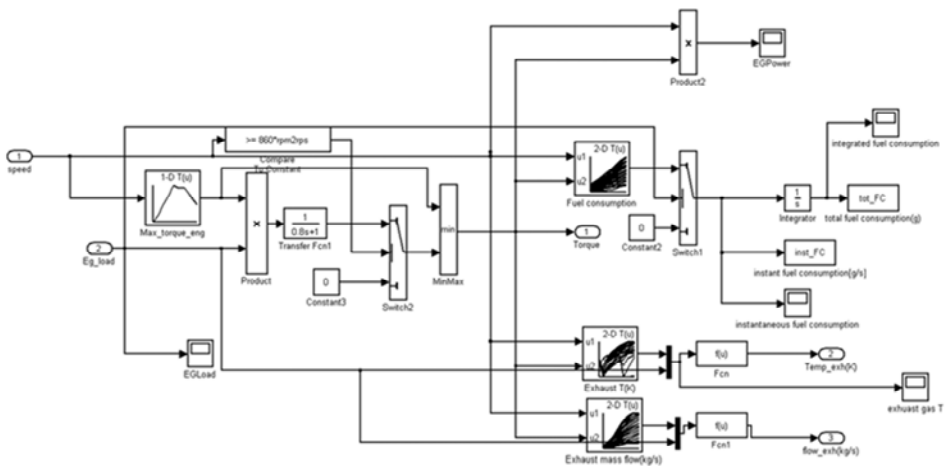


Figure 32. Implemented 0-D engine model in Matlab/Simulink

### 3.2.2 Motor and generator (M/G) models

In order to reduce computational effort, a simple map-based model was implemented for the motor and the generator. The efficiency map which is function of speed and torque of M/G includes inverter efficiency. Thus, the efficiency of overall energy conversion process from the electrical energy to the mechanical energy and opposite process can be taken into account. In addition, first order delay was applied to simulate the transient behavior. The inputs of M/G model are a required torque from traction motor control unit model and hybrid control unit model, a rotational speed and an operating voltage. The outputs of the M/G model are a torque and a current.

Maximum and minimum torque at a present speed is calculated to prevent over operation. In series HEV, the traction motor and the generator are used as both the motor and the generator. When the regenerative braking is activated, traction motor is used as generator. In contrast, the generator is used as motor at engine starting state. Thus, M/G model should calculate the motor operation and the generator operation. When the required input torque is positive, M/G model is operated as a motor. Because the first order delay is applied, a required torque is not the same compared to the output torque, instantaneously. The electric energy which is needed in M/G model was calculated as below in the motor case.

$$P_{electric} = T\omega / \eta_{mot} \quad (3.2.2.1)$$

where,  $T$ ,  $\omega$  and  $\eta_{mot}$  are the real motor torque, rotational speed and efficiency, respectively. The current was calculated with above power and input voltage. When the required input torque is negative, M/G model is operated as a generator. First order delay was considered to calculate a real torque like as

motor operation. The electric energy generated from M/G model was calculated as below in the generator case.

$$P_{electric} = \eta_{gen} T \omega \tag{3.2.2.2}$$

Where,  $\eta_{gen}$  is the efficiency of the generator. It is noted that the efficiency of each case is lower than 1. Thus, the electric energy is smaller than the mechanical energy in the generator case whereas the electric energy is larger than the mechanical energy in the motor case. The efficiency maps of the generator and the traction motor are shown in Figures 33 and 34. To achieve high efficient generator operation, reduction gear was applied between the generator and the engine. The generator shows higher efficiency than the traction motor, because the generator is PM type whereas the traction motor is ID type.

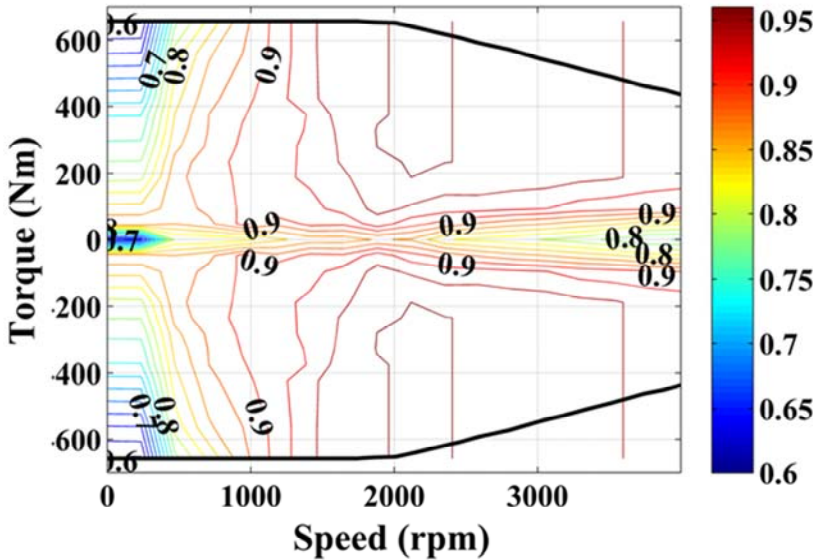


Figure 33. PM type generator efficiency

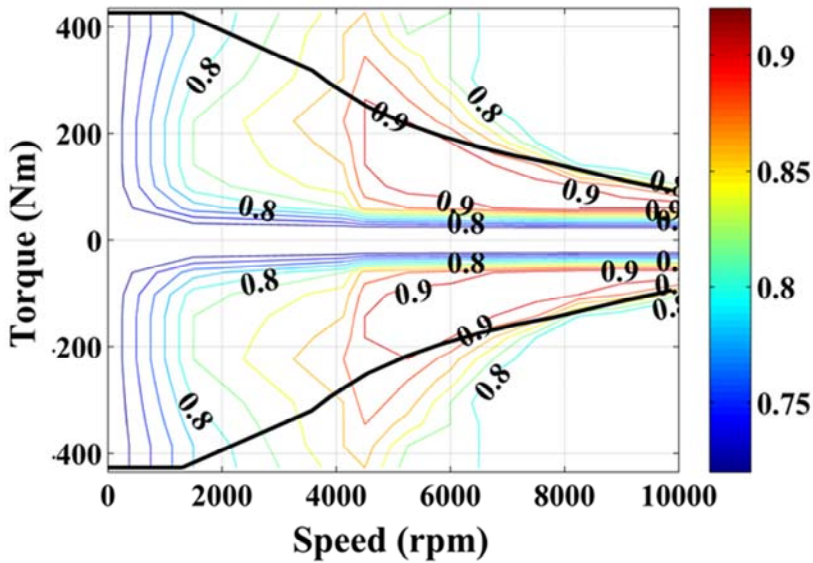


Figure 34. ID type traction motor efficiency

### 3.2.3 Battery model

The electrochemical Li-ion battery model which can estimate the internal behavior of the battery was used in this paper. Recently, to protect battery from damage, there has been effort to analyze internal behavior of Li-ion battery. Because it is difficult to estimate the internal behavior of the battery through the experiment, simulation was used to estimate that [58-60]. Especially, in the HEVs, it is important to control the battery with consideration of internal behavior, because over charge and discharge can damage the battery. The internal behavior of the battery affects the cell voltage. It means that the cell voltage is determined by the lithium ion concentration on the surface of the active material in the battery. The lithium ion moves in the battery by diffusion

process according to the input current. Therefore, sudden and large change of current causes great non-uniform distribution of the concentration in active material, which damages the battery. By adopting the electrochemical Li-ion battery model, it is possible to estimate internal behavior of battery and to protect battery from damage with the control logic [58]. The electrochemical battery model [58-60] consists of diffusion and conduction mechanisms in the active material and the electrolyte. The basic operation concept is described in Figure 35. The potential of the electrolyte and the active material are determined by Eqs. (3.2.3.1) and (3.2.3.2), respectively. The transfer of lithium ion in the battery is a diffusion process which takes much longer time than conduction of charge. Thus, the concentrations of lithium ion in the electrolyte and active material are expressed as partial differential equations as Eqs. (3.2.3.3) and (3.2.3.4) while the potential is expressed as ordinary difference equations.

$$\frac{\partial}{\partial x} (\kappa^{eff} \frac{\partial}{\partial x} \phi_e) + \frac{\partial}{\partial x} (\kappa_D^{eff} \frac{\partial}{\partial x} \ln c_e) + j^{Li} = 0 \quad (3.2.3.1)$$

$$\frac{\partial}{\partial x} (\sigma^{eff} \frac{\partial}{\partial x} \phi_s) - j^{Li} = 0 \quad (3.2.3.2)$$

$$\frac{\partial(\varepsilon_e c_e)}{\partial t} = \frac{\partial}{\partial x} (D_e^{eff} \frac{\partial}{\partial x} c_e) + \frac{1-t_+^0}{F} j^{Li} \quad (3.2.3.3)$$

$$\frac{\partial c_s}{\partial t} = \frac{D_s}{r^2} \frac{\partial}{\partial r} (r^2 \frac{\partial c_s}{\partial r}) \quad (3.2.3.4)$$

In Eqs. (3.2.3.1) – (3.2.3.4),  $c_e$  is the concentration of electrolyte,  $c_s$  is the concentration of an active material,  $\phi_e$  is the voltage of an electrolyte and  $\phi_s$  is the voltage of an active material. Boundary condition is described in Figure 36

and battery parameters are described in Table 10. The Butler-Volmer current density,  $j^{Li}$ , is defined as Eq. (3.2.3.5).

$$j^{Li}(x) = a_s j_0 \left[ \exp\left(\frac{\alpha_a F}{RT} \eta\right) - \exp\left(\frac{\alpha_c F}{RT} \eta\right) \right] \quad (3.2.3.5)$$

where,  $\eta$  is the over potential of each electrode. It is defined as Eq. (3.2.3.6)

$$\eta = \phi_s - \phi_e - U(c_{se}) \quad (3.2.3.6)$$

where,  $U(c_{se})$  is the open circuit voltage which is expressed as empirical correlation function of active material surface concentration,  $c_{se}$ . The terminal voltage is calculated as Eq. (3.2.3.7).

$$V = \phi_s(x=L) - \phi_s(x=0) - \frac{R_f}{A} I \quad (3.2.3.7)$$

where,  $R_f$  is the film resistance on an electrode surface of which value is 20 ( $\Omega \text{ cm}^2$ ) and  $I$  is the input current.

In this study, the reduced model which is solved with some assumptions was adopted. Simple information of concentration on the active material surface is sufficient to control the battery safely because it mainly has influences on open circuit voltage. Thus, the calculation load to solve all differential equations is so excessive. Further, because the battery model should be combined with the vehicle model, calculation load of that should be minimized. In the reduced model, it is assumed that there is one representative spherical active material in each electrode. Moreover, the Butler-Volmer current density is assumed as constant regardless of spatial locations. Using these assumptions, constant current density can be determined as Eq. (3.2.3.8)

$$\bar{j}^{Li} = \frac{1}{\delta} \frac{I}{A} = \frac{1}{\delta} \int_0^\delta j^{Li}(x) dx \quad (3.2.3.8)$$

From these assumptions, the battery voltage, Eq. (3.2.3.7) can be written with averaged values as Eq. (3.2.3.9).

$$V = (\bar{\eta}_p - \bar{\eta}_n) + (\bar{\phi}_{e,p} - \bar{\phi}_{e,n}) + (U_p(\theta_p) - U_n(\theta_n)) - \frac{R_f}{A} I \quad (3.2.3.9)$$

where,  $\theta = \frac{c_{se}}{c_{s,max}}$  is the normalized concentration value of active material.

$(\bar{\phi}_{e,p} - \bar{\phi}_{n,p})$  is solved as Eq. (3.2.3.10).

$$(\bar{\phi}_{e,p} - \bar{\phi}_{n,p}) = \phi_e(L) - \phi_e(0) = -\frac{I}{2Ak^{eff}} (\delta_n + \delta_{sep} + \delta_p) \quad (3.2.3.10)$$

Further, the difference of over potential is determined as Eqs. (3.2.3.11) – (3.2.3.14).

$$\bar{j}_n^{Li} = \frac{I}{A\delta_n} = a_s j_0 \left[ \exp\left(\frac{\alpha_a F}{RT} \bar{\eta}_n\right) - \exp\left(-\frac{\alpha_c F}{RT} \bar{\eta}_n\right) \right] \quad (3.2.3.11)$$

$$\bar{j}_p^{Li} = \frac{I}{A\delta_p} = a_s j_0 \left[ \exp\left(\frac{\alpha_a F}{RT} \bar{\eta}_p\right) - \exp\left(-\frac{\alpha_c F}{RT} \bar{\eta}_p\right) \right] \quad (3.2.3.12)$$

$$\bar{\eta}_n = \frac{RT}{\alpha_a F} \ln\left(\xi_n + \sqrt{\xi_n^2 + 1}\right) \quad (3.2.3.13)$$

$$\bar{\eta}_p = \frac{RT}{\alpha_a F} \ln\left(\xi_p + \sqrt{\xi_p^2 + 1}\right) \quad (3.2.3.14)$$

$$\xi = \frac{\bar{j}^{Li}}{2a_s j_0} \quad (3.2.3.15)$$

where,  $R$  is the universal gas constant,  $F$  is the faraday's constant and  $T$  is the battery temperature. Consequently, the battery voltage can be written as below equation.

$$V = \frac{RT}{\alpha_a F} \ln \frac{\xi_n + \sqrt{\xi_n^2 + 1}}{\xi_p + \sqrt{\xi_p^2 + 1}} - \frac{I}{2Ak^{eff}} (\delta_n + \delta_{sep} + \delta_p) + (U_p(\theta_p) - U_n(\theta_n)) - \frac{R_f}{A} I \quad (3.2.3.16)$$

This battery model was validated with the experiment results and the results are shown in Figure 37.

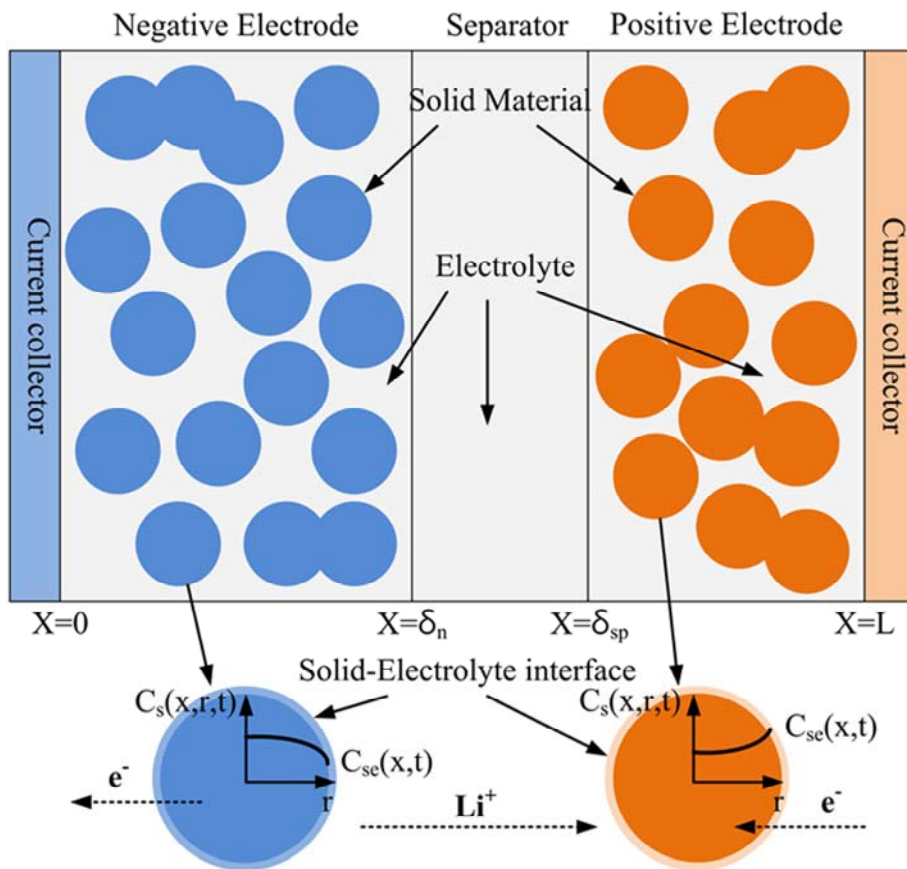


Figure 35. A schematic of the Li-Ion electrochemical model

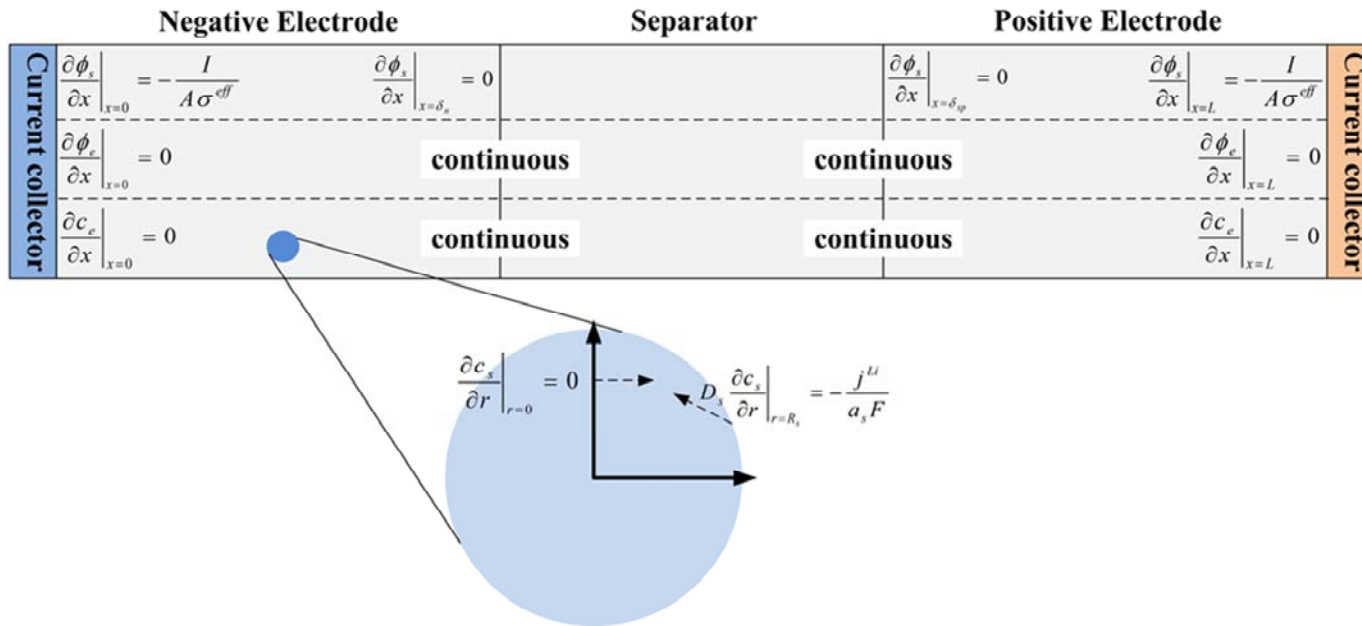


Figure 36. A boundary condition of electrochemical battery model

Table 10. Battery parameters

Parameter	Negative electrode	Separator	Positive electrode
Thickness (cm)	$\delta_n=50 \times 10^{-4}$	$\delta_{sep}=25.4 \times 10^{-4}$	$\delta_p=36.4 \times 10^{-4}$
Particle radius $R_s$ (cm)	$1 \times 10^{-4}$	-	$1 \times 10^{-4}$
Active material volume fraction $\varepsilon_s$	0.580	-	0.500
Electrolyte phase volume fraction (porosity) $\varepsilon_e$	0.332	0.5	0.330
Conductivity of solid active material $\sigma$ ( $\Omega^{-1}\text{cm}^{-1}$ )	1	-	0.1
Effective conductivity of solid active material	$\sigma^{eff} = \varepsilon_s \sigma$	-	$\sigma^{eff} = \varepsilon_s \sigma$
Transference number $t_+^0$	0.363		
Electrolyte phase ionic conductivity $\kappa$ ( $\Omega^{-1}\text{cm}^{-1}$ )	$\kappa = 0.0158 c_e \exp(0.85 c_e^{1.4})$		

Effective electrolyte phase ionic conductivity	$\kappa^{eff} = (\varepsilon_e)^{1.5} \kappa$		
Effective electrolyte phase diffusion conductivity	$\kappa_D^{eff} = 2 RT \kappa^{eff} (t_+^0 - 1) / F$		
Electrolyte phase diffusion coefficient $D_e$ (cm <sup>2</sup> s <sup>-1</sup> )	$2.6 \times 10^{-6}$	$2.6 \times 10^{-6}$	$2.6 \times 10^{-6}$
Effective electrolyte phase diffusion coefficient	$D_e^{eff} = (\varepsilon_e)^{1.5} D_e$		
Solid phase diffusion coefficient $D_s$ (cm <sup>2</sup> s <sup>-1</sup> )	$2.0 \times 10^{-12}$	-	$3.7 \times 10^{-12}$
Maximum solid-phase concentration $c_{s,max}$ (mol cm <sup>-3</sup> )	$16.1 \times 10^{-3}$	-	$23.9 \times 10^{-3}$
Stoichiometry at 0% $\theta_{0\%}$	0.26	-	0.903
Stoichiometry at 100% $\theta_{100\%}$	0.676	-	0.442
Average electrolyte concentration $\bar{c}_e$ (mol cm <sup>-3</sup> )	$1.2 \times 10^{-3}$		

Charge transfers coefficients $\alpha_a, \alpha_c$	0.5, 0.5	-	0.5, 0.5
Active surface area per electrode unit volume $a_s$ ( $\text{cm}^{-1}$ )	$a_{s_n} = 3 \varepsilon_e / R_s$	-	$a_{s_p} = 3 \varepsilon_e / R_s$
Electrode plate area $A$ ( $\text{cm}^2$ )	10,452	-	10,452

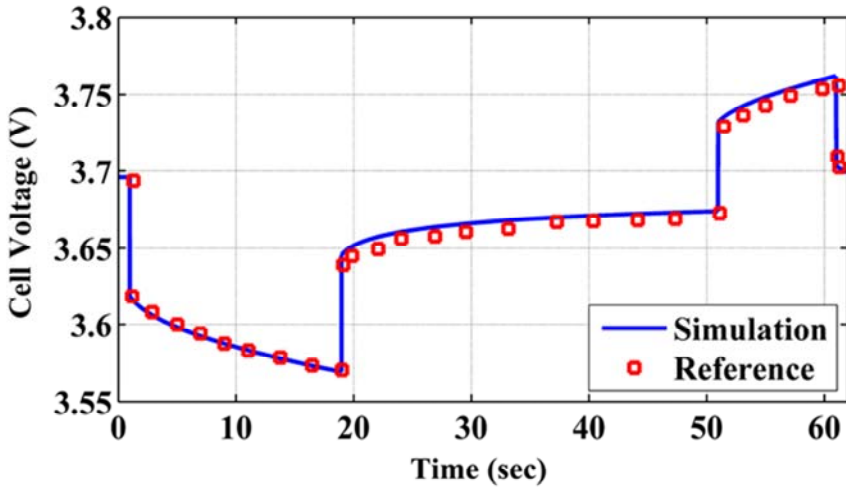
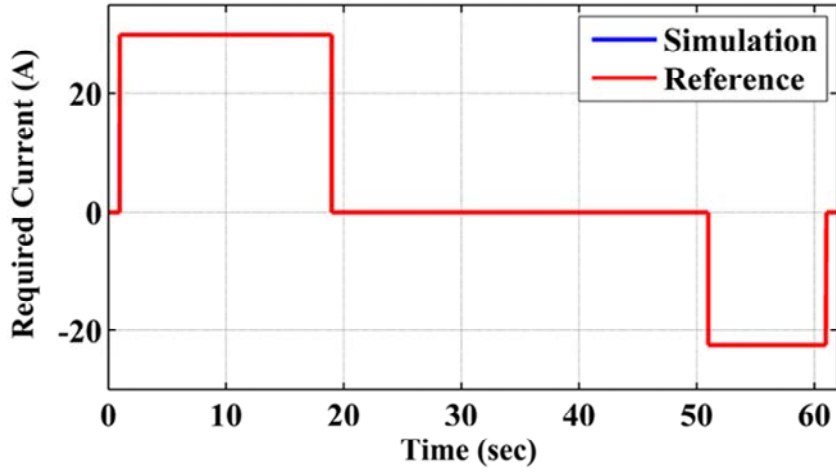


Figure 37. Validation of the averaged electrochemical Li ion battery model

### 3.2.4 Model of waste heat recovery

#### 3.2.4.1 Heat exchanger model

In order to simulate phase change of working fluids in heat exchanger according to longitudinal direction, a quasi-1D heat exchanger model has been developed. This model consists of 0-D nodes which simulate the heat transfer process with single and two phase working fluid. As described in Figure 38, the 0-D nodes were arranged along the length direction. Thus, distributions of temperature, gas fraction of working fluid along length direction can be estimated. Each 0-D model consists of an exhaust gas side and a working fluid side.



Figure 38. Schematic of quasi-1D heat exchanger model

The heat transfer coefficient of heat exchanger which has fins on heat transfer surface can be calculated as below equation [61].

$$h = St \times G \times c_p \quad (3.2.4.1)$$

where,  $St$  is the Stanton number,  $G$  is the exchanger flow-stream mass velocity, and  $c_p$  is the specific heat at constant pressure.  $St$  was obtained from tables

corresponding to the basic geometry of the surface and was supplied in the form of  $St \cdot Pr^{2/3}$  as a function of  $Re$  [61]. Moreover, the values of  $St \cdot Pr^{2/3}$  in reference were validated with the experimental data. Thus, the heat transfer coefficient calculated in this study has reliability.  $Re$  and  $G$  are determined in the model as below equations.

$$Re = \frac{4r_h G}{\mu} \quad (3.2.4.2)$$

$$G = \frac{\dot{m}}{A_{freeflow}} \quad (3.2.4.3)$$

where  $r_h$ ,  $A_{freeflow}$  and  $\mu$  are the hydraulic radius, the free flow area and the viscosity of fluid, respectively. When the working fluid is in a single phase, the heat transfer coefficient is calculated based on above equations. However, the boiling state that the working fluid is two-phase state should be calculated because calculation method to determine heat transfer coefficient is not the same to single phase case. Thus, when the working fluid is two-phase state, a boiling correlation is applied. For simplicity, Chen's correlation [62], which shows a difference of  $\pm 11.6\%$  in the two-phase heat transfer coefficient of the circular tube compared with the experimental results, was adopted to estimate the two-phase heat transfer coefficient. The convective and nucleate boiling contributions are calculated and combined as below.

$$h_{TP} = F \cdot h_{conv} + S \cdot h_{nucleate} \quad (3.2.4.4)$$

Each term in above equation is determined as below equations.

$$h_{conv} = 0.023 \cdot Re_L^{0.8} Pr_L^{0.4} \left( \frac{K_L}{D_h} \right) \quad (3.2.4.5)$$

$$F = 2.35 \left[ \frac{1}{X_w} + 0.213 \right]^{0.736} \quad (3.2.4.6)$$

where,

$$X_w = \left( \frac{1-x}{x} \right)^{0.9} \left( \frac{\rho_G}{\rho_L} \right)^{0.5} \left( \frac{\mu_L}{\mu_G} \right)^{0.1} \quad (3.2.4.7)$$

$$h_{nucleate} = 0.00122 \frac{K_L^{0.79} c_{p,L}^{0.45} \rho_L^{0.49}}{\sigma^{0.5} \mu_L^{0.29} h_{fg}^{0.24} \rho_G^{0.24}} (T_w - T_{sat})^{0.24} \Delta P_{sat}^{0.75} S \quad (3.2.4.8)$$

$$S = (1 + 2.53 \cdot 10^{-6} (\text{Re}_L F^{1.25})^{1.17})^{-1} \quad (3.2.4.9)$$

According to an average state of each node, the proper heat transfer coefficient is selected and is used to calculate the heat flow. The heat transfer between the exhaust gas, the working fluid, and the heat exchanger wall is calculated based on below equation.

$$q = hA(T_{flow} - T_{wall}) \quad (3.2.4.10)$$

The output temperature of each flow in each node is determined as below equation.

$$T_{out} = T_{in} + \frac{q}{c_p \dot{m}} \quad (3.2.4.11)$$

To estimate the surface temperature of the metal, a lumped method is applied, and the conduction between each node is considered. The surface temperature is defined as below.

$$T_{wall} = \frac{\int_0^t (q_i) dt}{m \cdot C} \quad (3.2.4.12)$$

The quasi-1D simulation model was implemented in Matlab/Simulink<sup>®</sup> and is shown in Figure 39. The implemented model consists of exhaust gas side, working fluid side and thermal mass.

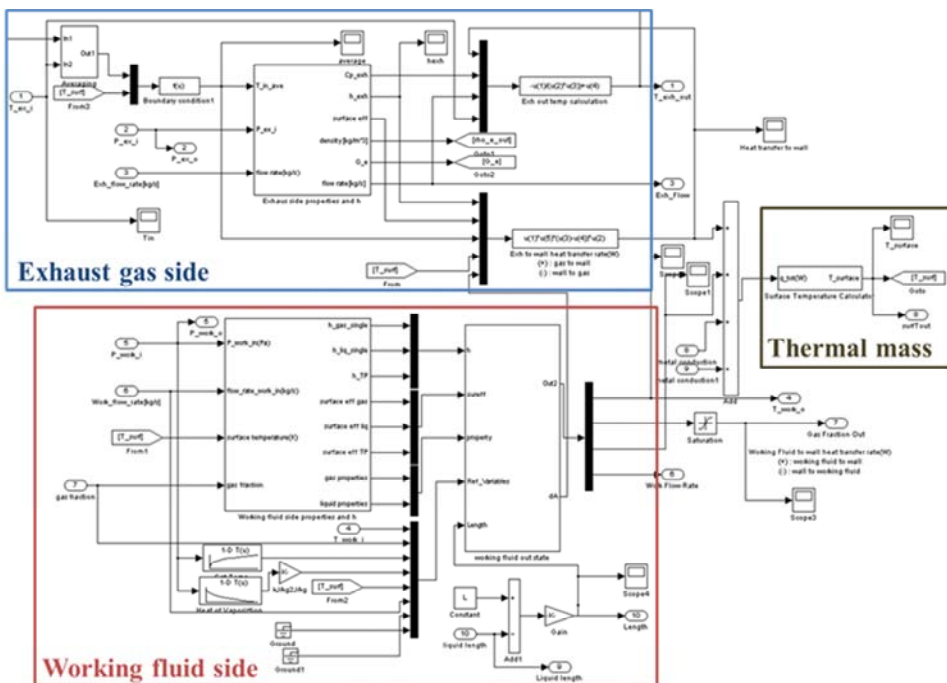


Figure 39. Heat exchanger model implemented in Matlab/Simulink

### 3.2.4.2 Turbine model

The turbine model is based on the velocity diagram and the Euler turbine equation [63]. In the turbine, only tangential component of the working fluid flow is used to produce a work. It means that the change of momentum of the tangential component work fluid between the flow inlet and outlet can be applied to calculate the force on the turbine rotor. Then, the work of the turbine can be calculated from the forces and the torques. The net tangential force and torque of the turbine with an input/output radius  $r_1$ ,  $r_2$  and a tangential component of the absolute velocity  $C_{\theta 1}$  and  $C_{\theta 2}$  are determined as follow equations.

$$F = \dot{m}(C_{\theta 1} - C_{\theta 2}) \quad (3.2.4.13)$$

$$T = \dot{m}(r_1 C_{\theta 1} - r_2 C_{\theta 2}) \quad (3.2.4.14)$$

From above equations, the energy transferred from working fluid to the turbine blade can be determined as follow equation.

$$W_{turbine} = \dot{m} \omega (r_1 C_{\theta 1} - r_2 C_{\theta 2}) = \dot{m} (u_1 C_{\theta 1} - u_2 C_{\theta 2}) \quad (3.2.4.15)$$

where,  $u_i$  is the tangential speed. Then, Euler's equation can be defined from Eq. (3.2.4.15).

$$\frac{W_{turbine}}{\dot{m}} = u_1 C_{\theta 1} - u_2 C_{\theta 2} \quad (3.2.4.16)$$

In the turbine model, the torque of the turbine is calculated based on Euler's equation.

In this study, the radial type turbine was adapted because that type is used generally rather than the axial type turbine in the mid-size generation system. In

addition, multi-stage was considered to enable to achieve the high pressure ratio. To implement the turbine model, the velocity diagram of the radial type turbine should be taken into account. The velocity diagram shown in Figure 40 is the basic concept to describe the turbo-machines. The inlet tangential component speed of the working fluid is determined from the absolute inlet speed and inlet angle. Euler`s equation can be simplified by assuming that the swirl of the outlet fluid is zero and the inlet blade angle is zero. Thus, Euler`s equation of the radial type turbine can be defined as Eq. (3.2.4.17).

$$\frac{W_{turbine}}{\dot{m}} = \Delta h_{turbine} = u_1 C_{\theta 1} = C_{\theta 1}^2 \quad (3.2.4.17)$$

From above equation, the inlet tangential component speed was determined, then, turbine torque was calculated. Consequently, the speed of working fluid flow was calculated based on difference between inlet and outlet enthalpy of the working fluid. However, in expansion process, which the thermal energy is converted into the mechanical energy, losses are occurred. Thus, the enthalpy drop level of real turbine is smaller than that of ideal turbine. Thus, the experimental efficiency which is suggested by Rohlick was applied to calculate enthalpy drop. Thus, torque of the turbine is determined as Eq. (3.2.4.18).

$$T = r_1 \dot{m} C_{\theta 1} = r_1 \dot{m} \sqrt{\eta_{turbine} \Delta h_{turbine}} \quad (3.2.4.18)$$

where,  $\eta_{turbine}$  is the efficiency of the turbine. Torque is summed up with generator torque. Then, the rotational acceleration is calculated with inertia of the turbine and the generator. Finally, a rotational speed of the turbine is calculated.

$$\omega = \int \frac{T_{\text{turbine}} - T_{\text{generator}}}{I} dt \quad (3.2.4.19)$$

Based on above equations, the turbine model was implemented. In addition, to improve efficiency of overall cycle by increasing pressure ratio, multi-stage turbine was implemented. The difference between final stage turbine and the other stage turbine is that the final stage turbine model uses total-to-static efficiency whereas other stage turbine model uses total-to-total efficiency. It is because the outlet working fluid of final stage turbine has kinetic energy which can be used to generate work while that of other stage is used in next stage turbine. The overall turbine model is shown in Figure 41.

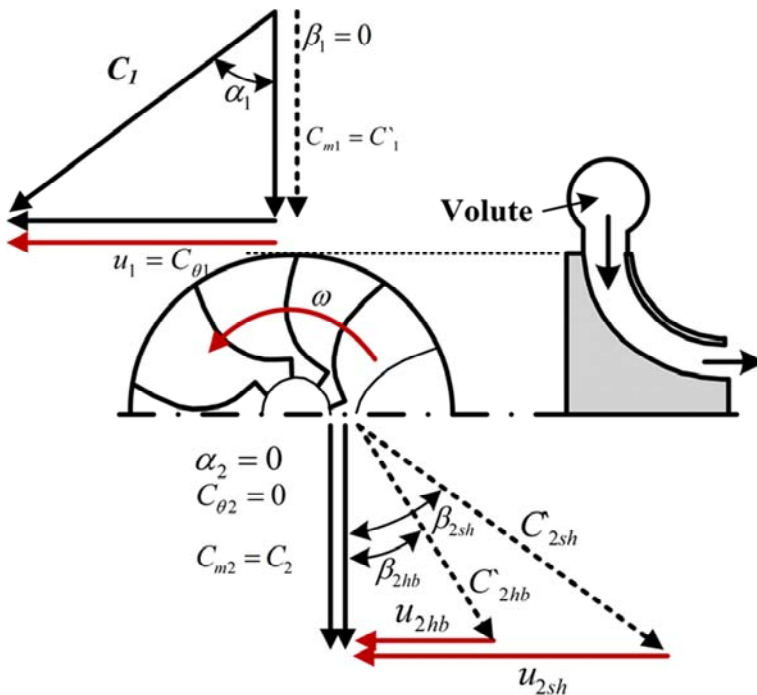


Figure 40. Velocity diagram of the radial type turbine

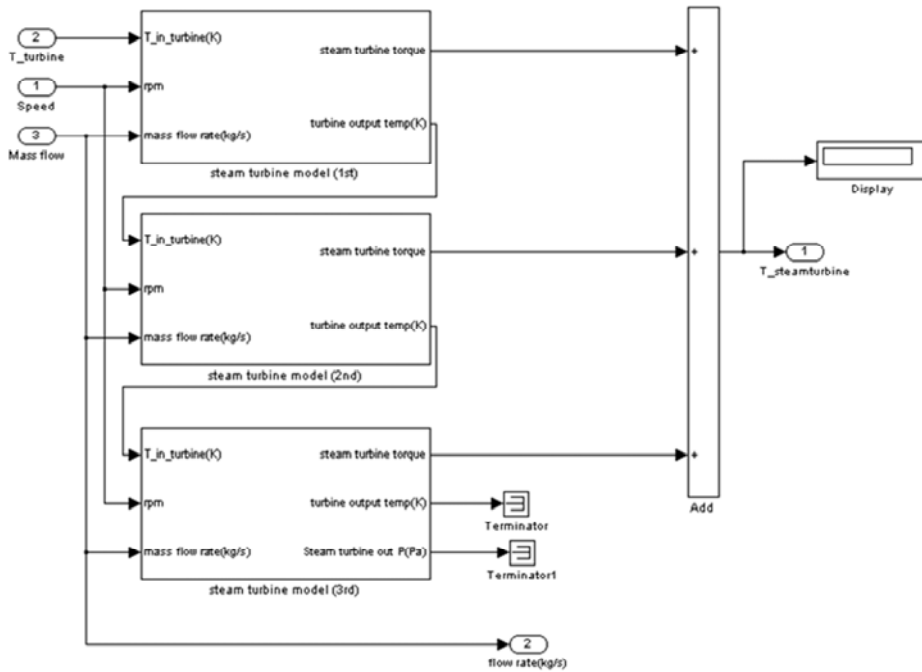


Figure 41. The turbine model implemented in Matlab/Simulink

### 3.2.4.3 Condenser and pump models

The condenser and the pump were implemented as 0-D simple model. The pump model calculated pump work from constant efficiency and enthalpy increase. The pump converts saturated liquid into compressed liquid. The pump work is calculated as Eq. (3.2.4.20). Each enthalpy is calculated based on the pressure, temperature and entropy.

$$W_{pump} = \frac{\dot{m}(h_{pump,out} - h_{pump,in})}{\eta_{pump}} \quad (3.2.4.20)$$

The condenser model calculated cooling heat after turbine process. In condenser, superheated or saturated vapor should be converted into saturated liquid. Thus, the heat should be removed from the working fluid. It is calculated based on the difference of inlet and outlet enthalpy as Eq. (3.2.4.21).

$$Q_{condenser} = \dot{m}(h_{con,out} - h_{con,in}) \quad (3.2.4.21)$$

### 3.3 Vehicle model

#### 3.3.1 Vehicle longitudinal dynamic model

In this study, the target vehicle is operated in a specific test cycle such as Heavy-Duty UDDS, Braunschweig and JE05 and only fuel economy was estimated. Thus, only longitudinal motion was taken into account to simulate the vehicle dynamics. The vehicle model consists of drag force model and brake model. When the vehicle is driving, air drag force, rolling resistance force and hill climbing force are activated on the vehicle. Each drag force is defined as below equations.

$$F_{air} = \frac{1}{2} A_f \rho_{air} C_D V^2 \quad (3.3.1)$$

$$F_{rolling} = mg\mu \cos \theta \quad (3.3.2)$$

$$F_{Hill} = mg \sin \theta \quad (3.3.3)$$

Based on Newton's law, the vehicle dynamics can be defined as Eq. (3.3.4).

$$F_{veh} = ma = F_{traction} - (F_{air} + F_{rolling} + F_{Hill}) \quad (3.3.4)$$

From above equation, acceleration of the vehicle is determined, then, the vehicle speed can be calculated by integrating the acceleration.

$$a = \frac{F_{traction} - (F_{air} + F_{rolling} + F_{Hill})}{m} \quad (3.3.5)$$

$$V = \int a dt \quad (3.3.6)$$

In accelerating state or constant speed condition, a value of acceleration is positive or zero. In decelerating condition, a value of acceleration is negative until vehicle speed becomes zero. To simulate deceleration and stopping process in the vehicle model, simulating a braking process is necessary. Thus, braking model was implemented using hyperbolic tangent function which reduces braking force as vehicle speed becomes zero. If it is not considered, vehicle speed becomes negative because the braking force is activated as negative force when the vehicle speed is almost zero. Thus, the actual braking force is function of the vehicle speed as below equation.

$$F_{b,actual} = F_b \tanh\left(\frac{V}{gain}\right) \quad (3.3.7)$$

In above equation, a *gain* was adopted to implement smooth deceleration. A hyperbolic tangent function according to the vehicle speed is shown in Figure 42.

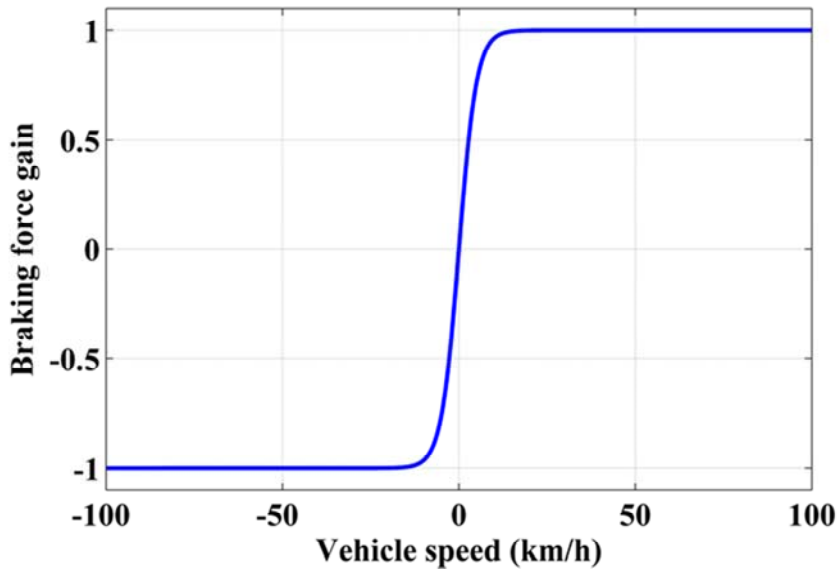


Figure 42. Hyperbolic tangent function for braking force gain

### 3.3.2 Regenerative braking algorithm

In the HEV, a regenerative braking is important to improve the fuel economy by recovering the kinetic energy of the vehicle. Thus, by recovering kinetic energy through regenerative braking, high fuel economy can be achieved. However, to ensure the vehicle stability during the braking process, the regenerative braking algorithm should be calculated with consideration of vehicle dynamics. In order to keep vehicle stability, the braking force is distributed into front and rear side axles. The force acting on a vehicle during braking process is shown in Figure 43.

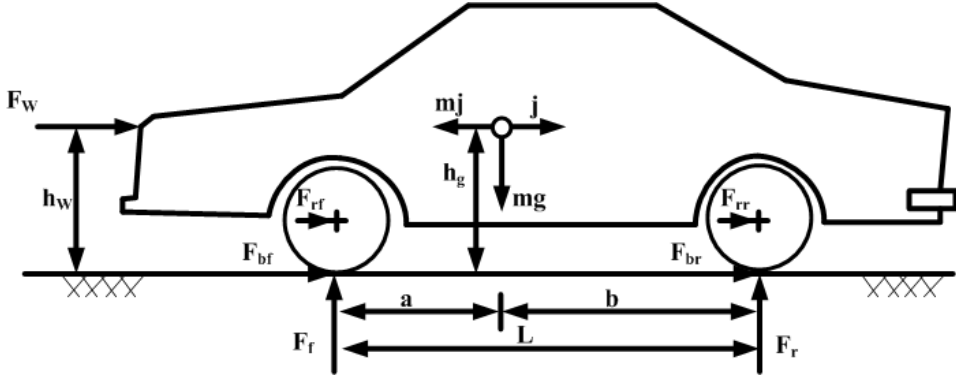


Figure 43. Forces acting on a vehicle during braking process [64]

The normal forces activated on front and rear wheels are defined as below equation based on the equilibrium of moments [64].

$$F_f = \frac{1}{L} \left[ (mgb + mgh_g \left( \frac{j}{g} - f_r \frac{r}{h_g} \right) - F_W h_W \right] \quad (3.3.8)$$

$$F_r = \frac{1}{L} \left[ (mga - mgh_g \left( \frac{j}{g} - f_r \frac{r}{h_g} \right) + F_W h_W \right] \quad (3.3.9)$$

where,  $j$  is the deceleration,  $f_r$  is the tire rolling resistance coefficient,  $r$  is tire radius, and  $F_W$  is the aerodynamic resistance, respectively. However, tire rolling resistance and aerodynamic resistance are much smaller than inertial force. Thus, Eqs. (3.3.8) and (3.3.9) can be reduced as below equations.

$$F_f = \frac{mg}{L} \left( b + h_g \frac{j}{g} \right) \quad (3.3.10)$$

$$F_r = \frac{mg}{L} \left( a - h_g \frac{j}{g} \right) \quad (3.3.11)$$

Because the braking forces are proportional to the normal force, the ratio between front and rear braking forces can be determined as Eq. (3.3.12) and the relationship between total braking force and the vehicle force can be defined as Eq. (3.3.13)

$$\frac{F_{bf}}{F_{br}} = \frac{b + h_g \frac{j}{g}}{a - h_g \frac{j}{g}} \quad (3.3.12)$$

$$F_{bf} + F_{br} = mgj \quad (3.3.13)$$

By using Eq. (3.3.13) to remove  $j$  in Eq. (3.3.12), the relationship between  $F_{br}$  and  $F_{bf}$  can be defined as Eq. (3.3.14)

$$F_{bf} = \frac{a - \frac{2h_g}{mg} F_{br} - \sqrt{a^2 - \frac{4h_g L}{mg} F_{br}}}{\frac{2h_g}{mg}} \quad (3.3.14)$$

Using Eq. (3.3.14), optimal braking line of the target system can be obtained as shown in Figure 44. The diagonal lines in the figure mean deceleration level. However, the optimal braking line can be implemented when the rolling resistance coefficient is constant. In other words, it is impossible to achieve optimal braking in the real world as calculation results. Thus, dot line which will be applied in the real world was determined. In this study, the

distribution of front and rear braking according to the deceleration was determined as dot line.

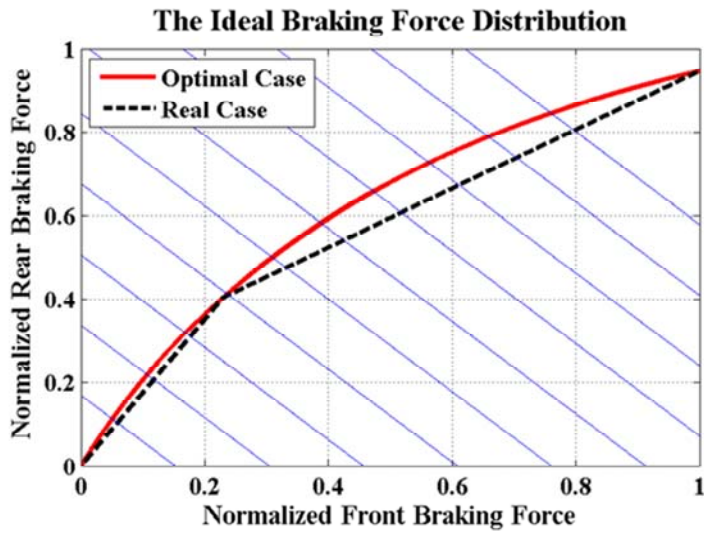


Figure 44. Braking force distribution strategy for the target vehicle

The braking line means summation of regenerative braking and friction braking forces. To recover more kinetic energy from the vehicle, the regenerative braking is maximized with minimization of the friction braking. However, the regenerative braking is limited because of vehicle stability and safety.

To ensure the vehicle stability, the front braking is activated earlier than rear braking when the driver pushes the braking pedal. Thus, only front braking was activated when the braking process was started. Moreover, in low speed range, it is very hard to control the motor, safely. Therefore, only friction braking was activated at low speed.

### **3.4 Validation of vehicle model**

The developed models were validated with the experimental data. In order to confirm physical validity of model, energy values which were used in each component were calculated and compared. The experiment has been conducted in heavy-duty chassis dynamometer and battery energy was measured by external device. The torques and speeds of the engine, the traction motor, and the generator were measured from ECU (Electric Control Unit). Fuel consumption was measured and calculated based on CVS-method (Constant Volume Sampling). A test mode which was applied to the experiment was KATECH G mode that represents driving features of intra-city bus in Seoul, Korea.

As shown in Figure 45, the vehicle speed of model traced out the experimental result with good agreement. Moreover, the main purpose of this validation is to confirm the reliability of physical behavior of mathematical model. Thus, a control strategy which determines the operation of the generation system and magnitude of regenerative brake reflected that of target vehicle. Especially, because the target vehicle adopted simple on/off control strategy that determines operation of generation system only according to battery SOC, it is possible to reproduced control strategy of target vehicle in the vehicle simulation. Thus, an engine on/off time, engine operating duration, and operation region of engine, traction motor and generator shows good agreement with the experimental result. They are shown in Figures 46 ~ 48. In addition, because SOC trajectory of the experiment and simulation shows similar trends as shown in Figure 49, it is certain that the control strategy of the target vehicle was reproduced in simulation perfectly.

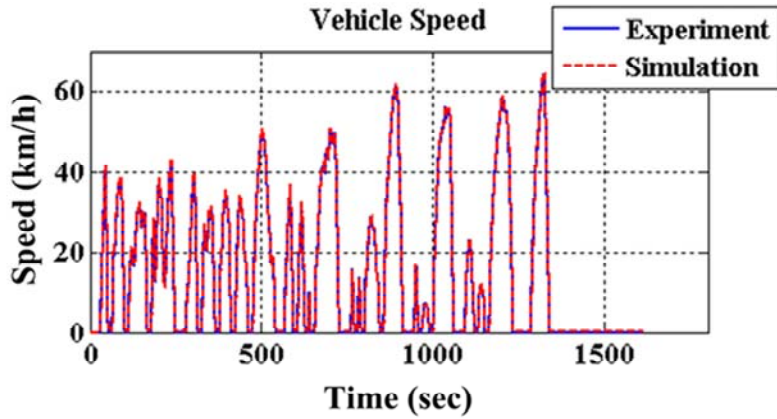


Figure 45. Validation result of vehicle speed in KATECH G mode

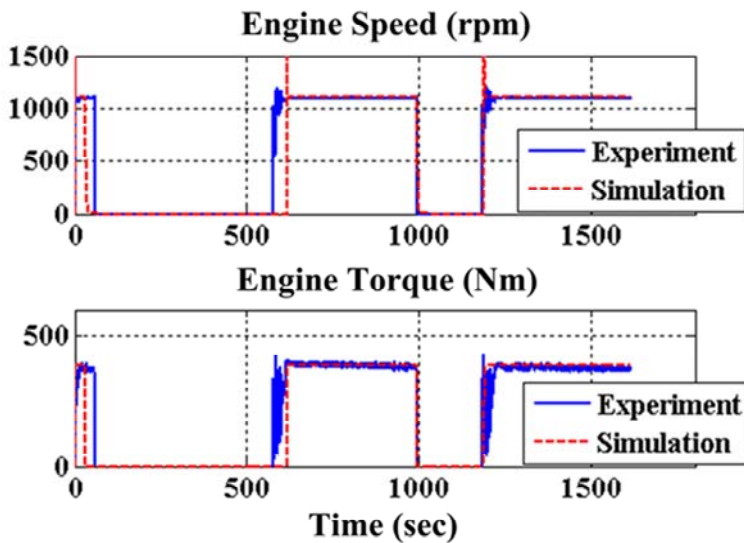


Figure 46. Validation results of the engine speed and torque in KATECH G mode

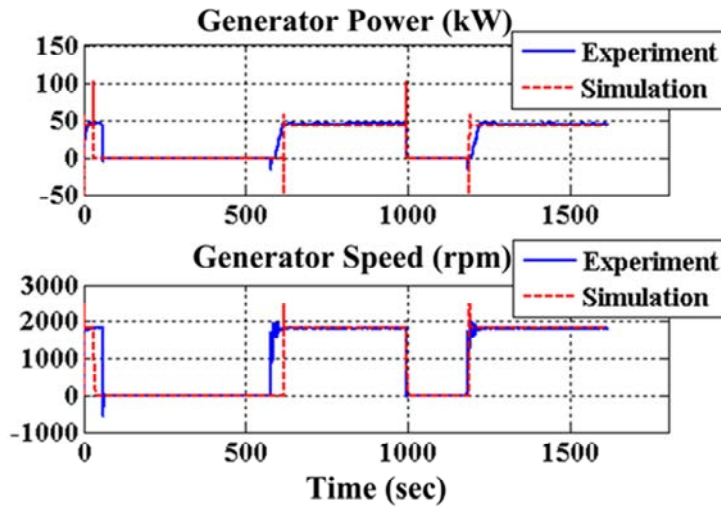


Figure 47. Validation results of the generator electric power and speed in KATECH G mode

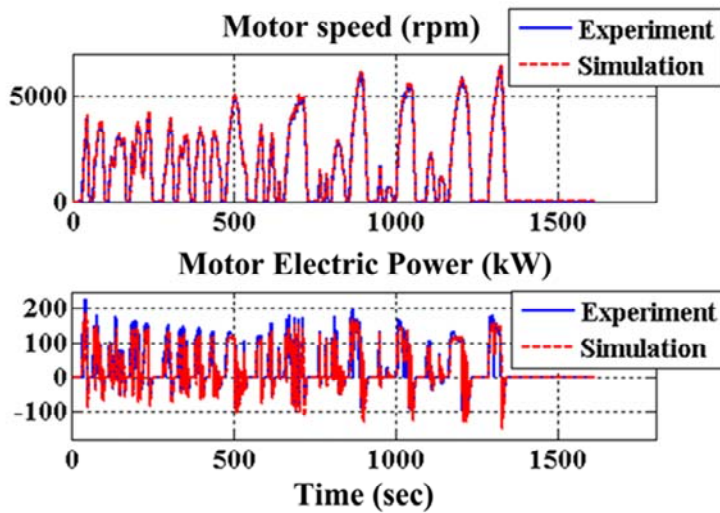


Figure 48. Validation results of the motor speed and electric power in KATECH G mode

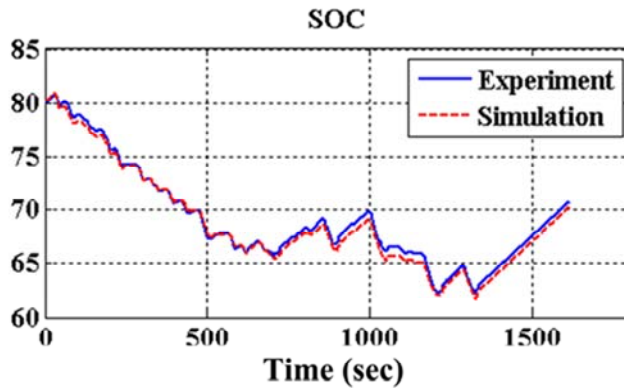


Figure 49. Validation result of SOC trajectory in KATECH G mode

Energy quantities are calculated and compared. The results of calculation are listed in Table 11.

Table 11. Validation results of energy balance of each component

	Experiment	Simulation	Error (%)
Distance (km)	7.01	7.02	0.02
Fuel consumption (kg)	2.00	2.20	9.86
Traction motor (kWh)	13.73	13.76	0.2
Regeneration (kWh)	2.77	2.47	-10.71
Battery (kWh)	3.56	3.75	5.41
Generator (kWh)	10.60	9.21	-13.13

The traction energy consumed by motor shows 0.2 % difference compared to the experimental data. It means that the drivetrain model which consists of motor, motor reduction gear, and final reduction gear can simulate real vehicle very precisely. Although the energy recovered by regenerative braking shows 10.71 % difference, the absolute value is negligibly small. Moreover, discharged battery energy shows good agreement with the experiment data. The predicted generated energy from generation system is almost the same as the experimental data. However, fuel consumption calculated from simulation shows difference compared with the experimental result even though engine operating time and conditions are the same. The reason is that the map data which was applied to simulation was measured from dynamometer test while the fuel consumption measured during the experiment was predicted from ECU. Since the two maps were measured in different environment and equipment, fuel consumption rates show errors as shown in Figure 50.

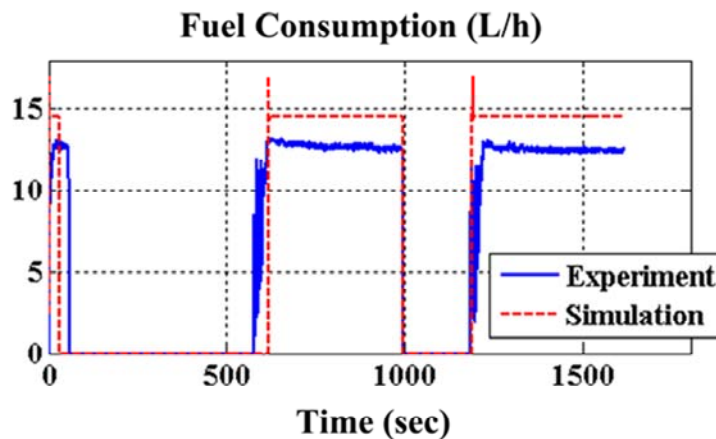


Figure 50. Validation results of fuel consumption in KATECH G mode

## Chapter 4. Optimization

### 4.1 Optimization of system design

#### 4.1.1 Optimization of the working fluid type

There are various organic fluids which are used as working fluid in Rankine cycle. Because each organic fluid has specific physical properties, the cycle efficiency is different according to the working fluids. To calculate the cycle efficiency, representative working fluids such as R245fa, R1234yf, water, toluene and ethanol were adopted. The properties of working fluids at 1 *atm* and 393.15 K are listed in Table 12. As shown in Table 12, organic fluids show lower sound speed and constant pressure heat capacity than water. In contrast, a density of organic fluid is higher than that of water. These different characteristics of properties are very important to design a turbine, because those properties affect the diameter, the operation speed, and the efficiency of the turbine.

The T-S diagrams of working fluids are shown in Figures 51 ~ 55. R245fa, R1234fa, and toluene show the characteristic of the dry fluid. The dry fluid has positive gradient on the saturated vapor line, while the wet fluid such as water and ethanol has the negative gradient of saturated vapor line in T-S diagram. It means that after pressure drop in the turbine, the working fluids stay still superheated vapor state in the case of dry fluid. Thus, the blade erosion can be avoided. In contrast, because the wet working fluid state is saturated vapor after the pressure drop in the turbine, the dryness of working fluid should be taken into account to avoid the turbine blade erosion.

To calculate Rankine cycle efficiency, the state at condenser was determined with consideration of the pressure because the size of condenser should be limited. To achieve low pressure in the condenser, the size of the condenser should be increased. However, because the system is installed in the engine room of the target vehicle, it is assumed that the condenser pressure is greater than 0.1 MPa to ensure installation of that in the vehicles. The process of Rankine cycle was assumed as an isentropic, and the efficiencies of the pump and the turbine were assumed as constant value (0.8).

The process of Rankine cycle is drawn on T-S diagram in Figure 56. From state 1 to state 2, the pump compresses the working fluid up to the target pressure. In the heat exchanger (state 2  $\rightarrow$  state 3), the exhaust gas supplies heat to compressed working fluid, then the working fluid is converted from compressed liquid into superheated vapor. The superheated working fluid is expanded in the turbine (state 3  $\rightarrow$  state 4) with generation of the useful work. Finally, the working fluid is converted into saturated liquid in the condenser (state 4  $\rightarrow$  state 1). Energy flow in each process is defined as below equations.

$$\text{Process } 1 \rightarrow 2 : w_{\text{pump}} = h_2 - h_1 \quad (4.1.1.1)$$

$$\text{Process } 2 \rightarrow 3 : q_{\text{heatexchan ger}} = h_3 - h_2 \quad (4.1.1.2)$$

$$\text{Process } 3 \rightarrow 4 : w_{\text{turbine}} = h_3 - h_4 \quad (4.1.1.3)$$

$$\text{Process } 4 \rightarrow 1 : q_{\text{condenser}} = h_3 - h_4 \quad (4.1.1.4)$$

Because the isentropic process was assumed, the entropy values of state 1 and state 2 are the same. In the same sense, the entropy values of state 3 and state 4 are the same, too. From this assumption, the dryness of the working fluid is determined as Eq. (4.1.1.5).

$$x = \frac{s_3 - s_{4,L}}{s_{4,G} - s_{4,L}} \quad (4.1.1.5)$$

where,  $s$  means the entropy and subscript  $L$  and  $G$  are the liquid state and the gas state, respectively. From above equations, Rankine cycle efficiency is determined as Eq. (4.1.1.6).

$$\eta_R = \frac{[(h_3 - h_4) \times \eta_{turbine} - (h_2 - h_1) / \eta_{pump}] \dot{m}_{work}}{\dot{q}_{exh}} \quad (4.1.1.6)$$

where,  $\dot{q}_{exh}$  and  $\dot{m}_{work}$  are the inlet exhaust gas energy after the catalyst and the mass flow rate of the working fluid.

A point of 1200 rpm – 100 % load where the bsfc has minimum value is selected as the reference engine operation point because the engine is operated at the best bsfc point to achieve high level fuel economy. In the case of the conventional SHEV, the engine is operated at the best bsfc point mainly when the optimal control strategy is applied. Thus, because the WHRS uses surplus energy from the engine, this control rule would be applied to the target system. The temperature of the exhaust gas at that operation point is 750 K. It is enough to superheat the working fluid up to target temperature by controlling mass flow rate of the working fluid. Only the exhaust gas was selected as heat source because the exergy and the available energy are much greater than that of the charged air and the coolant.

To investigate Rankine cycle efficiency according to the working fluids, the working conditions at inlet and outlet of turbine were varied. In this chapter it is assumed that various pressure ratio can be implemented. The optimization of working condition was described in the next chapter. The conditions of the condensers are listed in Table 13. The inlet temperature of the condenser is the same to the temperature of the turbine outlet. The temperature at the turbine outlet was determined with consideration of the superheated vapor temperature and the condenser pressure.

It is assumed that the superheat temperature of the working fluid is 20 K higher than the boiling temperature. The temperature at the turbine outlet was determined based on the temperature of the superheated vapor and the pressure in the condenser. The pressure ratios of the working fluids were varied as 1.5, 2, 3, 4, 5, 10, 15 and 20. However, because the pressure ratio cannot be greater than the value at the critical point, maximum pressure ratio is limited. Rankine cycle efficiency of the each working fluid according to the pressure ratio is described in Figure 57. As the pressure ratio increased, Rankine cycle efficiency is increased. However, the increase rate is reduced as the pressure ratio increased. The higher pressure ratio requires more complex system such as a high number multi-stage turbine. In addition, to endure high pressure, overall parts are strengthened. Thus, it will cause the cost increase. Therefore, it is needed to select reasonable pressure ratio with consideration of relationship between the efficiency and the cost.

As described in Figure 57, R1234yf shows the best efficiency whereas toluene shows the worst efficiency. The refrigerants show higher efficiencies than that of other working fluids. It is because that the inlet temperature of the heat exchanger is different. The heat exchanger inlet temperature of R245fa and R1234yf were 304 K whereas those of toluene, water and ethanol were 383 K,

372 K, and 351 K, respectively. Because the effectiveness of the heat exchanger was fixed as 0.8, the outlet temperature of the exhaust gas at the heat exchanger was decreased as the temperature of the compressed working fluid was decreased. It means that the energy recovered from the exhaust gas is increased as the temperature of the compressed working fluid is decreased. Thus, toluene shows the worst efficiency because the inlet temperature at the heat exchanger has the highest value.

Although R1234yf showed the highest efficiency in low pressure ratio range, it is not proper working fluid because it is impossible to implement high pressure ratio with R1234yf to achieve high efficiency. It means that the output power of the turbine with R1234yf is smaller than that of other working fluid. Thus, R245fa was selected as working fluid among the dry fluids. Ethanol and water showed similar efficiency value at the same pressure ratio. However, ethanol is toxic and can cause lubrication problem. Thus, water was selected as the working fluid among the wet fluids.

Table 12. Properties of various working fluids at 1 atm, 393.15 K

Type	State	Density (kg/m <sup>3</sup> )	C <sub>p</sub> (kJ/kg-K)	Sound speed (m/s)	Therm. Cond. (mW/m-K)	Viscosity (g/cm-s)
R245fa	Superheated	4.15	1.04	159.41	21.28	137.42 x 10 <sup>-6</sup>
R1234yf	Superheated	3.52	1.06	174.24	22.80	163.19 x 10 <sup>-6</sup>
Toluene	Superheated	2.93	1.53	188.17	19.75	90.65 x 10 <sup>-6</sup>
Water	Superheated	0.56	2.02	485.87	26.49	130.09 x 10 <sup>-6</sup>
Ethanol	Superheated	1.43	1.94	276.57	25.71	116.48 x 10 <sup>-6</sup>

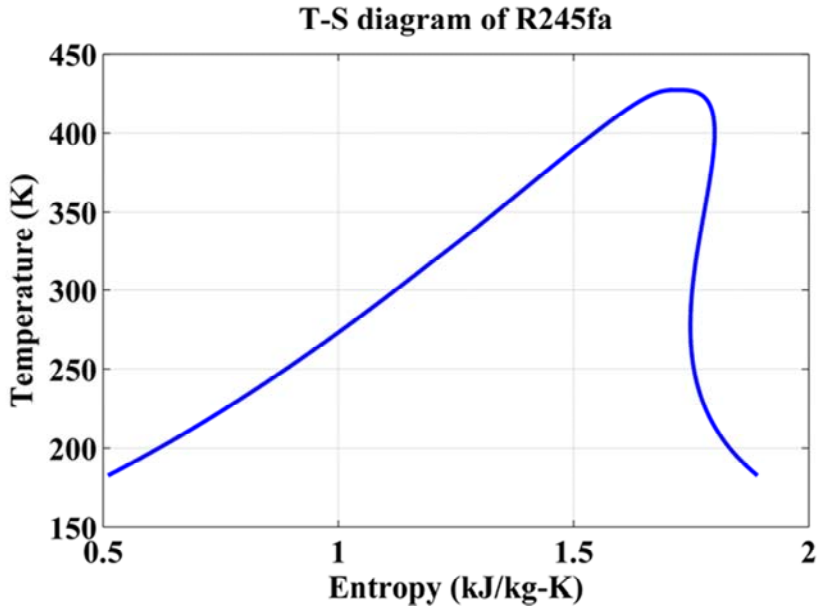


Figure 51. T-S diagram of R245fa

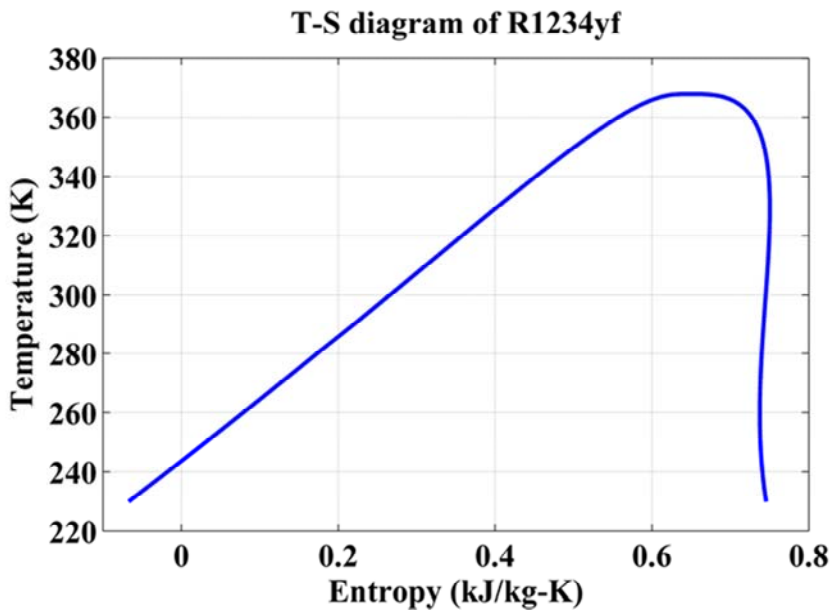


Figure 52 . T-S diagram of R1234yf

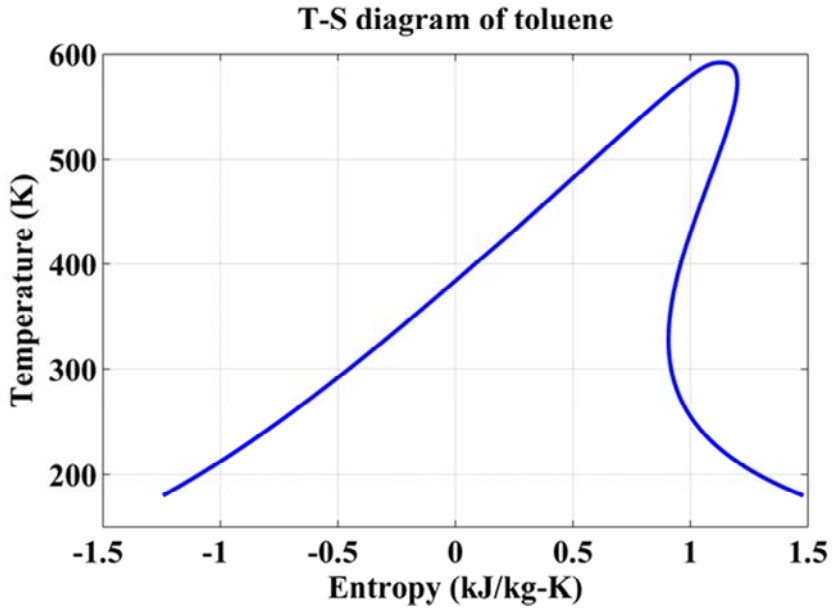


Figure 53. T-S diagram of toluene

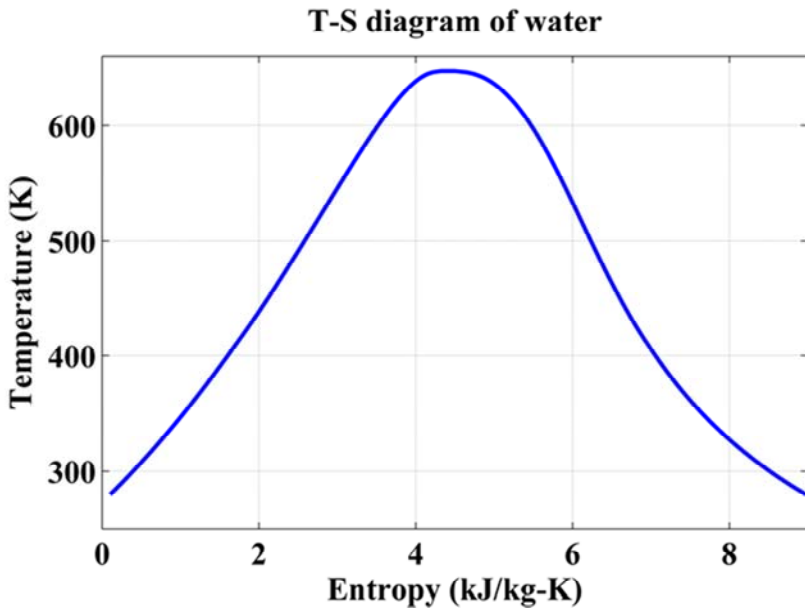


Figure 54. T-S diagram of water

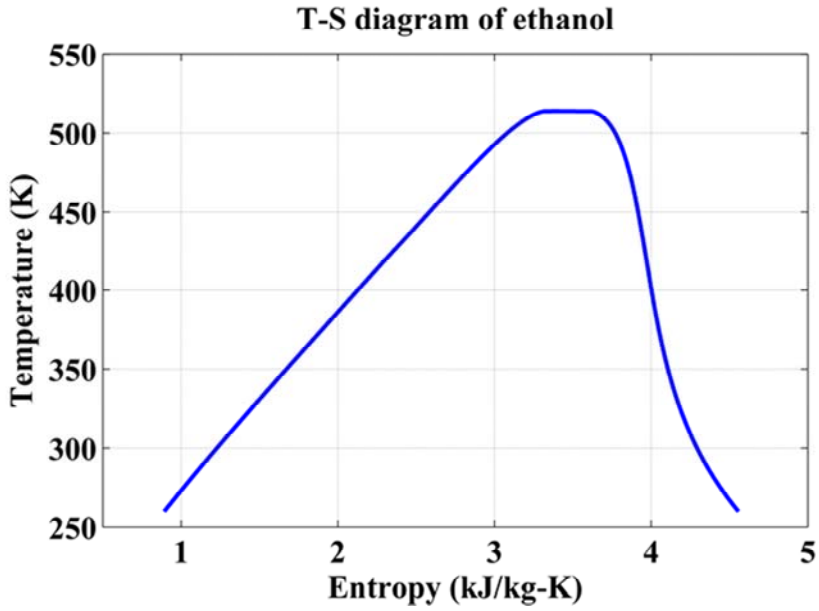


Figure 55. T-S diagram of ethanol

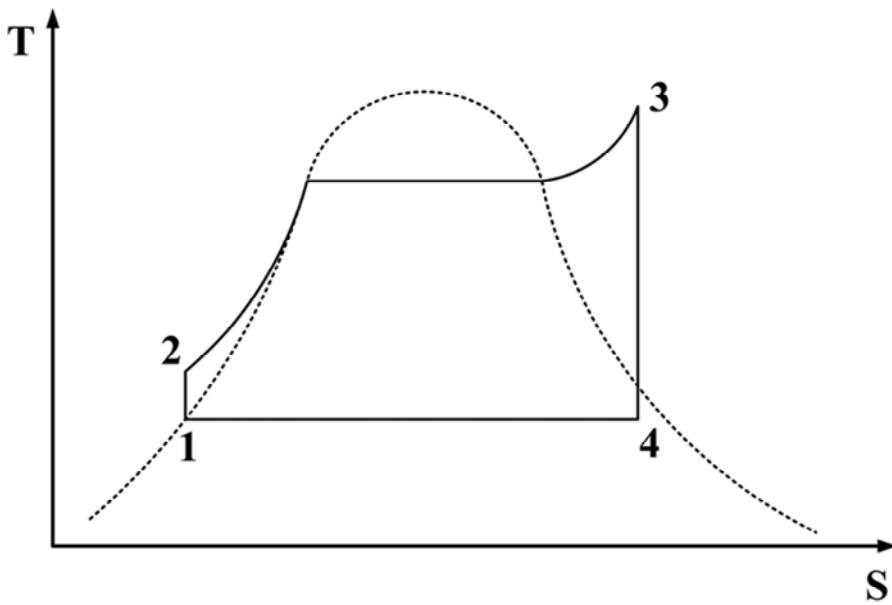


Figure 56. A T-S diagram of superheated Rankine cycle

Table 13. The assumed working condition at the condenser

Working fluid type	Temperature (K) at condenser	Pressure (MPa) at condenser
R245fa	303.2	0.18
R1234yf	303.2	0.78
Toluene	383.3	0.10
Water	373.0	0.10
Ethanol	351.1	0.10

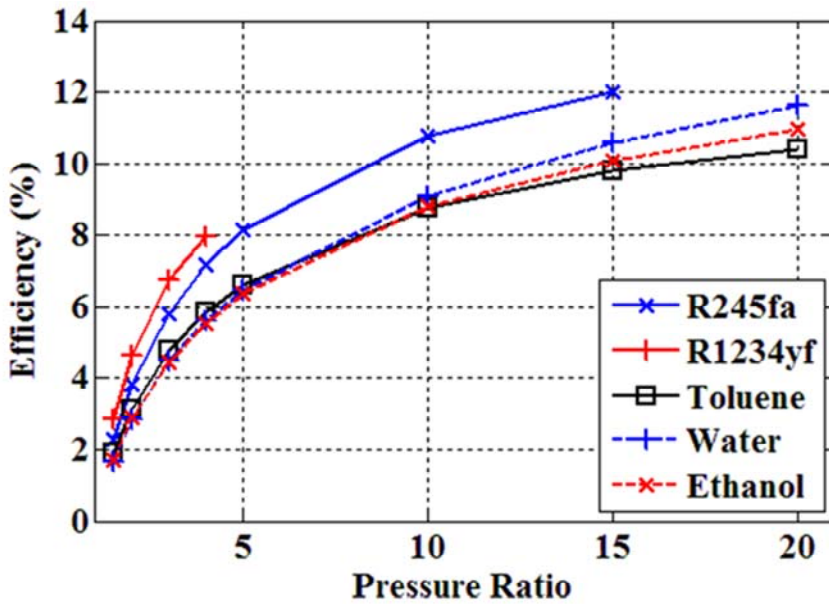


Figure 57. Rankine cycle efficiency according to the working fluids and the pressure ratio

#### **4.1.2 Suggestion of optimizing the working condition**

There are 3 main factors which have effects on efficiency of Rankine cycle. They are the pressure ratio, superheating temperature, and state in the condenser. These factors are varied by type of working fluid because of their physical properties. Thus, in order to achieve high efficiency, it is required to optimize working condition according to working fluids type.

Among above factors, the pressure ratio has great effect on the efficiency of Rankine cycle. As shown in Figure 57, high efficiency can be achieved by increasing the pressure ratio. However, high pressure ratio can cause problem such as choking phenomena in the turbine. Thus, it should be limited to avoid choking. In the turbine design process, pressure ratio is determined as possible as high to improve the efficiency within the limit. Moreover, multi-stage turbine can be designed and implemented to increase pressure ratio without choking phenomena.

The state in the condenser is important because it affects the size of that and recoverable energy level in the heat exchanger. The size of the condenser is limited because it is installed to the vehicle. Thus, in this study, minimum pressured in the condenser was determined as 0.1 MPa. In the case of organic fluid, saturated pressure is higher than 0.1 MPa when saturated temperature is 303.2 K. Because atmosphere temperature is assumed as 303.2 K, minimum fluid temperature in the condenser has the same value compared to atmospheric condition. In contrast, conventional working fluid has lower saturated pressure than 0.1 MPa when the saturated temperature is 303.2 K. Therefore, the saturated pressure was fixed as 0.1 MPa with higher saturated temperature than 303.2 K. As a result, condenser state should be determined with consideration of minimum fluid temperature and saturated pressure because of above reasons.

Superheating temperature has different effect on Rankine cycle efficiency according to working fluid. Thus, it should be taken into account to achieve high efficiency. The efficiencies according to superheating temperature are shown in Figures 58 and 59. In the case of water, the efficiency is slightly improved as superheating temperature increased at both low and high pressure ratios. However, in the case of R245fa, the efficiency is decreased as the superheating temperature increases at low pressure ratio whereas the efficiency is increased at high pressure ratio with the same condition. Thus, when wet fluid is used as working fluid, the temperature should be set as high as possible regardless of the pressure ratio. The target superheating temperature of dry fluid should be determined based on the pressure ratio because improvement in efficiency by superheating temperature shows opposite trends according to pressure ratio.

Consequently, the working condition of water and R245fa to maximize the efficiency of the system can be summarized as bellows.

- The pressure ratio has to be maximized for achieving high efficiency. However, the maximum pressure ratio should be limited to avoid choking phenomena. Thus, in turbine design process, the pressure ratio should consider above guide line.
- The state of condenser is determined with consideration of saturated pressure and temperature. Saturated pressure is limited by size of the condenser and saturated temperature is limited by atmospheric condition. Especially, temperature affects recoverable energy level in the heat exchanger.
- To maximize the system efficiency, the superheating temperature should be determined based on the working fluid properties. In the case of wet fluid such as water, superheating temperature should be high to

enhance efficiency. In contrast, in the case of dry fluid, superheating temperature is determined considering pressure ratio because efficiency show different improvement trend according to the pressure ratio.

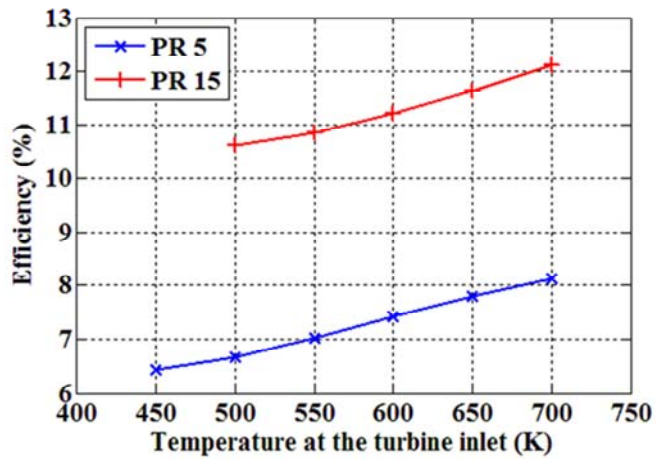


Figure 58. Rankine efficiency of water according to the temperature at the turbine inlet

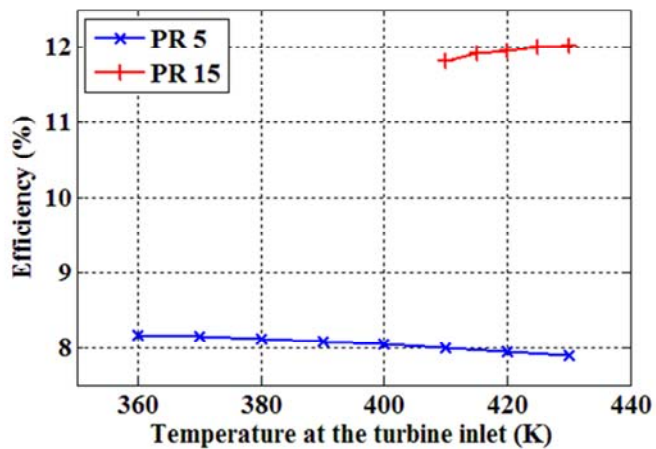


Figure 59. Rankine efficiency of R245fa according to the temperature at the turbine inlet

## 4.1.3 Optimization of the geometric specification

### 4.1.3.1 Turbine

The turbine operation is limited when the choking phenomena occurs. Thus, it is important to design the turbine to avoid choking phenomena. In this study, the radial type was adopted and designed to avoid choking and to achieve high efficiency. As described in previous chapter, high pressure ratio causes choking phenomena. Moreover, it is affected by properties of working fluids. Therefore, the pressure ratio which is determined to avoid choking in design process is maximum limit in real operation.

To optimize design of the turbine, a concept of specific speed should be taken into account [63, 65]. Specific speed is a non-dimensional number which is used to describe the geometry of turbo machine. Although two turbines have different size, the geometries show similar shapes with the same specific speed. The change of geometry according to specific speed is shown in Figure 60.

Specific speed is defined as below equation.

$$N_s = \frac{\omega \sqrt{Q_{out}}}{(\Delta h_0)^{\frac{3}{4}}} \quad (4.1.3.1)$$

where,  $N_s$ ,  $\omega$ ,  $Q_{out}$ , and  $\Delta h_0$  are the specific speed, the turbine rotational speed (rad/s), the volumetric flow rate, and the enthalpy difference between upstream and downstream, respectively. Rohlick [63] had suggested relationship between the efficiency of turbine, inlet angle, and specific speed as shown in Figure 60. Total-to-total efficiency is used when the output kinetic energy of the working fluid is used in next stage turbine. Thus, in the multi-stages turbine, the

efficiencies of turbines excepting final stage turbine have value of total-to-total efficiency. In contrast, total-to-static efficiency is used when the output kinetic energy of the working fluid cannot be used, but wasted to the circumstance. Thus, the final stage turbine uses total-to-static efficiency because the output working fluid does not work, but goes into condenser. Conventional optimum value of specific speed for open loop system such as air turbine is 0.6, whereas 0.8 is optimum value for close loop system. However, high specific speed means high rotational speed of the system. Thus, high speed turbine including high speed generator can cause increase of cost. Thus, the relationship between the increase of cost and efficiency should be considered, carefully.

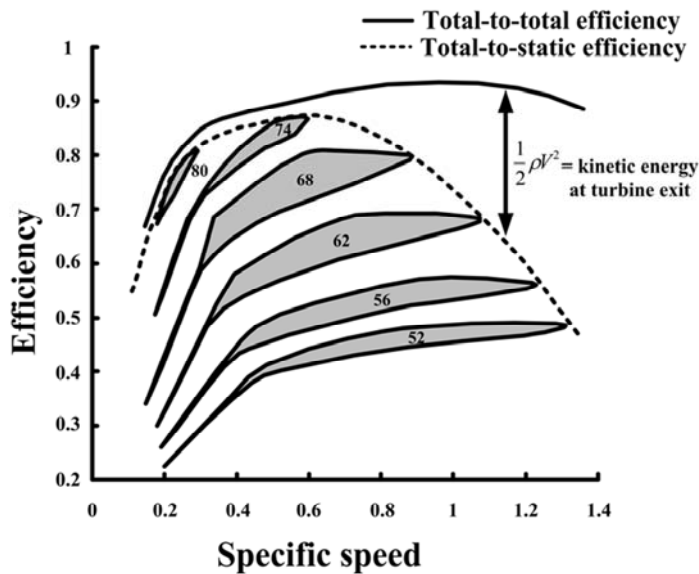


Figure 60. Specific speed vs. Efficiency (Rohlick, 1975)

From specific speed, the diameter of turbine can be determined. Specific speed, inlet angle, mass flow rate are fixed value. Thus, the diameter of turbine is calculated as Eq. (4.1.3.2)

$$D_t = \frac{2u_{in}\sqrt{Q_{out}}}{N_s(\Delta h_0)^{\frac{3}{4}}} \quad (4.1.3.2)$$

where,  $u_{in}$  is the tangential speed of turbine. As described in previous chapter, tangential speed and change of enthalpy are calculated from Eqs. (4.1.3.3) and (4.1.3.4).

$$\Delta h_0 = (C_1 \sin \alpha)^2 \quad (4.1.3.3)$$

$$u_{in} = C_1 \sin \alpha \quad (4.1.3.4)$$

where,  $C_1$  is the absolute inlet speed of working fluid, which is lower than the speed of sound. From above equations, the diameter of turbine can be determined as Eq. (4.1.3.5).

$$D_t = \frac{2\sqrt{Q_{out}}}{N_s(C_1 \sin \alpha)^{\frac{1}{2}}} \quad (4.1.3.5)$$

By using it, the turbine diameter and the inlet angle can be determined. The condenser state which was determined in the chapter 4.1.1, was adopted as the outlet state of the final turbine.

#### 4.1.3.1.1 Design of the single-stage turbine

First of all, the design of a single stage turbine was conducted. In Table 13, the turbine outlet condition was defined. The flow rate of working fluid was calculated based on the thermodynamic analysis which was described in previous chapter. The design points of the inlet angle and the specific speed were varied to investigate the maximum work of the turbine. A total-to-static efficiency was applied because the single stage turbine was adopted. The cases for the optimal design of the turbine are listed in Table 14.

Table 14. Optimization cases of the turbine geometry (diameter)

Turbine inlet angle		68, 74, 80
Pressure (MPa)	R245fa	0.2 ~ 3.5
	Water	0.2 ~ 10
Ns	68	0.16 ~ 0.88
	74	0.18 ~ 0.60
	80	0.18 ~ 0.30

When the outlet temperature of the turbine is 318.1 K, the efficiency, the inlet temperature, the maximum pressure ratio, the work and the speed of the turbine according to the inlet angle and specific speed are shown in Figures 61 ~ 66.

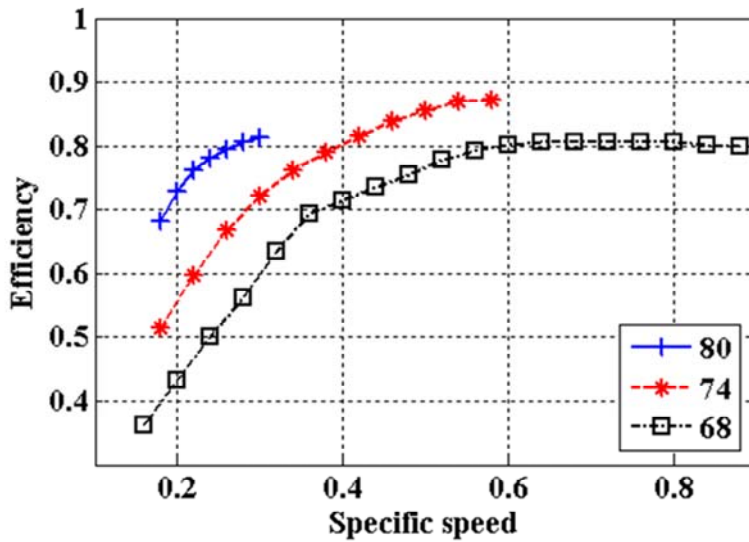


Figure 61. An efficiency of the turbine according to the inlet angle and a specific speed (R245fa, outlet temperature 318.1 K)

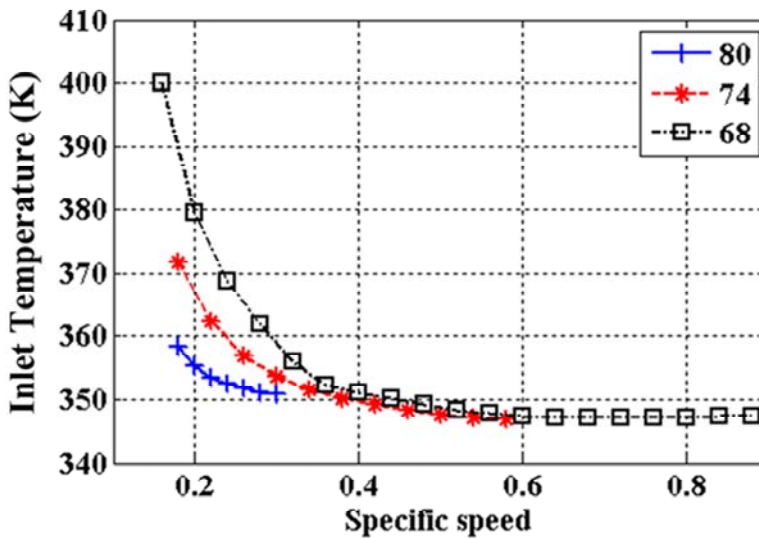


Figure 62. An inlet temperature of the turbine according to the inlet angle and a specific speed (R245fa, outlet temperature 318.1 K)

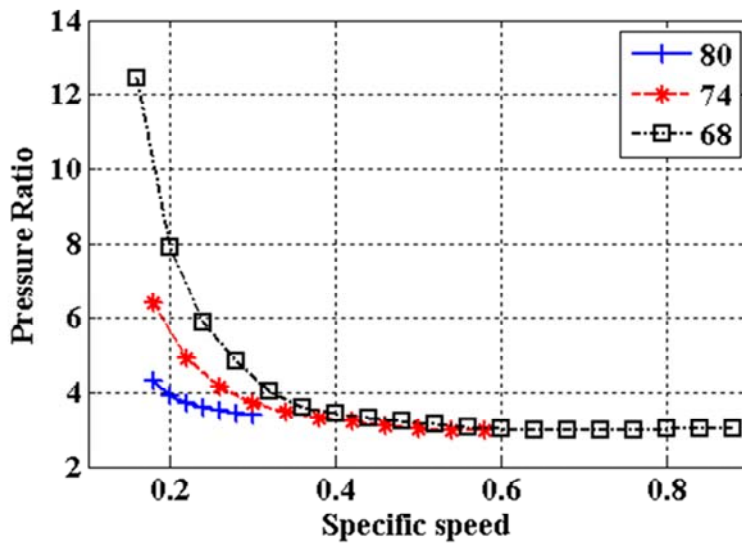


Figure 63. A maximum pressure ratio of the turbine according to the inlet angle and a specific speed (R245fa, outlet temperature 318.1 K)

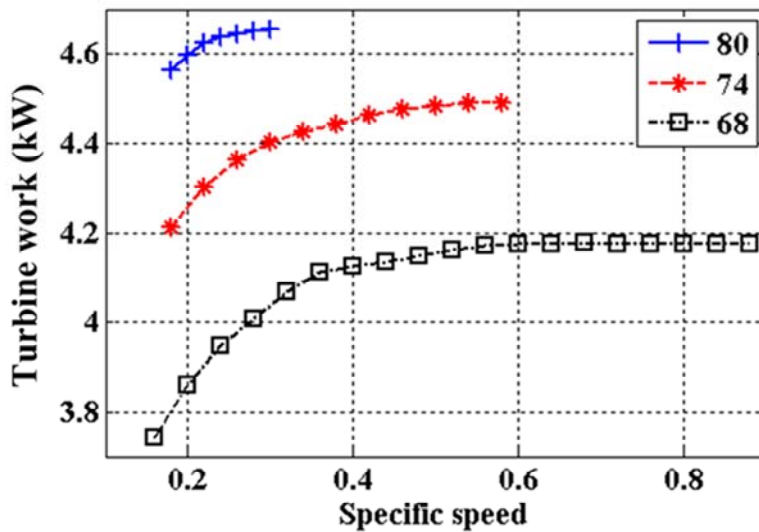


Figure 64. A work of the turbine according to the inlet angle and a specific speed (R245fa, outlet temperature 318.1 K)

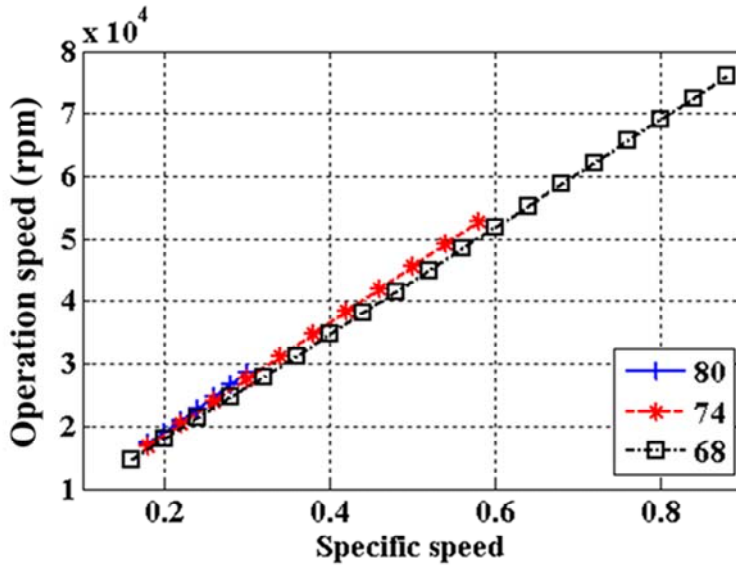


Figure 65. A speed of the turbine according to the inlet angle and a specific speed (R245fa, outlet temperature 318.1 K)

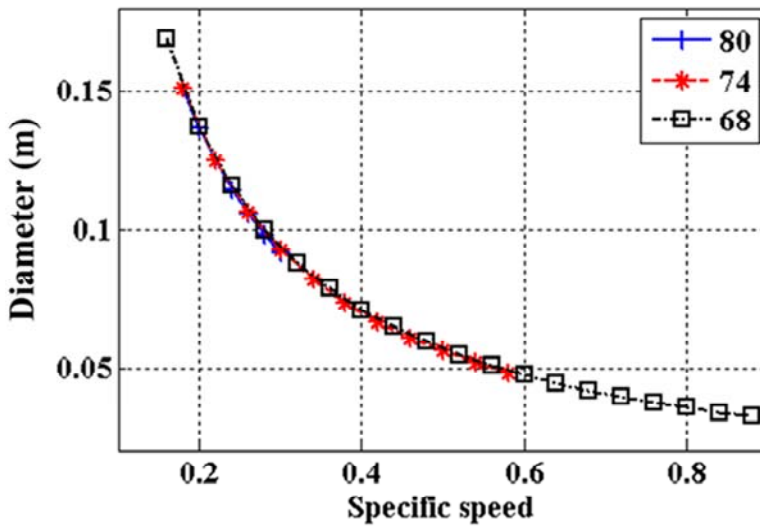


Figure 66. A diameter of the turbine according to the inlet angle and a specific speed (R245fa, outlet temperature 318.1 K)

In previous chapter, the efficiency is increased as the pressure ratio increased. Therefore, the design results are seemed to be wrong because the relationship between the pressure ratio and the efficiency shows opposite trends. However, in design process, the efficiency was determined before determining the pressure ratio. The efficiency was determined by the target specific speed. Then, the difference on enthalpy of the working fluid at the inlet and outlet was multiplied by the efficiency. After that, the pressure at the turbine inlet was determined to avoid choking. In other words, if the efficiency is low, net enthalpy which is converted into kinetic energy of the working fluid is decreased with the same inlet enthalpy. Thus, in low efficiency region, a pressure ratio is increased because inlet enthalpy should be large enough to increase the speed of working fluids up to sound of speed. When the outlet temperature of the turbine is 352.4 K, the results of the design are shown in Figures 67 ~ 69.

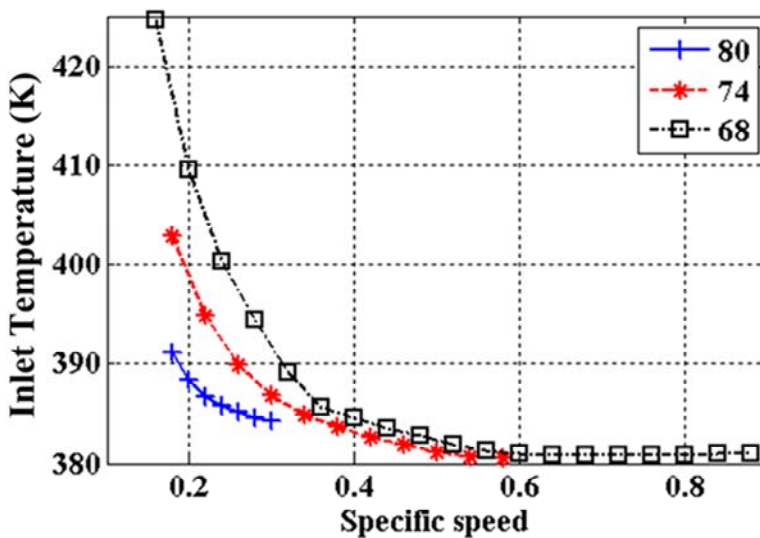


Figure 67. An inlet temperature of the turbine according to the inlet angle and a specific speed (R245fa, outlet temperature 352.4 K)

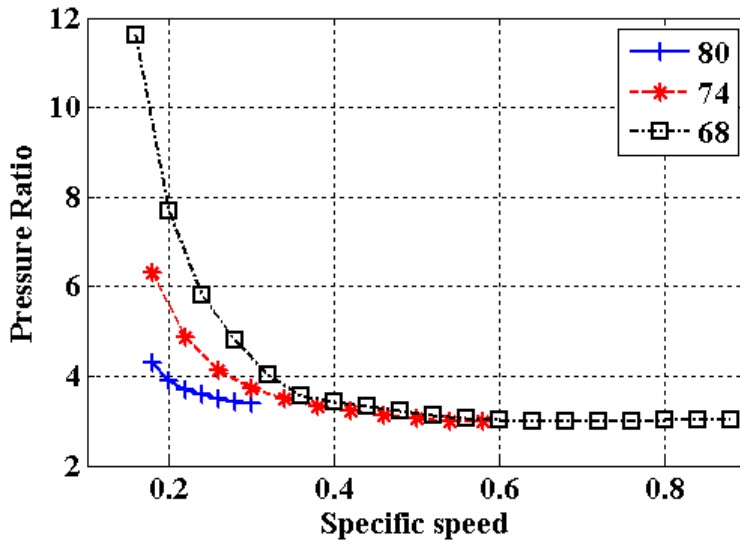


Figure 68. A maximum pressure ratio of the turbine according to the inlet angle and a specific speed (R245fa, outlet temperature 352.4 K)

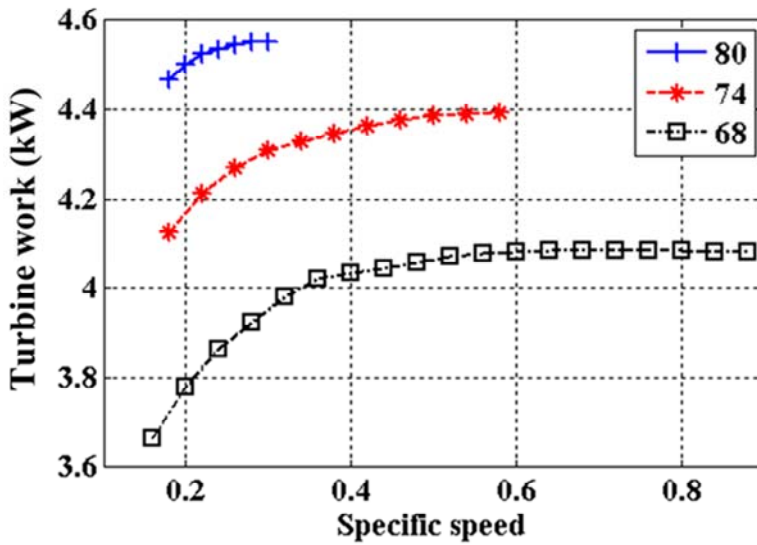


Figure 69. A work of the turbine according to the inlet angle and a specific speed (R245fa, outlet temperature 352.4 K)

The work generated by the turbine at low outlet temperature condition was greater than at high outlet temperature condition. Thus, from these results, the optimal design and working condition can be determined as Table 15 when the single turbine was applied.

Table 15. Optimal design of the single turbine (R245fa)

Turbine diameter (m)	0.092
Turbine target speed (rpm)	28482
Turbine inlet angle (°)	80
Pressure ratio (-)	3.4
Turbine inlet temperature (K)	351

By using the same process, the turbine was designed optimally when water was used as the working fluid. It was conducted with two turbine outlet conditions. In the first case, the dryness and the temperature at the outlet of the turbine were determined as 85 % and as 372.8 K, respectively. In the second case, they were determined as 100 % and 372.8 K, respectively. The results of the first case and the second case are described in Figures 70 ~ 74 and Figures 75 ~ 77, respectively.

Rankine system produced smaller work with water than with R245fa. Moreover, the operation speed with water was much higher than that with R245fa because water density is small which causes increase in volume flow rate. As described in previous chapter, water shows characteristic which the turbine work is increased as superheating temperature increased at the same specific speed. The turbine operation speed should be limited to prevent increase of cost. Thus, the maximum operation speed was determined as 200,000 rpm. Moreover, for manufacturing, it is suggested that the diameter of the turbine

should be larger than 0.4 m. The optimal design of the single stage turbine which satisfies constraints is determined as Table 16.

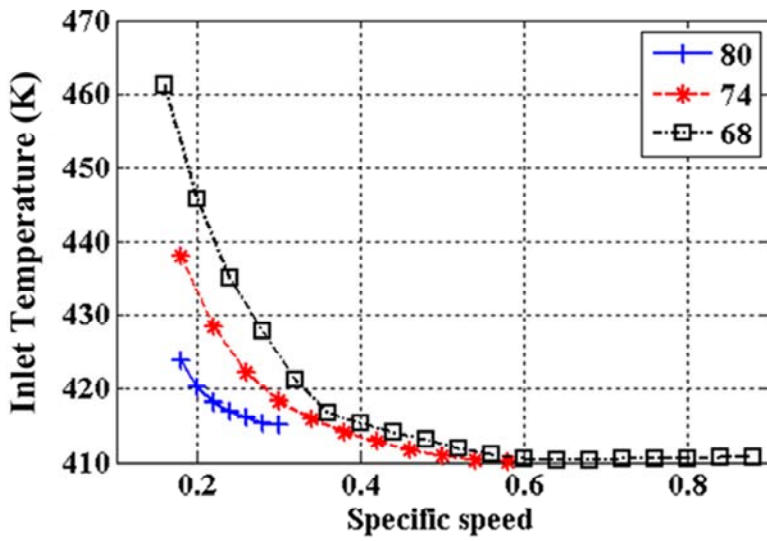


Figure 70. An inlet temperature of the turbine according to the inlet angle and a specific speed (water, outlet dryness 85 %)

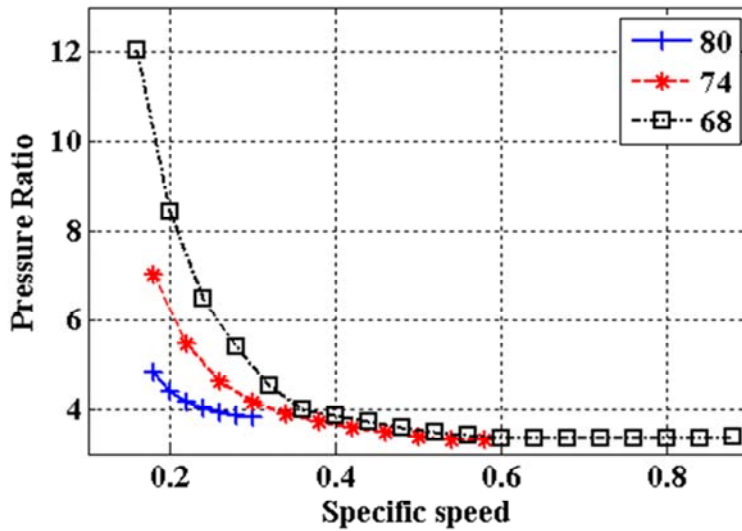


Figure 71. A maximum pressure ratio of the turbine according to the inlet angle and a specific speed (water, outlet dryness 85 %)

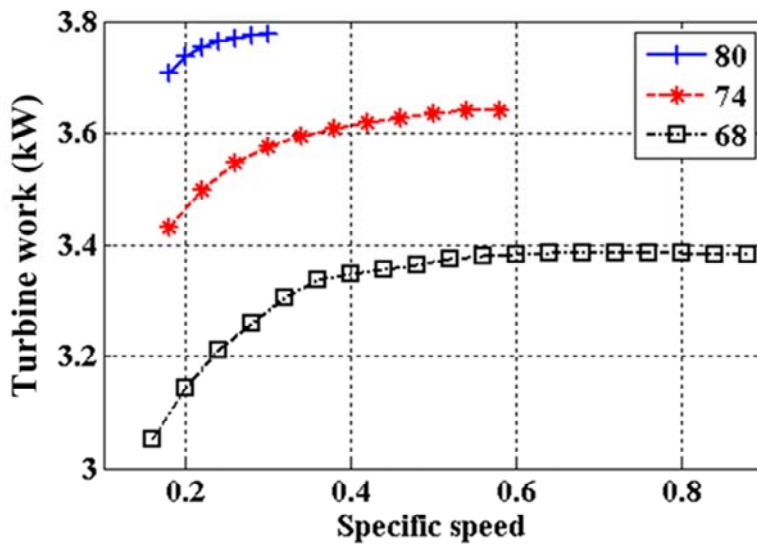


Figure 72. A work of the turbine according to the inlet angle and a specific speed (water, outlet dryness 85 %)

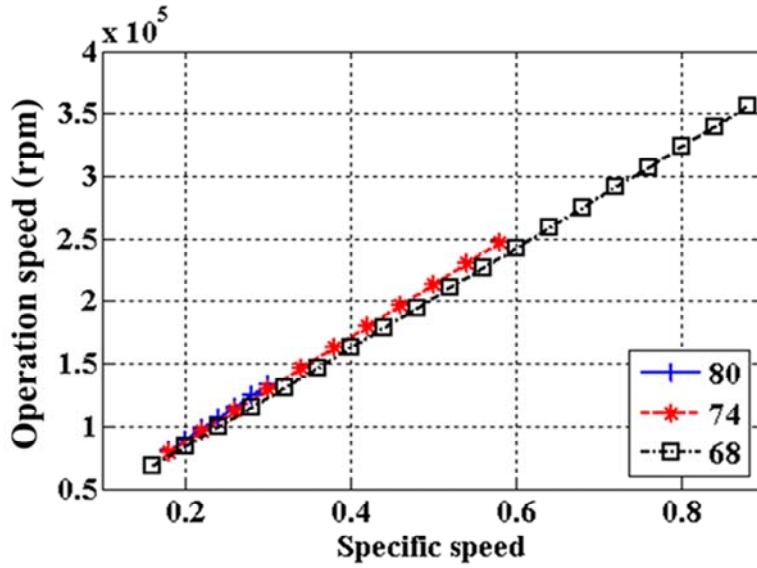


Figure 73. A speed of the turbine according to the inlet angle and a specific speed (water, outlet dryness 85 %)

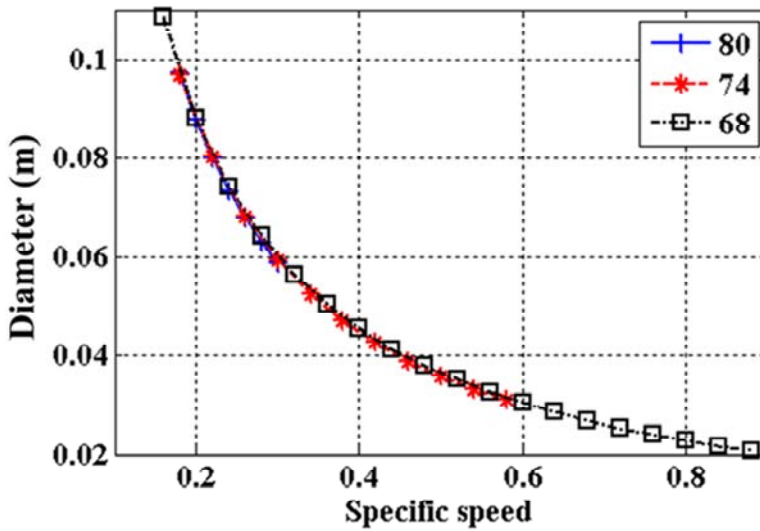


Figure 74. A diameter of the turbine according to the inlet angle and a specific speed (water, outlet dryness 85 %)

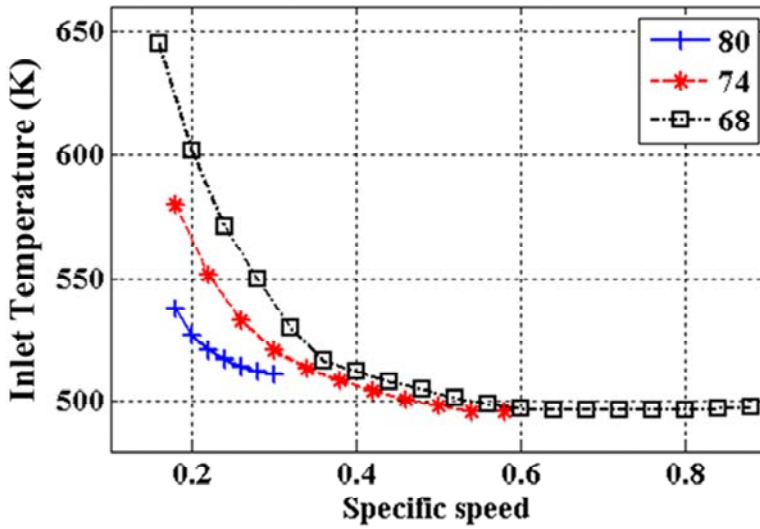


Figure 75. An inlet temperature of the turbine according to the inlet angle and a specific speed (water, outlet dryness 100 %)

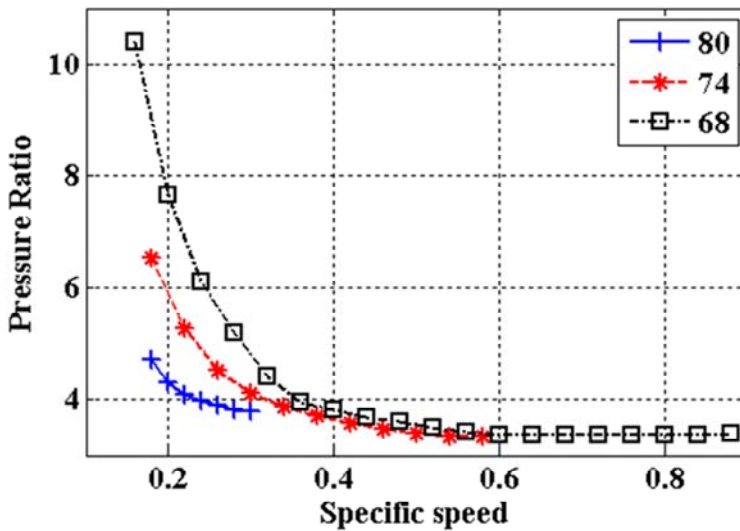


Figure 76. A maximum pressure ratio of the turbine according to the inlet angle and a specific speed (water, outlet dryness 100 %)

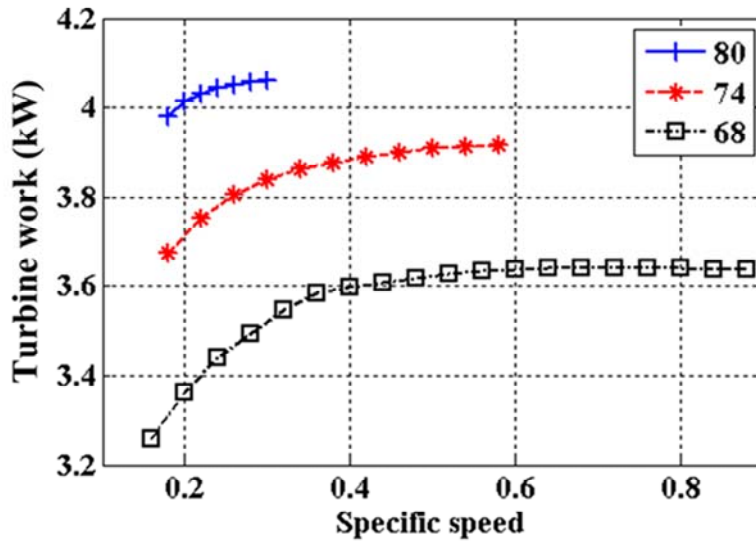


Figure 77. A work of the turbine according to the inlet angle and a specific speed (water, outlet dryness 100 %)

Table 16. Optimal design of the single turbine (water)

Turbine diameter (m)	0.0636
Turbine target speed (rpm)	139,607
Turbine inlet angle (°)	80
Pressure ratio (-)	3.9
Turbine inlet temperature (K)	514

#### **4.1.3.1.2 Design of the multi-stage turbine**

However, it is difficult to produce more work with the single-stage turbine because pressure ratio is limited. In addition, to improve cycle efficiency of Rankine cycle, pressure ratio should be increased. Thus, multi-stage turbine to achieve high pressure ratio was adopted. The design process is similar to that of the single stage turbine. Design was conducted from last stage to first stage. However, because many stages can cause the increase of the cost, the maximum number of stage was limited as 3. The design was conducted with the same condenser conditions which were used in the design process of the single stage turbine.

In the case of R245fa, 3-stage turbine was designed and applied to the system. Each stage turbine speed should be the same because they are connected through one shaft. It means that each stage turbine cannot be optimized separately because of the operating speed. Thus, to optimize turbine with satisfaction of the same speed condition, a combination which can generate maximum work was selected. The maximum speed of turbine was assumed as near 50,000 rpm. Tables 17 and 18 show the results of the multi stage turbine when the turbine output temperatures are 318.1 K and 352.4 K, respectively.

Table 17. The results of the multi-stage turbine design (R245fa, outlet temperature 318.1 K)

Angle			Speed	Work				Pressure			Temp.	Diameter		
°			rpm	kW				MPa			K	m		
3rd	2nd	1st	total	1st	2nd	3rd	Total	1st	2nd	3rd	1st	1st	2nd	3rd
80	80	74	29707	1.52	2.92	4.00	8.43	3.64	1.56	0.59	430	0.053	0.074	0.087
		68	29649	1.30	2.92	4.00	8.21	3.64	1.56	0.59	430	0.050	0.074	0.087
	74	74	29646	1.32	2.63	4.00	7.95	3.64	1.75	0.59	430	0.050	0.071	0.087
		68	29648	1.13	2.63	4.00	7.76	3.64	1.75	0.59	430	0.046	0.071	0.087
	68	74	29648	1.21	2.34	4.00	7.55	3.64	1.87	0.59	430	0.048	0.067	0.087
		68	29650	1.04	2.34	4.00	7.38	3.64	1.87	0.59	430	0.044	0.067	0.087
74	80	74	42042	1.79	3.13	3.88	8.79	3.02	1.42	0.55	418	0.041	0.054	0.060
		68	42038	1.61	3.13	3.88	8.62	3.17	1.42	0.55	421	0.039	0.054	0.060
	74	80	42036	1.92	2.90	3.88	8.69	2.93	1.45	0.55	416	0.042	0.052	0.060
		74	42037	1.75	2.90	3.88	8.53	3.07	1.45	0.55	419	0.041	0.052	0.060
		68	42042	1.58	2.90	3.88	8.36	3.22	1.45	0.55	422	0.038	0.052	0.060
	68	80	42029	1.88	2.68	3.88	8.44	2.97	1.49	0.55	417	0.042	0.050	0.060
		74	42073	1.72	2.67	3.87	8.26	3.12	1.49	0.55	420	0.040	0.050	0.060
		68	42144	1.56	2.66	3.86	8.08	3.32	1.49	0.55	424	0.038	0.050	0.060
	68	80	80	42613	1.93	3.10	3.62	8.65	2.93	1.45	0.57	416	0.042	0.053

		74	42663	1.76	3.09	3.62	8.47	3.07	1.45	0.57	419	0.040	0.053	0.057
		68	42720	1.59	3.08	3.61	8.27	3.22	1.45	0.57	422	0.038	0.053	0.057
	74	80	42629	1.89	2.87	3.62	8.38	2.97	1.49	0.57	417	0.041	0.051	0.057
		74	42680	1.73	2.86	3.61	8.20	3.12	1.49	0.57	420	0.040	0.051	0.057
		68	42739	1.56	2.85	3.60	8.01	3.27	1.49	0.57	423	0.038	0.051	0.057
	68	80	42628	1.85	2.66	3.62	8.13	3.02	1.52	0.57	418	0.041	0.049	0.057
		74	42636	1.70	2.66	3.62	7.98	3.17	1.52	0.57	421	0.039	0.049	0.057
		68	42765	1.54	2.64	3.60	7.78	3.37	1.52	0.57	425	0.037	0.049	0.057

Table 18. The results of the multi-stage turbine design (R245fa, outlet temperature 352.4 K)

Angle		speed	Work				Pressure			Temp.	Diameter			
°		rpm	kW				MPa			K	m			
3rd	2nd	1st	total	1st	2nd	3rd	Total	1st	2nd	3rd	1st	1st	2nd	3rd
80	80	80	33505	1.27	3.29	4.00	8.56	2.95	1.88	0.60	440	0.047	0.075	0.083
		74	33506	1.07	3.29	4.00	8.36	2.95	1.88	0.60	440	0.043	0.075	0.083
		68	33505	0.92	3.29	4.00	8.21	2.95	1.88	0.60	440	0.040	0.075	0.083
	74	80	33505	0.87	2.97	4.00	7.84	2.95	2.19	0.60	440	0.039	0.072	0.083
		74	33506	0.78	2.97	4.00	7.74	2.95	2.19	0.60	440	0.037	0.072	0.083
		68	33503	0.68	2.97	4.00	7.65	2.95	2.19	0.60	440	0.034	0.072	0.083
	68	74	33503	0.51	2.67	4.00	7.18	2.95	2.47	0.60	440	0.030	0.068	0.083
		68	33503	0.46	2.67	4.00	7.13	2.95	2.47	0.60	440	0.028	0.068	0.083
	74	80	80	50300	2.01	3.41	3.77	9.20	2.95	1.51	0.54	440	0.039	0.051
74			50303	1.78	3.41	3.77	8.97	2.95	1.51	0.54	440	0.037	0.051	0.054
68			50302	1.57	3.41	3.77	8.75	2.95	1.51	0.54	440	0.035	0.051	0.054
74		80	50300	1.85	3.23	3.77	8.85	2.95	1.60	0.54	440	0.038	0.050	0.054
		74	50302	1.65	3.23	3.77	8.65	2.95	1.60	0.54	440	0.035	0.050	0.054
		68	50301	1.46	3.23	3.77	8.46	2.95	1.60	0.54	440	0.033	0.050	0.054
68		80	50303	1.35	3.00	3.77	8.12	2.95	1.69	0.54	440	0.032	0.048	0.054

		74	50302	1.51	3.00	3.77	8.29	2.95	1.69	0.54	440	0.034	0.048	0.054
		68	50303	1.35	3.00	3.77	8.12	2.95	1.69	0.54	440	0.032	0.048	0.054
68	80	80	51147	1.93	3.39	3.55	8.87	2.95	1.55	0.56	440	0.038	0.050	0.051
		74	51146	1.72	3.39	3.55	8.66	2.95	1.55	0.56	440	0.036	0.050	0.051
		68	51149	1.52	3.39	3.55	8.46	2.95	1.55	0.56	440	0.034	0.050	0.051
	74	80	51146	1.77	3.21	3.55	8.53	2.95	1.64	0.56	440	0.036	0.049	0.051
		74	51149	1.59	3.21	3.55	8.35	2.95	1.64	0.56	440	0.034	0.049	0.051
		68	51143	1.42	3.21	3.55	8.18	2.95	1.64	0.56	440	0.032	0.049	0.051
	68	80	51144	1.61	2.98	3.55	8.14	2.95	1.73	0.56	440	0.034	0.047	0.051
		74	51147	1.45	2.98	3.55	7.99	2.95	1.73	0.56	440	0.033	0.047	0.051
		68	51150	1.32	2.98	3.55	7.85	2.95	1.73	0.56	440	0.031	0.047	0.051

Based on the results, the multi stage turbine for R245fa generates maximum power with 80°, 80°, 74° of first, second, third turbine inlet angle at 50,300 rpm. Thus, the optimal case of multi stage turbine for R245fa was determined as below table.

Table 19. Optimal combination of multi stage turbine for R245fa

Turbine diameter (m)	0.039, 0.051, 0.054
Turbine target speed (rpm)	50,300
Turbine inlet angle (°)	80, 80, 74
Pressure ratio (-)	1.95, 2.80, 3.04
Turbine inlet temperature (K)	440

In the case of water, 2-stage turbine was designed. Because the mass flow rate of water is very small, the turbine speed is much greater than that of R245fa. Thus, it is impossible to match each turbine speed the same with 3-stage turbine. To optimize turbine with satisfaction of the same speed condition, a combination which can generate maximum work was selected. The maximum speed of turbine was assumed as near 250,000 rpm. Tables 20 and 21 show the results of the multi stage turbines, when the turbine output dryness values are 85 % and 100 %, respectively.

Table 20. The results of the multi-stage turbine design (Water, outlet dryness 85 %)

Angle		Speed	Work			Pressure		Temp.	Diameter	
°		rpm	kW			MPa		K	m	
2nd	1st	total	1st	2nd	total	1st	2nd	1st	1st	2nd
74	68	245162	5.08	2.60	7.68	11.20	0.33	750	0.043	0.031
	68	298617	5.59	2.66	8.24	11.20	0.33	750	0.037	0.026
	68	191817	4.36	2.61	6.97	11.20	0.36	750	0.051	0.040
68	68	234674	4.86	2.46	7.32	11.20	0.35	750	0.044	0.031
	68	280453	5.42	2.44	7.86	11.20	0.33	750	0.039	0.026
	68	378442	4.57	2.86	7.43	2.05	0.33	507	0.024	0.019

Table 21. The results of the multi-stage turbine design (Water, outlet dryness 100 %)

Angle		Speed	Work			Pressure		Temp.	Diameter	
°		rpm	kW			MPa		K	m	
2nd	1st	mean	1st	2nd	total	1st	2nd	1st	1st	2nd
80	68	180161	3.60	2.66	6.26	2.03	0.29	750	0.051	0.044
74	68	347913	5.26	2.54	7.80	2.03	0.26	750	0.032	0.022
	68	290165	4.74	2.54	7.29	2.03	0.27	750	0.036	0.026
	68	203354	3.81	2.55	6.35	2.03	0.30	750	0.046	0.038
	68	174060	3.43	2.54	5.97	2.03	0.31	750	0.051	0.044
	68	121913	2.55	2.55	5.10	2.03	0.40	750	0.063	0.063
68	68	478977	5.82	2.38	8.21	1.80	0.27	730	0.024	0.015
	68	273642	4.57	2.35	6.92	2.03	0.28	750	0.038	0.027
	68	120913	2.31	2.37	4.68	2.03	0.48	750	0.060	0.061

The multi stage turbine for water generates maximum power with 68 °, 68 ° of first and second turbine inlet angle at 478,977 rpm. However, the speed of turbine is too high to use general generator. Thus, as described above, the optimal combination of the multi stage turbine for water was selected with the consideration of the maximum speed as near 200,000 rpm. In addition, to protect erosion of the turbine blade, the dryness at turbine outlet was determined as 100 %. The optimal combination is listed in Table 22.

Table 22. Optimal combination of multi stage turbine for water

Turbine diameter (m)	0.051, 0.044
Turbine target speed (rpm)	180,161
Turbine inlet angle (°)	68, 80
Pressure ratio (-)	7, 2.9
Turbine inlet temperature (K)	750

#### 4.1.3.2 Heat exchanger

An optimizing a geometric specification of the heat exchanger was conducted about type and size. To optimize the type of the heat exchanger, various geometric characteristic of plate fin type were applied to the quasi-1D model. To optimize the size, various combinations were applied. The length of the heat exchanger was limited shorter than 0.1 m because there is limitation to install the heat exchanger in the engine room. It was assumed that the width and the height have the same value, and they were limited under 0.3 m as the same reason of length. The flow direction of each working fluid was determined as counter flow because this type flow direction can recover the waste heat effectively. 4 types of plate fin geometry were considered and listed in Table 23. A friction factor and Stanton number according to Reynolds number of each heat exchanger are shown in Figures 78 ~ 81.

Table 23. The characteristics of various plat fin type heat exchanger

Surface designation	Plate spacing	Fins/in	Hydraulic diameter, $4r_h$	Fin thickness	Flow length of uninterrupted fin	Heat transfer area / volume between plate	Fin area/ total area
	$10^{-3}$ m		$10^{-3}$ m	$10^{-3}$ m	$10^{-3}$ m	$m^2 / m^3$	
5.3	11.94	5.3	6.15	0.152	63.2	616.8	0.719
14.77	8.38	14.77	2.59	0.152	63.8	1378.0	0.844
10.27T	13.82	10.27	3.84	0.254	127.0	951.1	0.863
30.33T	8.76	30.33	1.222	0.152	63.5	2665.7	0.928

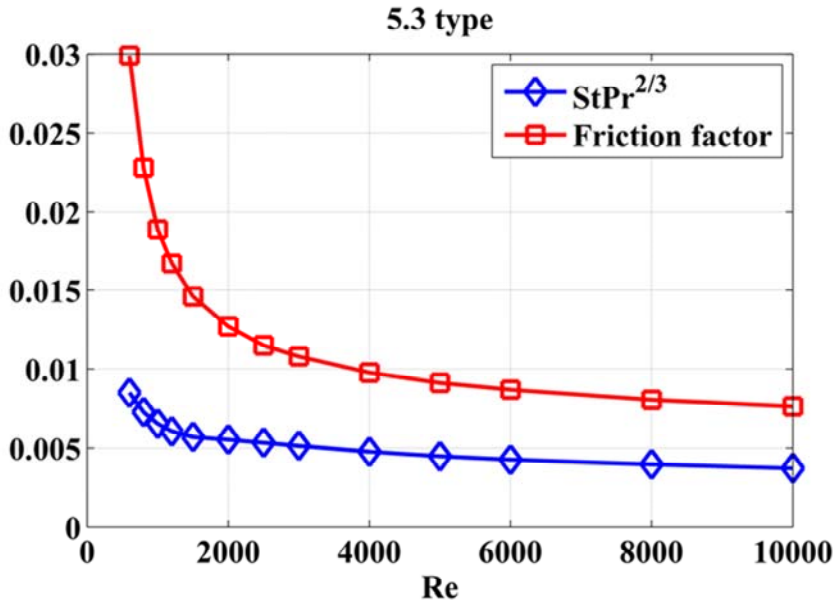


Figure 78. StPr<sup>2/3</sup> and friction factor of 5.3 type Heat exchanger

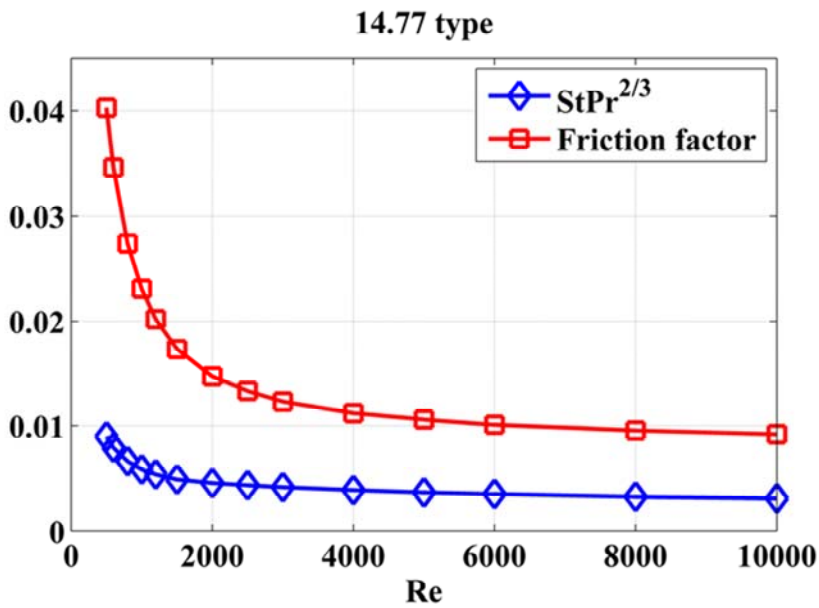


Figure 79. StPr<sup>2/3</sup> and friction factor of 14.77 type Heat exchanger

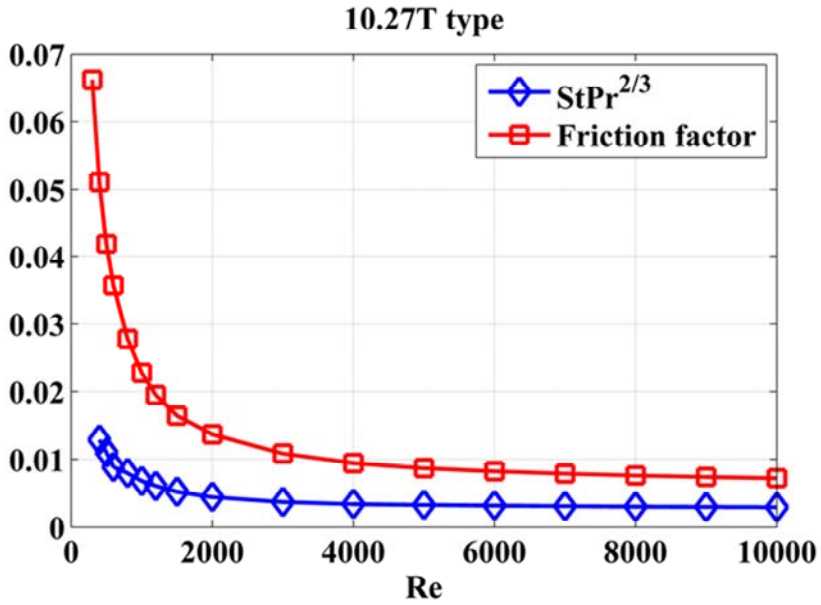


Figure 80. StPr<sup>2/3</sup> and friction factor of 10.27T type Heat exchanger

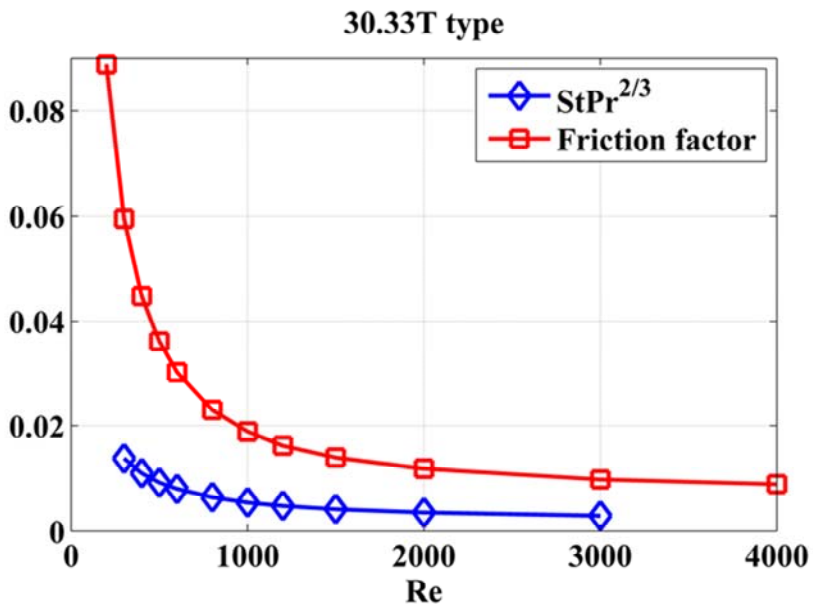


Figure 81. StPr<sup>2/3</sup> and friction factor of 30.33T type Heat exchanger

The optimal case design of the heat exchanger can be defined as bellows.

- The outlet temperature of the exhaust gas is the same to the input temperature of the working fluid. This means that the energy of the exhaust gas is fully absorbed by the working fluid. Thus, the design case which shows the lowest outlet temperature of exhaust gas is the optimal case.
- There is limitation to install the heat exchanger in the engine room. Thus, the design case which shows the smallest size with same performance is the optimal design.

In the case of R245fa, target superheating temperature was determined as 440 K. A pressure drop in the heat exchanger was ignored because it is very small value in a plate fin type. The inlet condition of the heat exchanger was 2.95 MPa and 305 K for the multi-stage turbine. The results of each type heat exchanger are listed in Tables 24 ~ 27.

Table 24. Design results of type 5.3 for R245fa

<b>5.3</b>				
<b>L</b>	<b>W</b>	<b>H</b>	<b>Mass flow rate</b>	<b>Exh. Temp.</b>
<b>m</b>	<b>m</b>	<b>m</b>	<b>kg/s</b>	<b>K</b>
0.8	0.2	0.2	0.10	423.7
	0.3	0.3	0.12	378.0
1	0.2	0.2	0.11	386.0
	0.3	0.3	0.13	343.2

Table 25. Design results of type 14.77 for R245fa

<b>14.77</b>				
<b>L</b>	<b>W</b>	<b>H</b>	<b>Mass flow rate</b>	<b>Exh. Temp.</b>
<b>m</b>	<b>m</b>	<b>m</b>	<b>kg/s</b>	<b>K</b>
0.5	0.2	0.2	0.13	339.0
	0.3	0.3	0.14	305.0
0.6	0.2	0.2	0.14	314.7
	0.3	0.3	0.14	305.0
1	0.2	0.2	0.14	305.0
	0.3	0.3	0.14	305.0

Table 26. Design results of type 10.27T for R245fa

<b>10.27T</b>				
<b>L</b>	<b>W</b>	<b>H</b>	<b>Mass flow rate</b>	<b>Exh. Temp.</b>
<b>m</b>	<b>m</b>	<b>m</b>	<b>kg/s</b>	<b>K</b>
0.3	0.2	0.2	0.08	486.1
	0.3	0.3	0.11	408.3
0.4	0.2	0.2	0.10	437.8
	0.3	0.3	0.12	360.6
0.5	0.2	0.2	0.11	401.5
	0.3	0.3	0.13	328.3

Table 27. Design results of type 30.33T for R245fa

<b>30.33T</b>				
<b>L</b>	<b>W</b>	<b>H</b>	<b>Mass flow rate</b>	<b>Exh. Temp.</b>
<b>m</b>	<b>m</b>	<b>m</b>	<b>kg/s</b>	<b>K</b>
0.2	0.1	0.1	0.09	471.9
	0.2	0.2	0.14	321.1
0.3	0.1	0.1	0.11	405.6
	0.2	0.2	0.14	305.0
0.4	0.1	0.1	0.12	362.2
	0.2	0.2	0.14	305.0

As shown in above tables, the longer and the wider heat exchangers show higher heat transfer performance. As a result, among heat exchangers, a 30.33T type was selected as the optimal type because it showed the highest performance with the smallest volume. The optimal size of type 30.33T is 0.3 X 0.2 X 0.2 case because it is shorter and smaller than 0.4 X 0.2 X 0.2 case.

The optimal design with water was conducted in the same sense. The condition of the working fluid at the heat exchanger inlet is 2.03 MPa and 373 K. The target superheating temperature is 750 K. Moreover, because the flow rate of water is much smaller than that of R245fa, the width and the height were limited under 0.15 m to maintain flow speed. Thus, in order to obtain higher performance of the heat exchanger, the length should be prolonged. However, there was limitation of the length. In Table 28, 1 X 0.15 X 0.15 size of each type heat exchanger shows the highest performance. Consequently, because 30.33T type can recover the largest waste heat energy from exhaust gas, it was selected as optimal case for water.

Table 28. Design result of the heat exchanger for water

Type	L	W	H	Mass flow rate	Exh. Temp.
	m	m	m	kg/s	K
5.30	1	0.15	0.15	0.0084	560.0
14.77		0.15	0.15	0.0142	444.1
10.27T		0.15	0.15	0.0117	480.3
30.33T		0.15	0.15	0.0161	426.9

From the design optimization of the heat exchanger, R245fa can recover more waste heat than water. It is because that the flow rate of R245fa is greater than that of water and the temperature at the heat exchanger inlet of R245fa is lower than that of the water. Thus, application of the WHRS to the series HEV was conducted with the optimal system which adopts R245fa as working fluid, the optimized design of the turbine and the heat exchanger, and the optimized working condition at each component.

#### 4.1.4 Simulation on the WHRS model

The simulation to calculate the work generated from the WHRS was conducted with previous optimization results. The quasi-1D heat exchanger model and the turbine model were linked and calculated according to the engine operation. Because the combination of R245fa, 30.33T type heat exchanger, and 3-stage turbine was estimated to generate the greatest power than other combinations, the simulation was conducted with this combination. The results are listed in Table 29 and Figure 82.

Table 29. Simulation results of turbine and heat exchanger combined model

Operating point	Exh. Temp	Exh. Flow rate	Turbine work	Pump work
	K	Kg/s	kW	kW
1200 rpm – 100 %	750.1	0.126	9.22	0.60
1400 rpm – 100 %	775.2	0.172	8.42	0.87
1600 rpm – 100 %	789.0	0.192	9.70	1.00
1800 rpm – 100 %	804.4	0.220	11.59	1.19
2000 rpm – 100 %	821.1	0.237	12.94	1.32
2300 rpm – 100 %	834.9	0.250	14.08	1.43

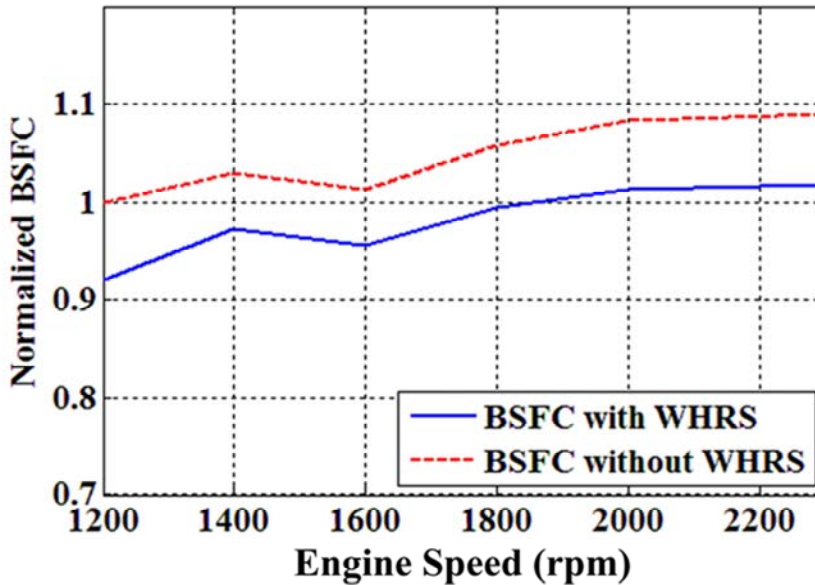


Figure 82. Comparison of BSFC between with and without BSFC

## 4.2 Optimization of system control

### 4.2.1 Dynamic programming

Many previous works have demonstrated dynamic programming to be a global optimization method. Thus, it is applied to solve deterministic problems such as optimal control of the HEV powertrain. The global optimization problem for the fuel economy in a vehicle can be defined as below Eq. (4.2.1) [66, 67].

$$\begin{aligned}
\min \quad & h(\mathbf{x}(t_f)) + \int_{t_0}^{t_f} g(\mathbf{x}(t), \mathbf{u}(t), t) dt \\
s.t. \quad & \dot{\mathbf{x}}(t) = \mathbf{a}(\mathbf{x}(t), \mathbf{u}(t))
\end{aligned} \tag{4.2.1}$$

where,  $\mathbf{x}$  is the state,  $\mathbf{a}$  is the state equation,  $g$  is the performance measure of the problem, and  $\mathbf{u}$  is the control input. From above equation, the optimal cost-to-go function which should be minimized to find out optimal trajectory is defined as Eq. (4.2.2). Eq. (4.2.2) is discrete equation and the process of converting from state equation to discrete equation is described in [67].

$$J_k^*(x_k) = \min_{u_k} \{g_k(x_k, u_k) + J_{k+1}^*(a(x_k, u_k))\} \tag{4.2.2}$$

where,

$$x_{k+1} = a(x_k, u_k) \tag{4.2.3}$$

The process of dynamic programming to find out optimal trajectory can be described as Figure 83.

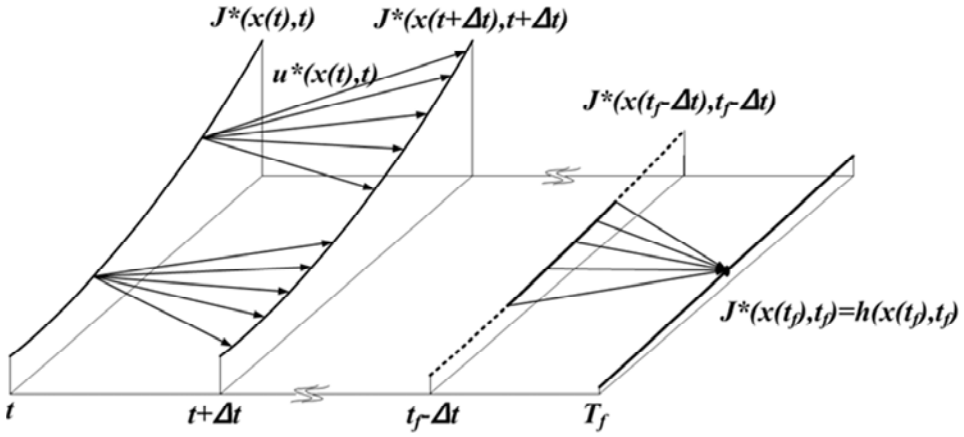


Figure 83. Finding out optimal trajectory based on Bellman's optimality [67]

Thus, dynamic programming was selected as the simulation method to estimate the theoretical improvement in the fuel economy when the heat recovery system was applied to the series HEV. Because the target system adopted the waste heat recovery system, the optimization problem was re-defined.

The most important factor in dynamic programming is the cost-to-go function, which coincides with the fuel consumption. The work produced by the WHRS is assumed to be used to generate electric energy. The output power of the WHRS is determined when the engine operating point is selected. Thus, the power of the engine and the turbine was summed, while the fuel consumption remained at the same level when only the engine is used. The control input at time  $k$  can be determined as in Eq. (4.2.4).

$$u_k = P_{bat} = P_{required} - (\eta_{gen,engine} P_{engine} + \eta_{gen,WHRS} P_{WHRS}) \quad (4.2.4)$$

where,  $P_{bat}$  is battery power,  $P_{required}$  is required power to drive vehicle,  $P_{engine}$  is engine power, and  $P_{WHRS}$  is power generated by the WHRS.  $\eta_{gen,engine}$  and  $\eta_{gen,WHRS}$  are efficiency of generators which are connected with the engine and the WHRS, respectively.

#### 4.2.2 ECMS

Equivalent Consumption Minimization Strategy is a kind of local optimization methods. It optimizes the cost function which is related with only fuel economy instantaneously. To minimize fuel economy, the best cost is defined as Eq. (4.2.5).

$$\underset{P_d(t)}{\text{Min}} \int \dot{m}_f(t) dt \quad (4.2.5)$$

where,  $P_d$  and  $\dot{m}_f$  are required power from vehicle and fuel consumption rate, respectively. Above equation means minimization of fuel economy during overall test cycle. However, in real-time environment, it is impossible to obtain whole drive cycle. Thus, the equation is corrected by an instantaneous cost, in an instantaneous optimization problem. The instantaneous optimal cost can be defined as Eq. (4.2.6).

$$\int \underset{P_d(t)}{\text{Min}} [\dot{m}_f(t)] dt \quad (4.2.6)$$

This instantaneous optimal cost is not equivalent to the global optimization problem such as dynamic programming, but the computation load is much smaller than that of global optimization problem. Although the local optimal result is not matched to the global optimal results perfectly, it shows

similar control trend which can achieve high fuel economy. From this concept, fuel consumption which should be minimized is determined as follow [68, 69].

$$\dot{m}_{f\_eq}(t) = \dot{m}_{f\_eng} + \dot{m}_{f\_bat} \quad (4.2.7)$$

where,  $\dot{m}_{f\_eq}$ ,  $\dot{m}_{f\_eng}$ , and  $\dot{m}_{f\_bat}$  mean the total equivalent fuel consumption, the fuel consumption of engine and the equivalent fuel consumption of the battery, respectively.  $\dot{m}_{f\_eng}$  is calculated based on the required power of the engine and the fuel consumption map. The equivalent fuel consumption of the battery is defined as below with consideration of the electrical efficiency ( $\eta_{elec}$ ) and the electric energy conversion factor ( $SC_{eng}$ ).

$$\dot{m}_{f\_bat} = \frac{SC_{eng} \cdot P_{bat}}{\eta_{elec}} \quad (4.2.8)$$

Where,  $P_{bat}$  is the battery power. The  $SC_{eng}$  is the core factor of ECMS because it determines system operation. Thus, it is very important to define proper  $SC_{eng}$  value. To obtain optimal  $SC_{eng}$ , the relationship between the use of the electric energy and the fuel energy in a specific vehicle powertrain system and test cycle should be investigated. The concept of the equivalent fuel consumption is described in [70].

To obtain proper  $SC_{eng}$ , the relationship between the chemical energy of fuel and the electric energy should be defined. In order to obtain proper  $SC_{eng}$  value, the vehicle simulation is conducted with various initial SOC condition. For instance, if various cases of the simulation are conducted, the results can be plotted as Figure 84 [70].

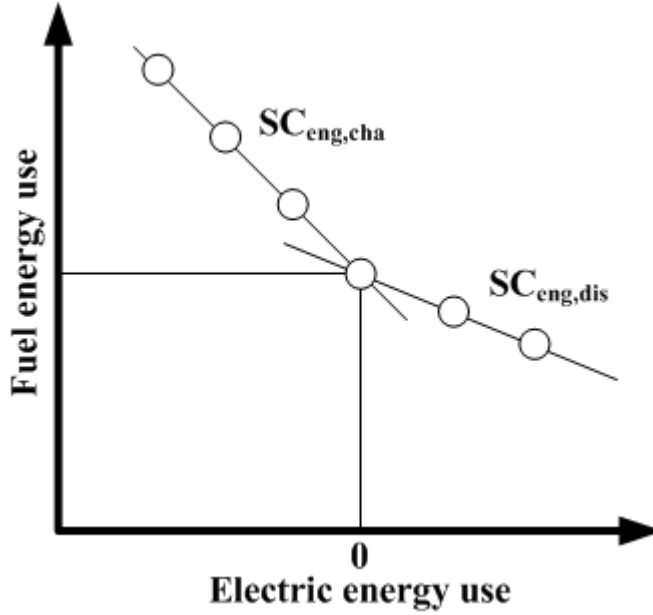


Figure 84. Determination of  $SC_{eng}$  factor from slope value

As shown in Figure 84,  $SC_{eng}$  can be determined as gradient value. However,  $SC_{eng}$  shows different value in charge and discharge processes. It is because the efficiencies of the energy conversion process in charge and discharge processes have different values.

In addition, the battery use should be limited when the battery is in dangerous SOC range to protect the battery from damage. Thus, penalty factor is considered as Eq. (4.2.9) in this study [69].

$$f(SOC) = 1 - (1 - 0.7x_{SOC}) \cdot x_{SOC}^3 \quad (4.2.9)$$

where,

$$x_{SOC} = \frac{SOC - \frac{SOC_L + SOC_H}{2}}{SOC_H - SOC_L} \quad (4.2.10)$$

$SOC_L$  and  $SOC_H$  are the low and high limit of the battery SOC, respectively. Thus, the fuel consumption can be determined as below equation.

$$\dot{m}_{f\_eq}(t) = \dot{m}_{f\_eng} + f(SOC)\dot{m}_{f\_bat} \quad (4.2.11)$$

By using Eq. (4.2.11), ECMS for the target system was calculated and implemented as map data for application in the vehicle simulation.

### 4.2.3 Simple strategy (Thermostatic control strategy)

In many series HEV applications, simple control strategy has been adopted because it is easy to be implemented in embedded hardware and error can be prevented due to its simplicities. In addition, because the engine is operated at only the target point, WHRS can be operated with constant heat source. Thus, in this study, simple strategy was adopted and applied with the target system. The target operating point was set as 1200 rpm – 100 % load, because bsfc shows minimum value at this point. The strategy to determine engine operation is described in Figure 85.

As shown in Figure 85, the generation system starts to be operated when SOC reaches 0.45. Then, the battery is charged when SOC reaches 0.6. After charging, the generation system is turned off.

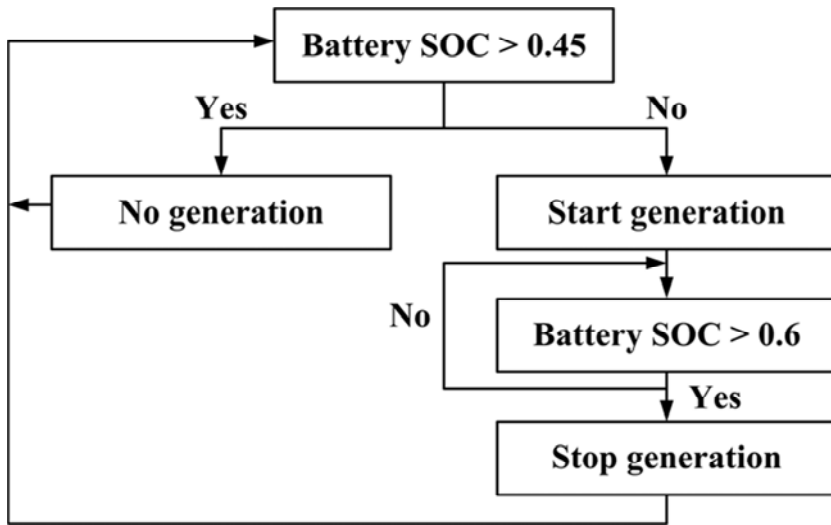


Figure 85. A flow chart of the thermostatic control strategy

## Chapter 5. Simulation results

### 5.1 Results of engine transient simulation

The engine is warmed up from cold start. In this transient period, temperatures of the coolant, the engine metal parts and the exhaust gas are increased. In other words, the temperatures of the exhaust gas and the coolant at start state are not high enough to be used as heat sources for the WHRS. Thus, it is important to estimate the temperature of the exhaust gas during warm up period. To estimate change of the exhaust gas temperature, 1-D engine model and ETM model were cooperated through semi-iteration. As described in previous chapter, simulation step times of 1-D engine model and ETM model show large difference. Thus, 1-D engine model and ETM model were calculated separately. The schematic of semi-iterative simulation is shown in Figure 86.

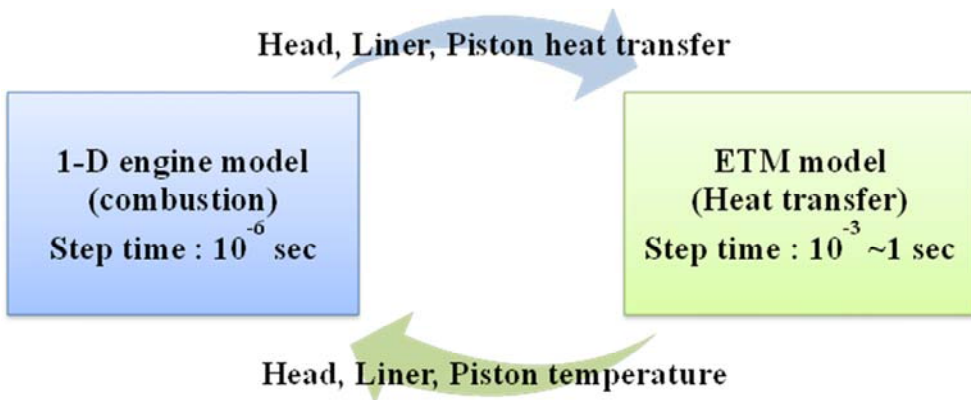


Figure 86. A schematic of semi-iterative simulation method

The simulation was conducted with 1200 rpm – 100 % condition because the engine is operated mainly at this point in the conventional SHEV. At atmospheric initial condition, the transient temperature changes of exhaust gas, coolant, piston, head and liner are shown in Figures 87 and 88. The piston, head and liner of # 3 cylinder were used because they show medium values.

As shown in Figure 87, a liner took the longest time to be converged while piston took the shortest time. It is because the liner is exposed to coolant with the largest heat exchange area. Piston temperature has the highest value because convection heat transfer occurs by only piston oil jet which has much smaller cooling effect than that of coolant. However, in piston heat transfer, piston jet is very important to maintain piston temperature at target value.

The most important fact in the result is the trend of the exhaust gas temperature. Because the WHRS uses the exhaust gas as heat source, exhaust gas temperature affects the WHRS operation. The ideal WHRS operation occurs when the exhaust gas is supplied as design condition. In this study, the design condition of the exhaust gas is fully warmed-up state. Thus, the temperature of the exhaust gas should be over 800 K to ensure the general WHRS operation. As shown in Figure 88, the exhaust gas temperature reached at 800 K after about 80 sec. From this, it is known that the WHRS should be operated after 80 sec from the start of the engine.

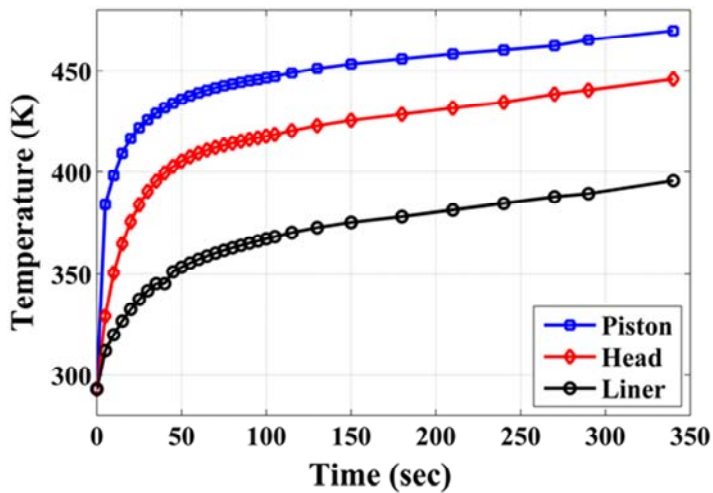


Figure 87. Transient simulation result of engine metal parts with 1-D engine model and ETM model under 1200 rpm – 100 % condition at cold start

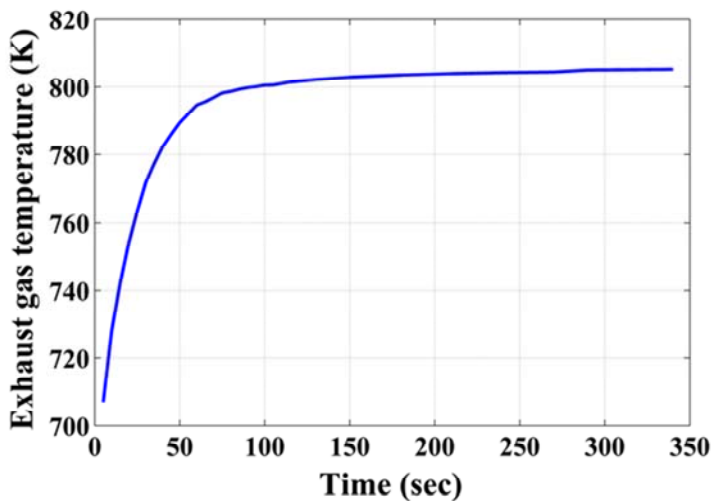


Figure 88. Transient simulation result of exhaust gas with 1-D engine model and ETM model under 1200 rpm – 100 % condition at cold start

## 5.2 Results of vehicle simulation

### 5.2.1 Test cycles

In this study, 5 test cycles were adopted to calculate improvement in fuel economy. KATECH 150, KATECH G, Braunschweig, Heavy duty UDDS, and JE05 are shown in Figures 89 ~ 93 [71]. The specifications of the cycles are listed in Table 30. Especially, KATECH 150 and KATECH G were measured at real bus route in Seoul to reflect real traffic environment. A measured data was after-treated using statistical method. Although they are not officially approved in Korea, because the target vehicle is intra-city bus which is driven in Seoul, Korea, they were adopted as test cycles. Heavy-duty UDDS, Braunschweig, and JE05 are used in USA, Europe, and Japan, respectively.

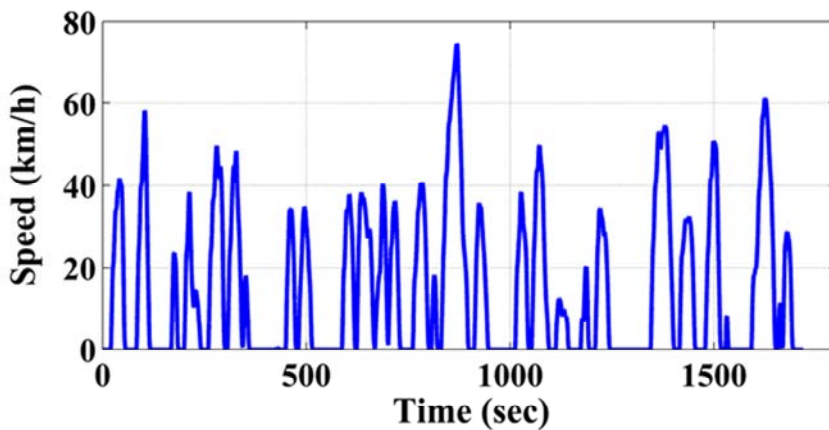


Figure 89. A speed profile of KATECH 150

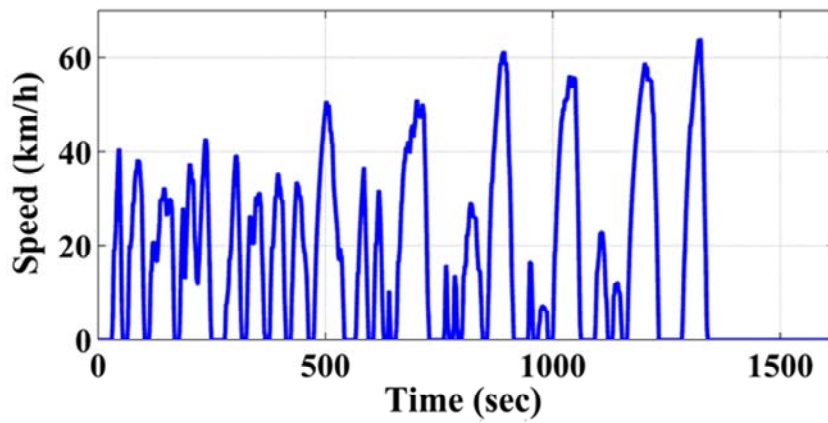


Figure 90. A speed profile of KATECH G

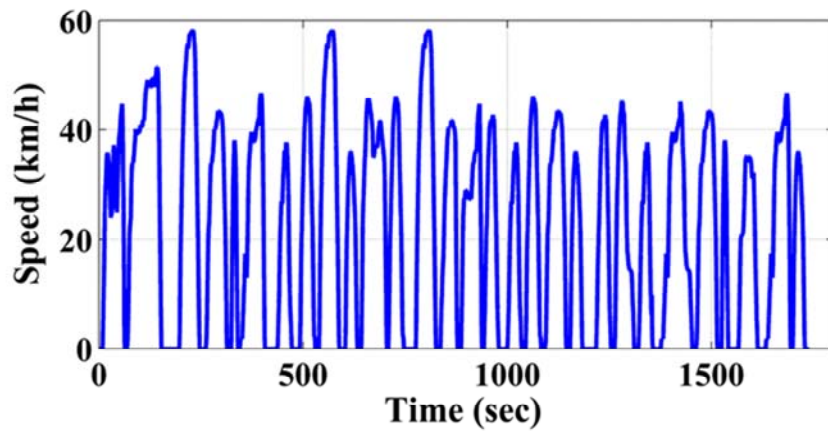


Figure 91. A speed profile of Braunschweig cycle

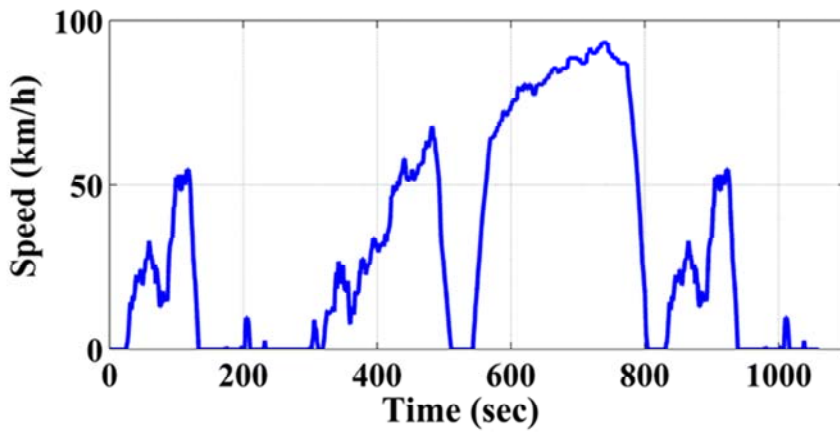


Figure 92. A speed profile of heavy-duty UDDS

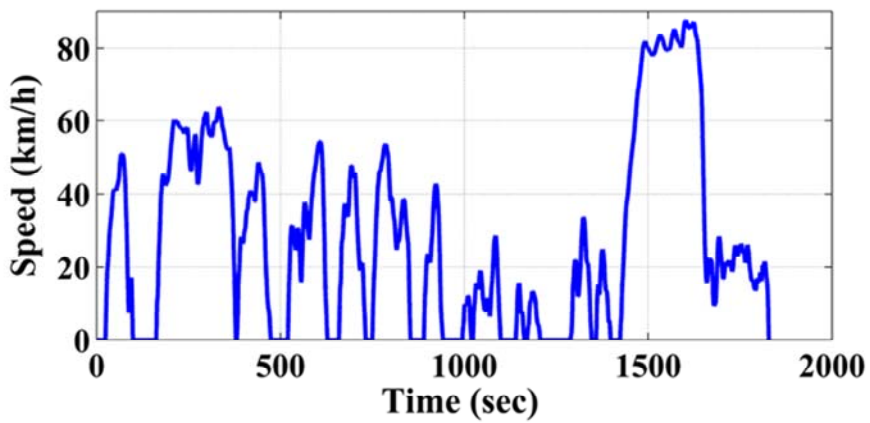


Figure 93. A speed profile of JE05

Table 30. Specifications of the test cycles

Test cycle	Duration (sec)	Distance (km)	Max. speed (km/h)	Ave. speed (km/h)
KATECH 150	1719	7.0	74.7	14.5
KATECH G	1613	7.1	64.5	15.9
Braunschweig	1740	11.0	58.2	22.9
HD-UDDS	1060	8.9	93.3	30.4
JE05	1829	13.9	88	26.9

### 5.2.2 Results of Dynamic Programming

By using dynamic programming, optimal control strategy for the target system can be obtained. A comparison of fuel economy between the conventional system and the target system was conducted. The results of each cycle are described in Figures 94 ~ 108. The trajectories of the SOC show similar trends regardless of application of WHRS. It means that two systems require generation of electric energy at same situation to minimize fuel consumption. The engine operating ranges of two systems show slight difference. As shown in Figures 95, 98, 101, 104 and 107, the target system operates engine around 100 kW mainly, whereas the conventional system operates engine around 80 kW mainly. However, overall operating ranges of two system are established around 80 ~ 100 kW. It means that engine operating range is not changed significantly even if WHRS is applied. In addition, operation timing of generation system was almost the same for both systems. Consequently, it is obvious that the overall control trend of the target system is not changed greatly compared to the conventional system. Thus, when the WHRS is designed and optimized for target system, it is conducted based on the main operation range of conventional system.

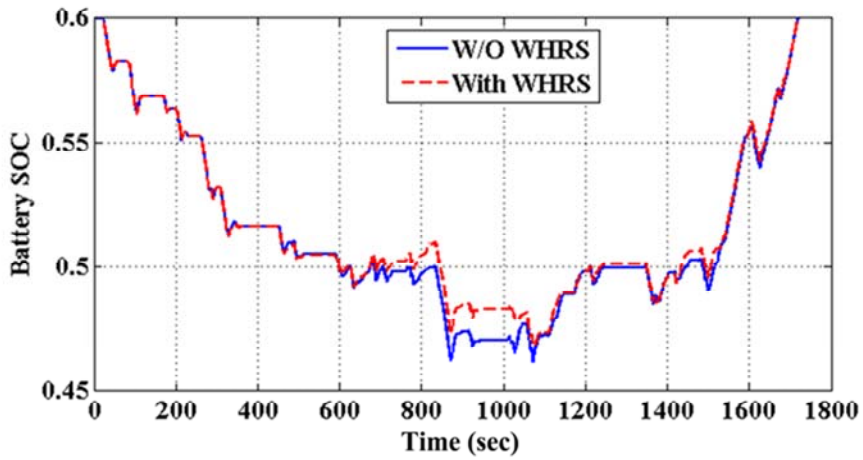


Figure 94. A SOC trajectory in KATCH 150

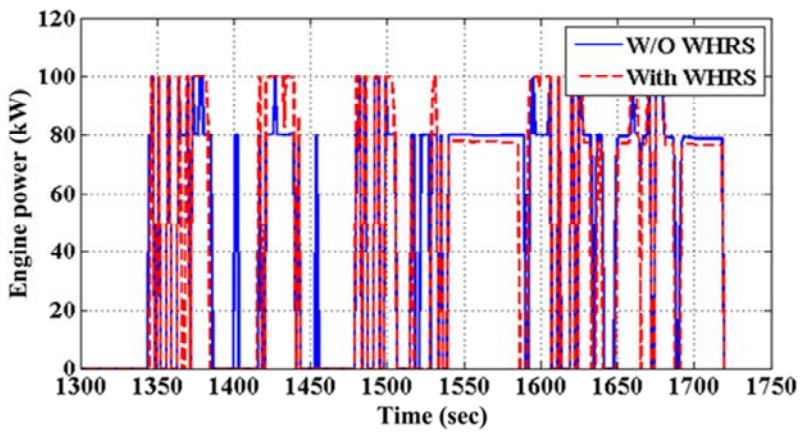


Figure 95. Engine operation power in KATCH 150 (1300~1750 sec)

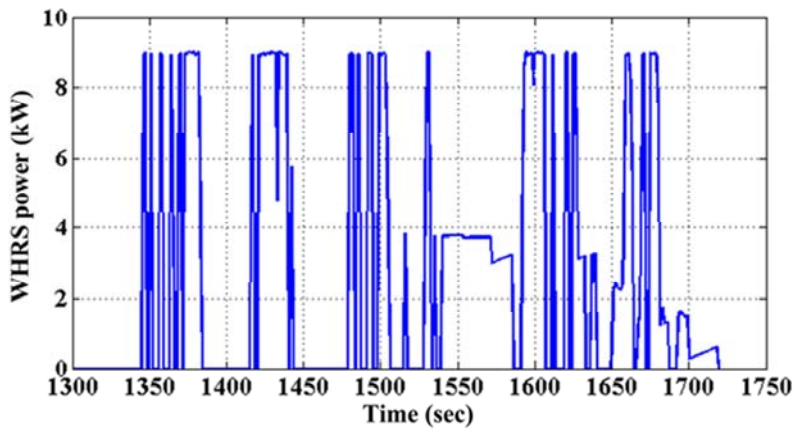


Figure 96. WHRS operation power in KATCH 150 (1300~1750 sec)

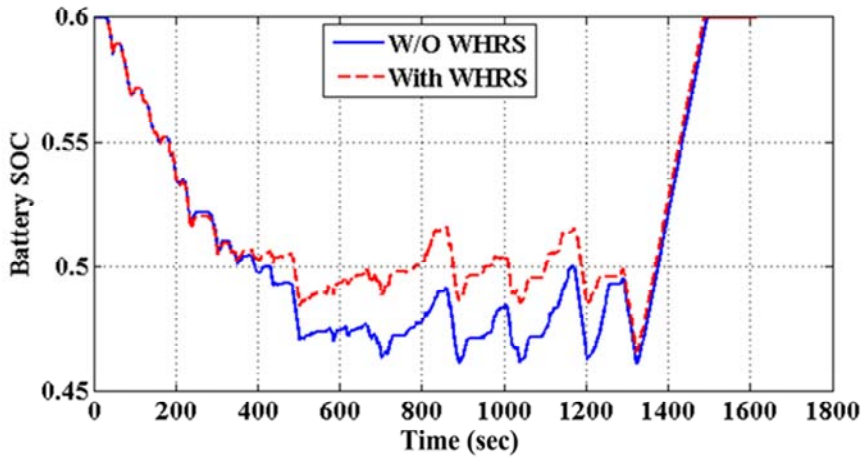


Figure 97. A SOC trajectory in KATCH G

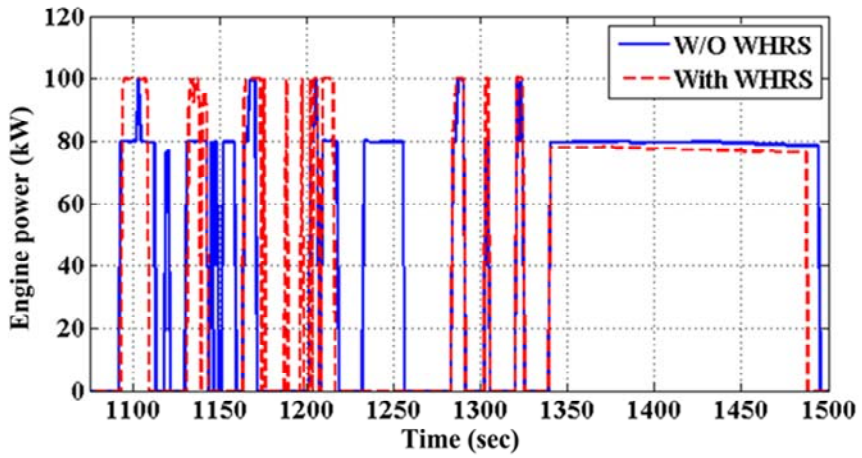


Figure 98. Engine operation power in KATCH G (1075~1500 sec)

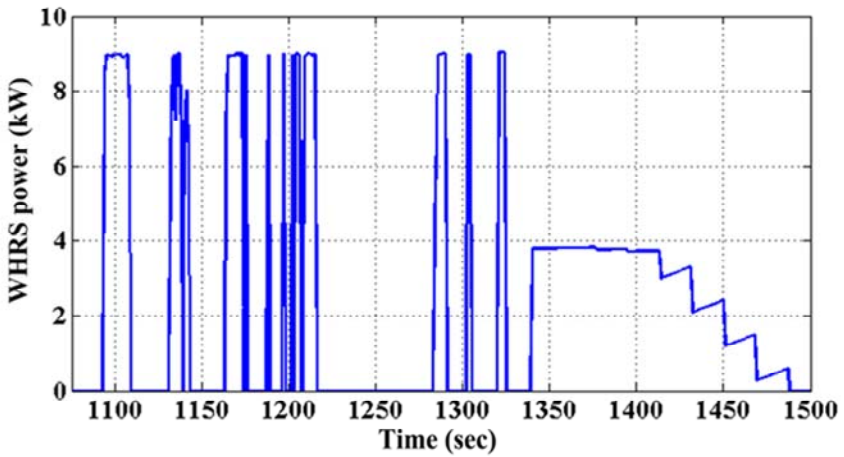


Figure 99. WHRS operation power in KATCHE G (1075~1500 sec)

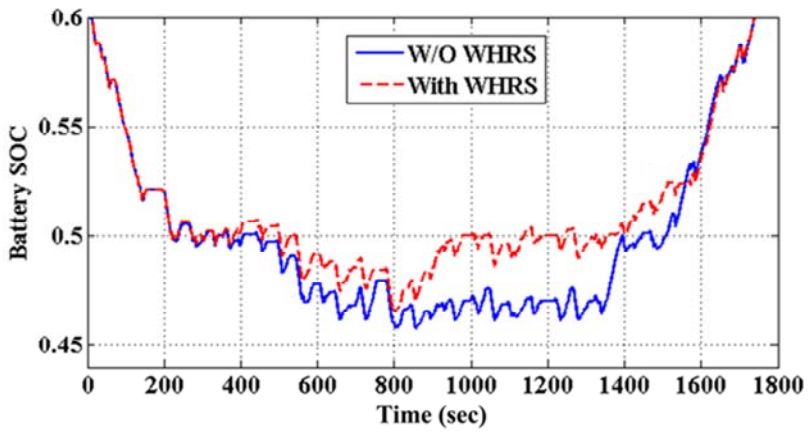


Figure 100. A SOC trajectory in Braunschweig

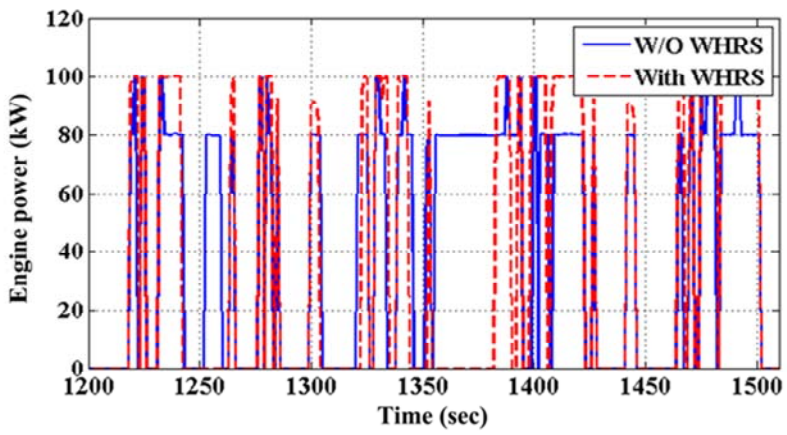


Figure 101. Engine operation power in Braunschweig (1200 ~ 1510 sec)

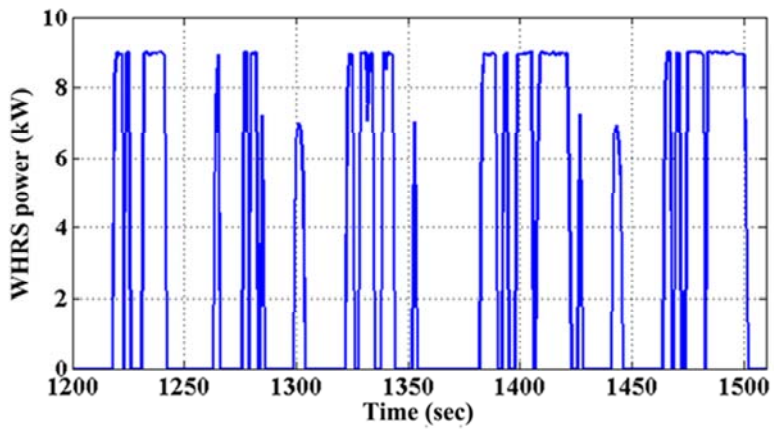


Figure 102. WHRS operation power in Braunschweig (1200 ~ 1510 sec)

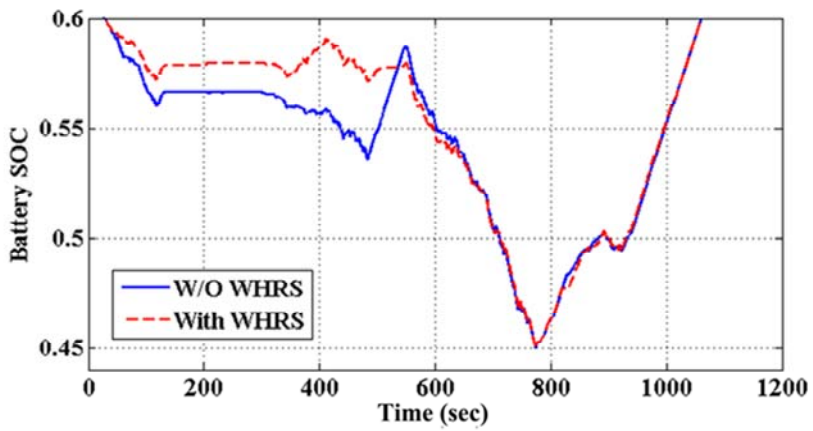


Figure 103. A SOC trajectory in Heavy-duty UDDS

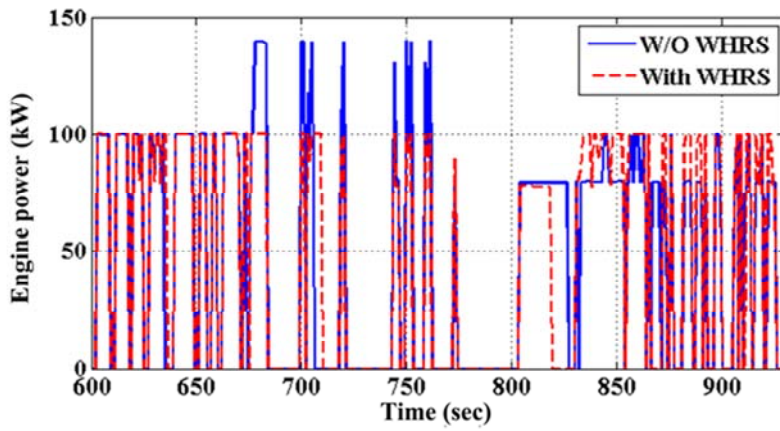


Figure 104. Engine operation power in Heavy-duty UDDS (600 ~ 930 sec)

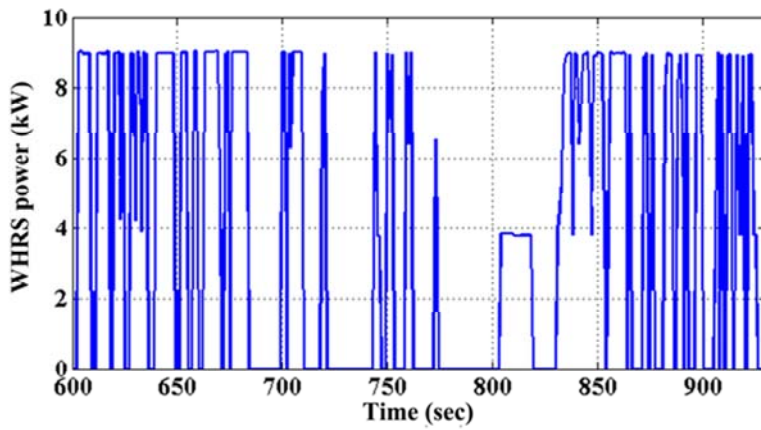


Figure 105. WHRS operation power in Heavy-duty UDDS (600 ~ 930 sec)

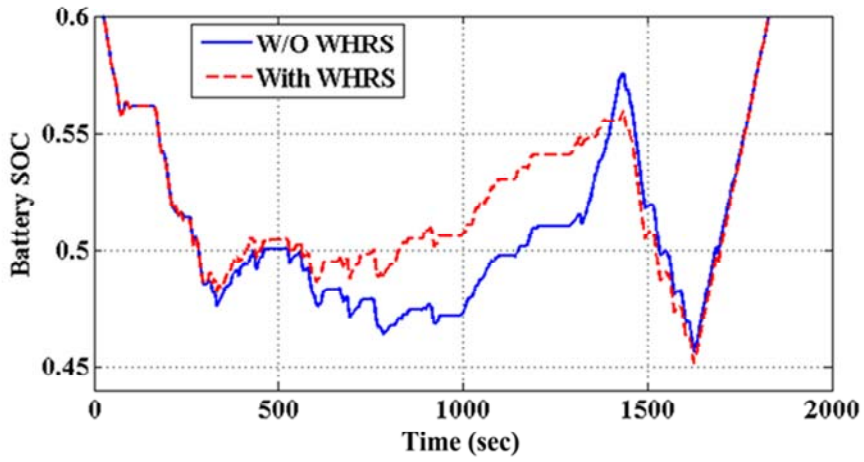


Figure 106. A SOC trajectory in JE05

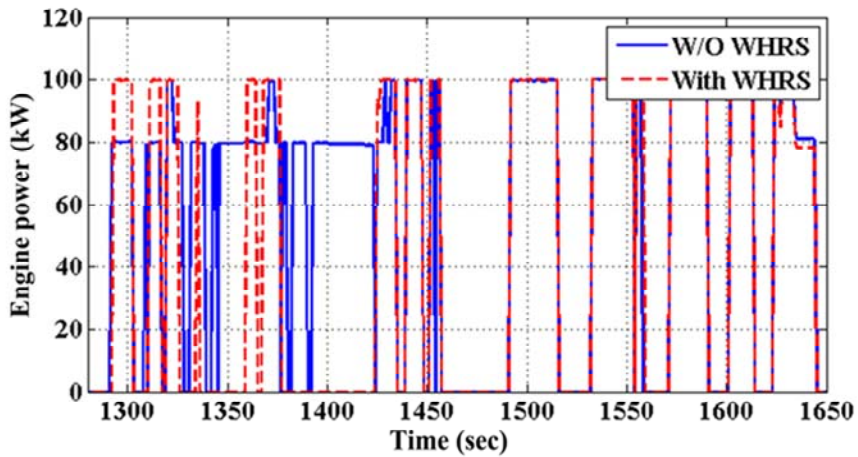


Figure 107. Engine operation power in JE05 (1280 ~ 1650 sec)

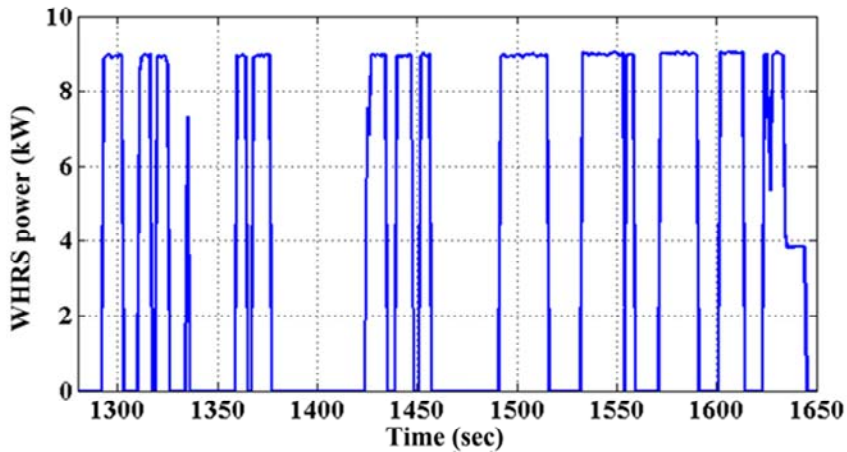


Figure 108. WHRS operation power in JE05 (1280 ~ 1650 sec)

The fuel economy and engine operating duration of each test cycle are listed in Table 31. The density of fuel is  $0.654 \text{ kg/Nm}^3$  which is used in EURO as standard value. As shown in Table 31, when the duration of engine operating is relative long, reduction of that with WHRS is greater than other cases. WHRS generates more energy as the engine operation duration increased. In other words, because the generation system generates almost same energy regardless of WHRS application in same cycle, the reduction of the engine operation duration become greater as the duration increased. It is because that the energy generated by WHRS is increase. The relation between engine generation energy and improvement is shown in Figure 109. As the engine generation energy is higher, the duration of the engine operation is increased, too. Thus, it is obvious that more improvement can be achieved when the engine is more used in the conventional system.

Table 31. The results of Dynamic Programming

Cycle	Type	Fuel economy (km/Nm <sup>3</sup> )	Duration (sec)	Improvement (%)
KATECH 150	Convention	2.57	414	6.28
	WHRS	2.73	351	
KATCH G	Convention	2.30	471	6.11
	WHRS	2.44	401	
Braunschweig	Convention	2.52	658	7.09
	WHRS	2.70	530	
HD-UDDS	Convention	2.94	438	6.17
	WHRS	3.12	392	
JE05	Convention	2.68	756	7.35
	WHRS	2.88	628	

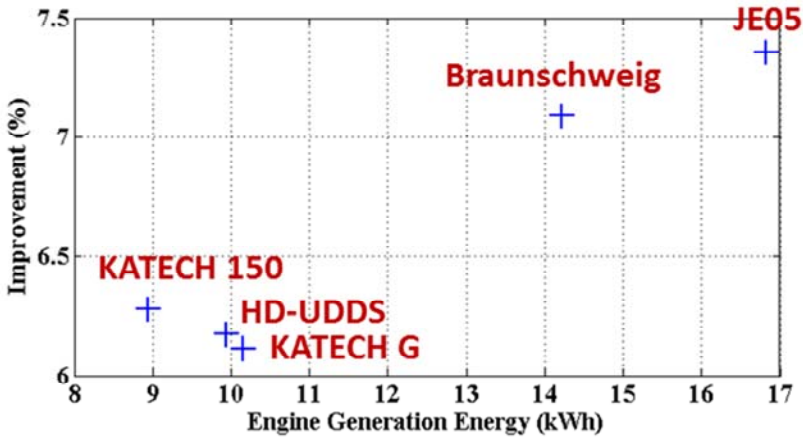


Figure 109. A relation between the engine generation energy and improvement

### 5.2.3 Results of ECMS application

As described in previous chapter, in order to obtain ECMS rule, the relationship between electric energy and fuel energy consumption should be defined about specific configuration of vehicle and test cycle. Thus, simulation to obtain  $SC_{eng}$  was conducted with configuration of conventional case and WHRS case, and test cycles. Because states of charge and discharge show similar slope value about all cases,  $SC_{eng}$  was assumed as single value when test cycle and configuration are not changed. In order to implement WHRS in forward type overall vehicle model, the map which reflects the WHRS results was constructed. The calculation results of  $SC_{eng}$  are listed Table 32 and shown in Figures 110 ~ 114.

Table 32.  $SC_{eng}$  values according to test cycles and configurations

Cycle	$SC_{eng}$ (W/O WHRS)	$SC_{eng}$ (with WHRS)
KATECH 150	0.0601	0.0562
KATCH G	0.0602	0.0563
Braunschweig	0.0616	0.0563
HD-UDDS	0.0611	0.0538
JE05	0.0562	0.0532

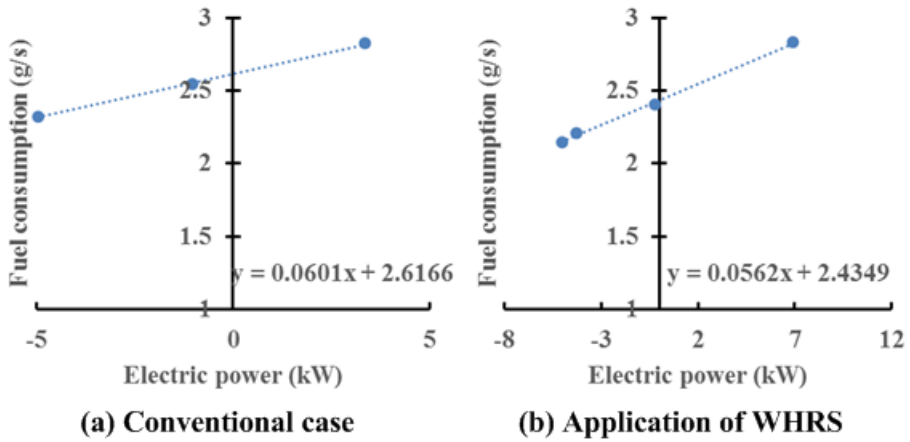


Figure 110. Determining a  $SC_{eng}$  value without WHRS (a) and with WHRS (b) in KATECH 150

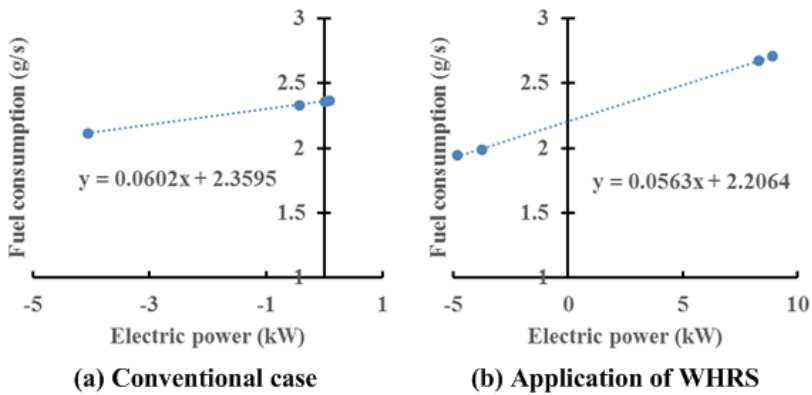
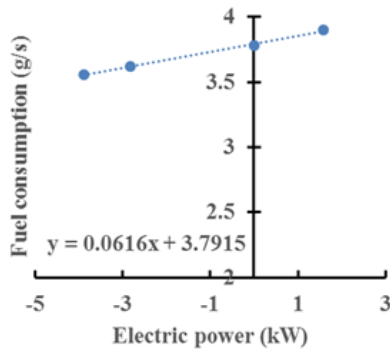
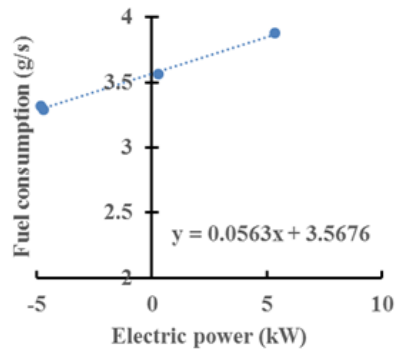


Figure 111. Determining a  $SC_{eng}$  value without WHRS (a) and with WHRS (b) in KATECH G

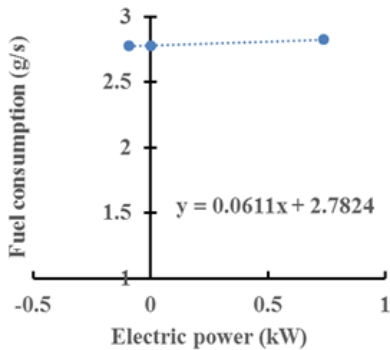


(a) Conventional case

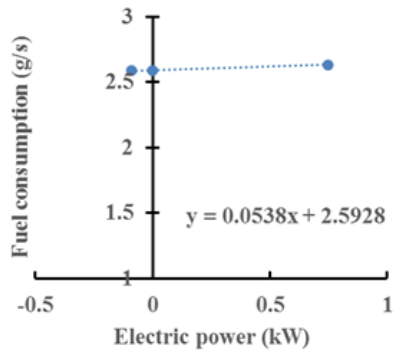


(b) Application of WHRS

Figure 112. Determining a  $SC_{eng}$  value without WHRS (a) and with WHRS (b) in Braunschweig



(a) Conventional case



(b) Application of WHRS

Figure 113. Determining a  $SC_{eng}$  value without WHRS (a) and with WHRS (b) in Heavy-duty UDDS

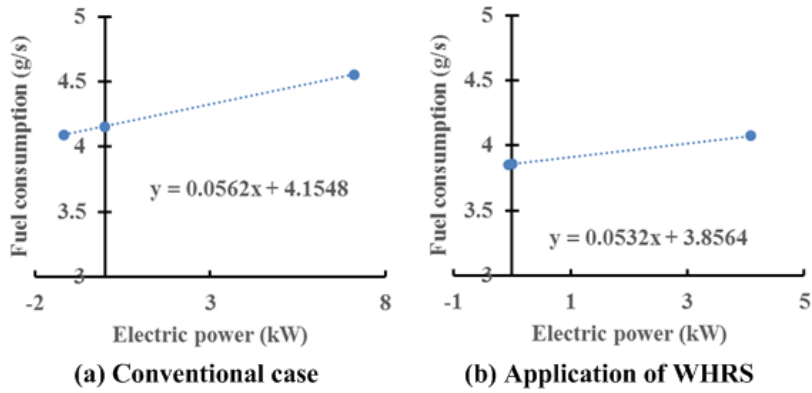


Figure 114. Determining a  $SC_{eng}$  value without WHRS (a) and with WHRS (b) in JE05

As shown in above figures, the gradient which is ratio between electric power and fuel consumption rate is decreased with WHRS. It means that more electric energy is generated with same fuel energy. Based on these  $SC_{eng}$  values, ECMS maps for each cycle and configuration were calculated. They are shown in Figures 115 ~124.

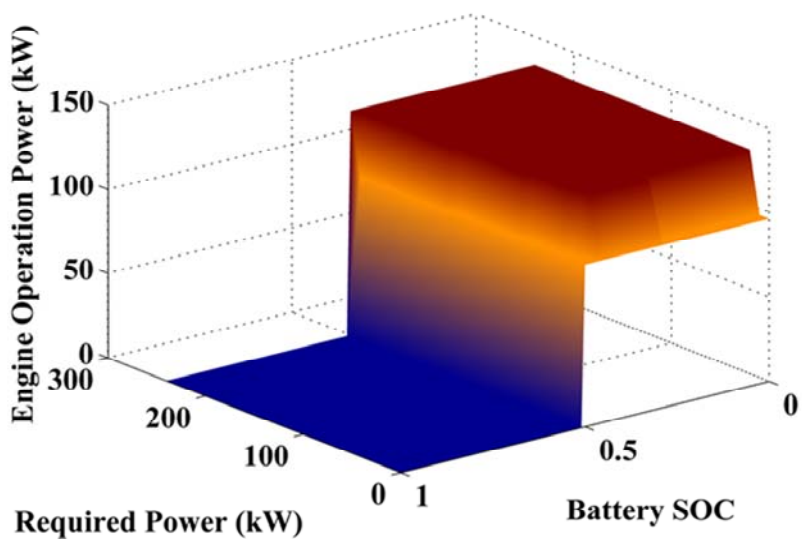


Figure 115. ECMS map without WHRS in KATECH 150

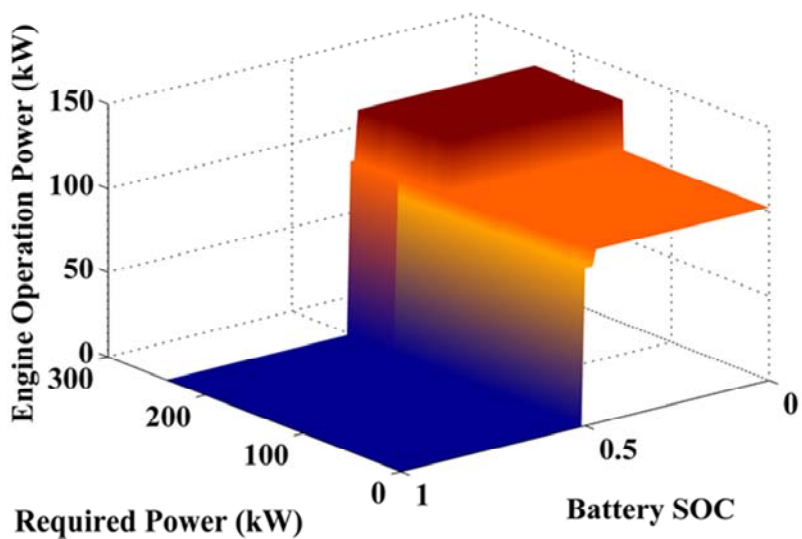


Figure 116. ECMS map with WHRS in KATECH 150

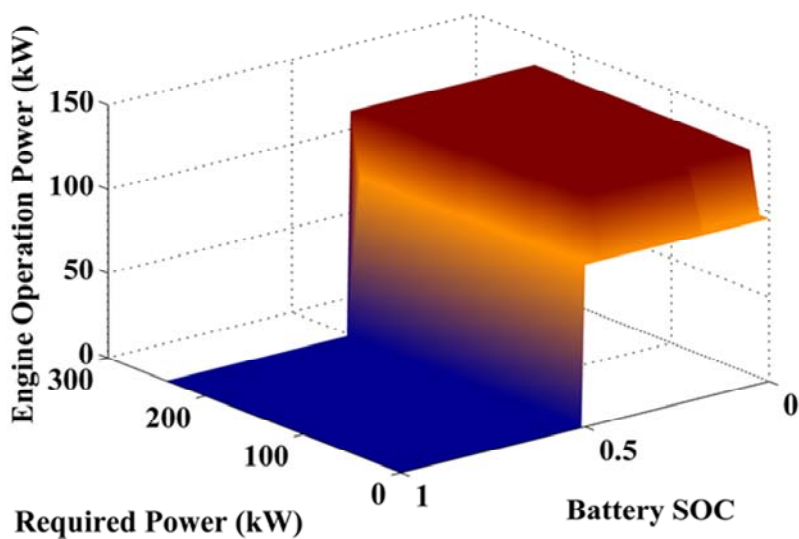


Figure 117. ECMS map without WHRS in KATECH G

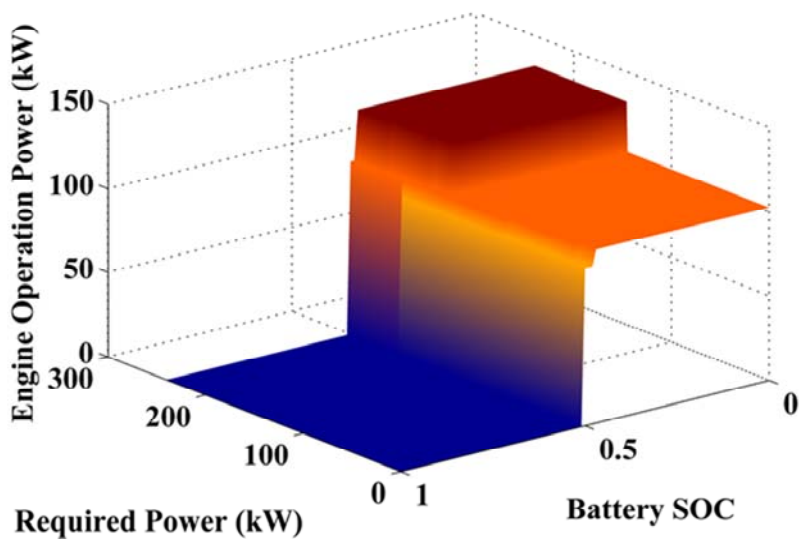


Figure 118. ECMS map with WHRS in KATECH G

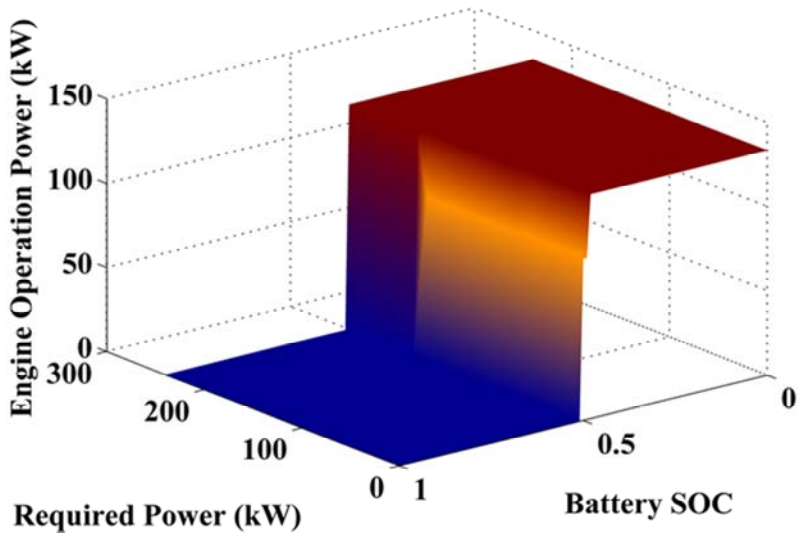


Figure 119. ECMS map without WHRS in Braunschweig

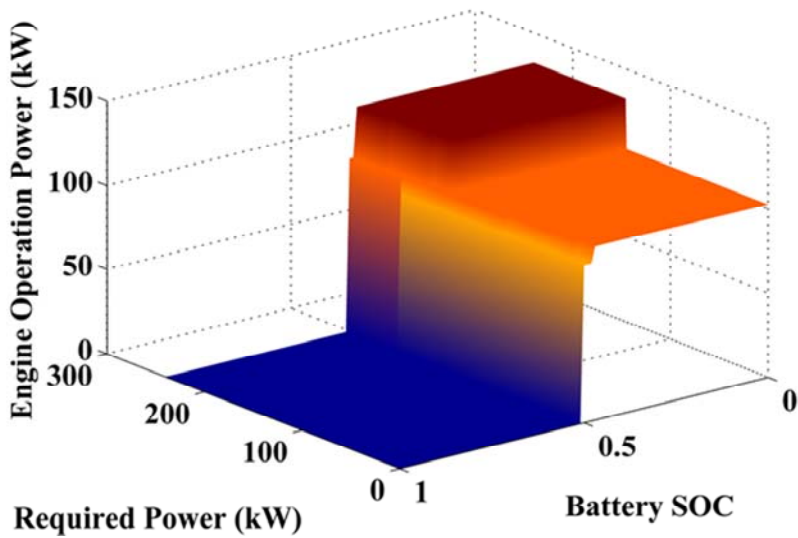


Figure 120. ECMS map with WHRS in Braunschweig

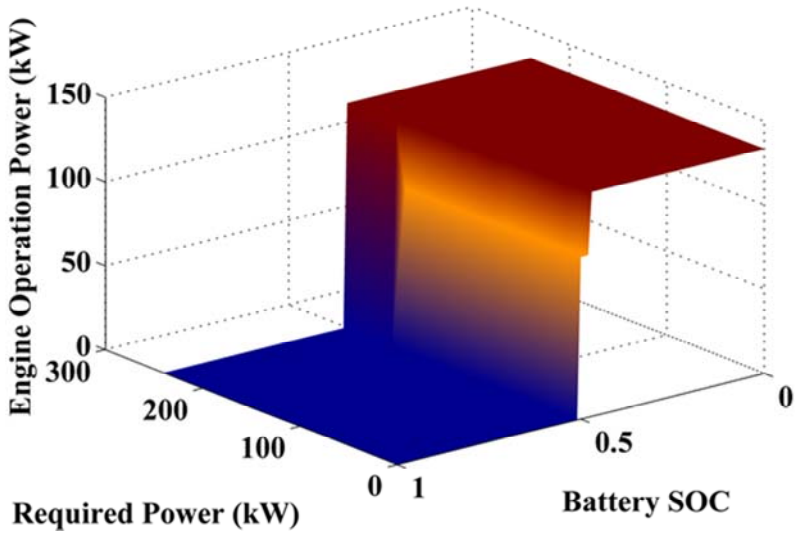


Figure 121. ECMS map without WHRS in Heavy-duty UDDS

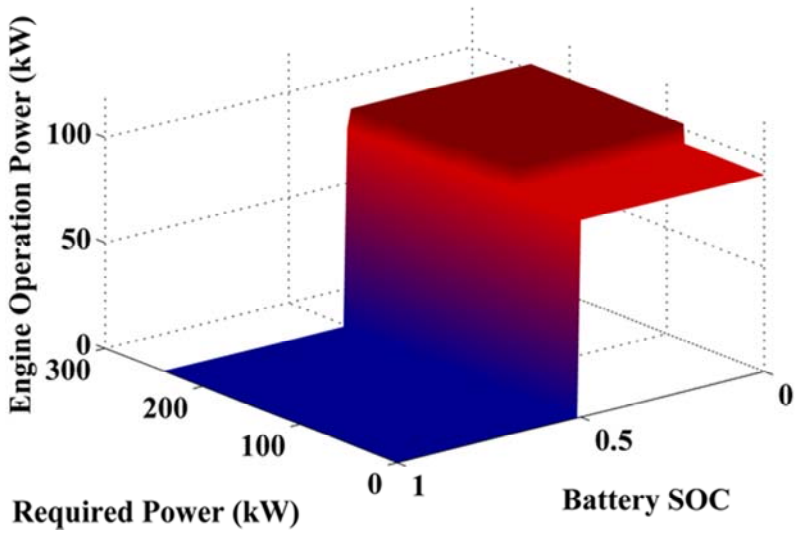


Figure 122. ECMS map with WHRS in Heavy-duty UDDS

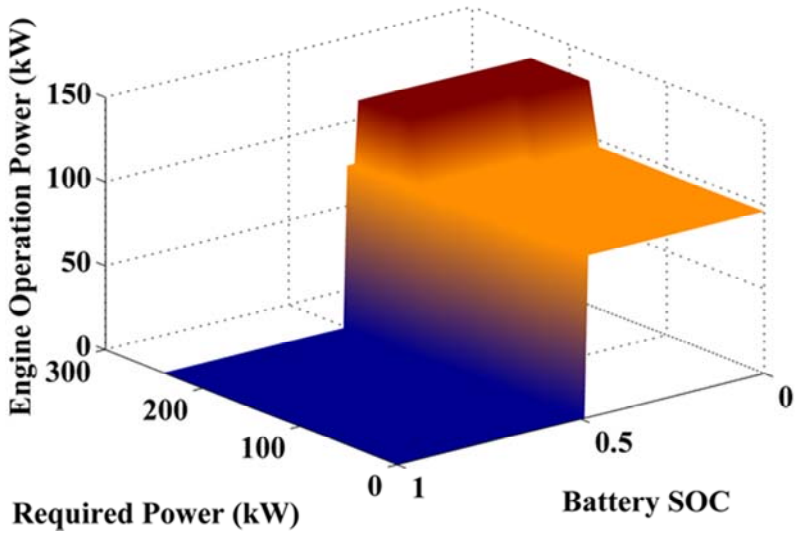


Figure 123. ECMS map without WHRS in JE05

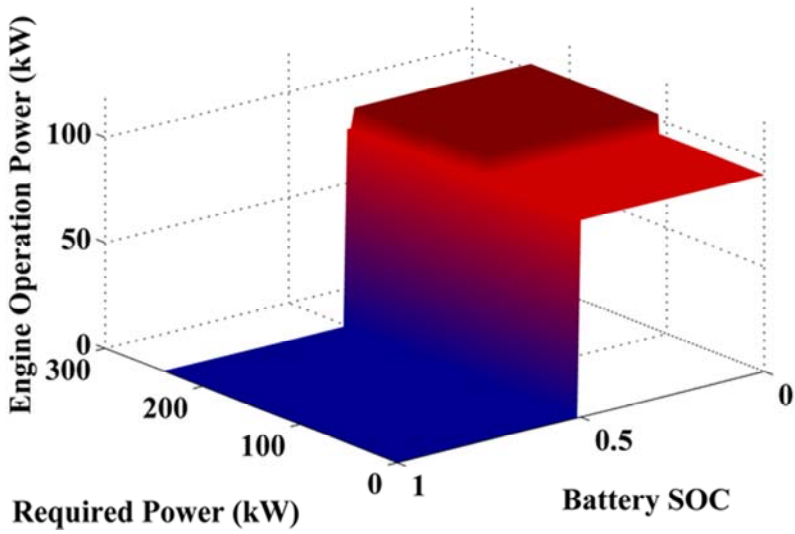


Figure 124. ECMS map with WHRS in JE05

Table 33. Results of forward simulation with ECMS

<b>Cycle</b>	<b>Type</b>	<b>Fuel economy (km/Nm<sup>3</sup>)</b>	<b>Improvement (%)</b>
KATECH 150	Convention	1.78	7.03
	WHRS	1.91	
KATCH G	Convention	1.99	6.90
	WHRS	2.12	
Braunschweig	Convention	1.89	6.70
	WHRS	2.02	
HD-UDDS	Convention	2.09	7.66
	WHRS	2.25	
JE05	Convention	2.20	6.60
	WHRS	2.35	

The results with ECMS are listed Table 33. Fuel economy was improved when WHRS was applied. However, absolute values of fuel economy show much smaller than that of dynamic programming. It is caused from difference between backward and forward simulation method. In backward simulation, dynamics of engine, motor, and generator are not considered, whereas they are considered in forward type simulation. In addition, rapid engine on/off is possible in backward type while it is impossible in forward type. The use of electric energy to start engine is not considered in backward type. From these reasons, forward type simulation shows lower fuel economy than backward type simulation.

#### **5.2.4 Results of thermostatic control strategy**

The results of thermostatic control strategy are listed in Table 34. Fuel economy of thermostatic control strategy was lower or the same level compared with that of ECMS. However, generally, because ECMS is optimal control strategy, fuel economy of ECMS is higher than that of thermostatic control strategy. In the case of parallel HEV, ECMS determines power split ratio of motor and engine. Moreover, engine is always operated because it is connected with drive shaft. Thus, by using ECMS which determines instantaneous optimal power split ratio, fuel economy can be much improved compared simple control strategy of which power split ratio is fixed. However, in the case of series HEV, engine is not connected with drive shaft. It means that the engine can be operated regardless of vehicle driving state. Therefore, instantaneous optimal operating point of the engine is determined as minimum bsfc point. As shown in ECMS maps, when the generation system is operated, operating range of the engine is 80 ~ 100 kW. It is similar with dynamic programming results. In addition, the target operating point of the engine of thermostatic control strategy is defined as 100 kW. Thus, ECMS and thermostatic control strategy show similar results.

In addition, the fuel economy of fully warmed-up and cold start condition were compared. By deactivating the WHRS operation 80 seconds after the engine start, cold start condition was implemented in vehicle simulation. In contrast, the WHRS begins to operate when engine runs at fully warmed-up start condition. As a result, 140 g of fuel could be saved under the fully warmed-up condition with simple control strategy regardless of driving cycles. It is because the engine had to be operated for longer time under the cold start

condition compared to the fully warmed-up condition as the WHRS was deactivated before the engine was fully warmed up.

Table 34. Results of forward simulation with thermostatic control strategy

<b>Cycle</b>	<b>Type</b>	<b>Fuel economy (km/Nm<sup>3</sup>)</b>	<b>Improvement (%)</b>
KATECH 150	Convention	1.75	8.15
	WHRs	1.89	
KATCH G	Convention	1.94	9.35
	WHRs	2.13	
Braunschweig	Convention	1.88	6.67
	WHRs	2.00	
HD-UDDS	Convention	2.10	7.31
	WHRs	2.25	
JE05	Convention	2.19	7.65
	WHRs	2.36	

## Chapter 6. Conclusion

In this study, WHRS with the SHEV was optimized with consideration of the target vehicle and operation environment. Analysis on the heat sources was conducted and operating conditions of the engine for using heat sources were investigated. The engine, traction motor, generator, electrochemical Li ion battery, turbine, 1-D quasi heat exchanger, and longitudinal vehicle dynamics model were implemented. By using these models, optimal working fluid was determined. Moreover, for practical application, heat exchanger and turbine were designed and optimized. Then, WHRS output power was calculated. In addition, with 1-D engine model and ETM model, transient behavior of the engine at cold start was investigated. Finally, optimal control methods were applied to the overall system to improve fuel economy.

Conclusively remarkable investigations are :

1. In order to use various heat sources with WHRS, the operation condition of the engine should be analyzed precisely. When various heat sources are used, working fluid which can evaporate at low temperature is selected, because charged air and coolant has low temperature compared to exhaust gas. In addition to selection of working fluid, engine operation is limited to use all heat sources because charged air and coolant temperatures are too low to be used as heat sources at low speed region.
2. Selection of working fluid should be considered for cycle efficiency as well as heat sources. In this study, various working fluids were investigated to fine out optimal one. Consequently, water and R245fa showed the best cycle efficiency. R245fa showed higher efficiency than water because the inlet temperature of heat exchanger is lower than that of

water. It means that R245fa can recover more energy from heat source than water. From this, to recover more energy from heat source, it is important to decrease the inlet temperature of working fluid at heat exchanger.

3. Type and size of the heat exchanger were optimized using quasi-1D model. 30.33T type showed the smallest sized and the highest performance compared to other type. The turbine was designed as single stage and multi-stage. Because the turbine operation is limited by choking of working fluid, pressure ratio cannot be increased infinitely. However, high pressure ratio can achieve high cycle efficiency, multi-stage turbine was suggested and designed to overcome choking. Thus, in order to achieve high efficiency of WHRS, multi-stage turbine is required.

4. The maximum efficiency of WHRS is about 30 %, theoretically. However, that goal is difficult to achieve in real implementation because of pressure ratio limitation. Thus, it is obvious that maximum efficiency in real environment is about 10 %. In order to overcome this limitation, it is required to increase pressure ratio with multi-stage turbine or other expander.

5. Simulation to estimate transient state of exhaust gas at cold start was conducted. As results, exhaust gas requires about 80 sec reaches warm-up condition. Therefore, WHRS should be operated at 80 sec after the engine started to ensure general operation.

6. Dynamic Programming was applied to the target system and the optimal operation of the system was obtained. It is notable that the engine operation timing and points of each system showed similar trends. It means that the engine operation of the target system is not changed greatly

compared to the conventional system. Thus, when WHRS for series HEV is designed, the main operation point of the conventional system is considered as target optimization point.

7. ECMS and thermostatic control strategy were adopted in the target system. Two control strategies showed similar fuel economy levels because the engine operating ranges were almost same. Because in series HEV, the engine is decoupled with drive shaft, instantaneous optimal operating point of the engine in ECMS is 80 ~ 100 kW where bfsc values are lower than other operating range.

8. By using WHRS in series HEV, fuel economy can be improve by 6 ~ 10 % in various cycles. As a result of dynamic programming, improvement was greater as engine operating duration increased. The duration of engine operating was more decreased when it is relative long. Because WHRS generated electric energy which should be generated from the engine in the conventional system, engine consumed less fuel with WHRS. Thus, as the duration of the engine operation increased, reduction of that was greater. Consequently, improvement in fuel economy is higher when the engine operating duration is long.

## Bibliography

- [1] H. Teng, G. Regner, and C. Cowland, "Waste heat recovery of heavy-duty diesel engines by organic Rankine cycle part I: hybrid energy system of diesel and Rankine engines," *SAE Paper No. 2007-01-0537*.
- [2] X. Zhang, K. Chau, and C. Chan, "Overview of thermoelectric generation for hybrid vehicles," *Journal of Asian electric vehicles*, vol. 6, pp. 1119-1124, 2008.
- [3] K. M. Saqr, M. K. Mansour, and M. Musa, "Thermal design of automobile exhaust based thermoelectric generators: objectives and challenges," *International journal of automotive technology*, vol. 9, pp. 155-160, 2008.
- [4] K. Ikoma, M. Munekiyo, K. Furuya, M. Kobayashi, T. Izumi, and K. Shinohara, "Thermoelectric module and generator for gasoline engine vehicles," *Thermoelectrics, 1998. Proceedings ICT 98. XVII International Conference on*, 1998, pp. 464-467.
- [5] J. C. Bass, N. Elsner, and F. Leavitt, "Performance of the 1 kW thermoelectric generator for diesel engines," *AIP Conference Proceedings*, 1994, p. 295.
- [6] E. Thacher, B. Helenbrook, M. Karri, and C. J. Richter, "Testing of an automobile exhaust thermoelectric generator in a light truck," *Proceedings of the Institution of Mechanical Engineers, Part D: Journal of Automobile Engineering*, vol. 221, pp. 95-107, 2007.
- [7] M. Algrain, "Controlling an electric turbo compound system for exhaust gas energy recovery in a diesel engine," *Electro Information Technology, 2005 IEEE International Conference on*, 2005, pp. 6 pp.-6.
- [8] L. Eriksson, T. Lindell, O. Leufven, and A. Tomasson, "Scalable Component-Based Modeling for Optimizing Engines with Supercharging, E-Boost and Turbocompound Concepts," *SAE International Journal of Engines*, vol. 5, 2012.

- [9] Y. Ismail, D. Durrieu, P. Menegazzi, P. Chesse, and D. Chalet, "Potential of Exhaust Heat Recovery by Turbocompounding," *SAE Paper No. 2012-01-1603*.
- [10] J. B. Heywood, *Internal Combustion Engine Fundamentals*: McGRAW-HILL, 1988.
- [11] T. Endo, S. Kawajiri, Y. Kojima, K. Takahashi, T. Baba, S. Ibaraki, *et al.*, "Study on Maximizing Exergy in Automotive Engines," *SAE Paper No. 2007-01-0257*.
- [12] M. Kadota and K. Yamamoto, "Advanced transient simulation on hybrid vehicle using Rankine cycle system," *SAE International Journal of Engines*, vol. 1, pp. 240-247, 2009.
- [13] J. Ringler, M. Seifert, V. Guyotot, and W. Hübner, "Rankine Cycle for Waste Heat Recovery of IC Engines," *SAE Paper No. 2009-01-0174*.
- [14] R. E. Chammas and D. Clodic, "Combined Cycle for Hybrid Vehicles," *SAE Paper No. 2005-01-1171*.
- [15] H. Teng, G. Regner, and C. Cowland, "Waste heat recovery of heavy-duty diesel engines by organic Rankine cycle part II: working fluids for WHR-ORC," *SAE Paper No. 2007-01-0543*.
- [16] N. Yamada and M. N. A. Mohamad, "Efficiency of hydrogen internal combustion engine combined with open steam Rankine cycle recovering water and waste heat," *International Journal of Hydrogen Energy*, vol. 35, pp. 1430-1442, 2010.
- [17] S. Aly, "Diesel engine waste-heat power cycle," *Applied energy*, vol. 29, pp. 179-189, 1988.
- [18] S. Hounsham, R. Stobart, A. Cooke, and P. Childs, "Energy Recovery Systems for Engines," *SAE Paper No. 2008-01-0309*.
- [19] M. Talbi and B. Agnew, "Energy recovery from diesel engine exhaust gases for performance enhancement and air conditioning," *Applied Thermal Engineering*, vol. 22, pp. 693-702, 2002.

- [20] C. Katsanos, D. Hountalas, T. Zannis, and E. Yfantis, "Potentiality for Optimizing Operational Performance and Thermal Management of Diesel Truck Engine Rankine Cycle by Recovering Heat in EGR Cooler," *SAE Paper No.* 2010-01-0315.
- [21] P. N. Arunachalam, B. Nyberg, M. Tuner, and P. Tunestal, "A Comparative Analysis of WHR System in HD Engines Using Conventional Diesel Combustion and Partially-Premixed Combustion," *SAE Paper No.* 2012-01-1930.
- [22] A. Boretti, A. Osman, and I. Aris, "Design of Rankine Cycle Systems to Deliver Fuel Economy Benefits over Cold Start Driving Cycles," *SAE Paper No.* 2012-01-1713.
- [23] H. Teng, J. Klaver, T. Park, G. L. Hunter, and B. v. d. Velde, "A Rankine Cycle System for Recovering Waste Heat from HD Diesel Engines - WHR System Development," *SAE Paper No.* 2011-01-1311.
- [24] T. Park, H. Teng, G. L. Hunter, B. v. d. Velde, and J. Klaver, "A Rankine Cycle System for Recovering Waste Heat from HD Diesel Engines - Experimental Results," *SAE Paper No.* 2011-01-1337.
- [25] X. ZHANG, K. ZENG, S. BAI, Y. ZHANG, and M. HE, "Exhaust Recovery of Vehicle Gasoline Engine Based on Organic Rankine Cycle," *SAE Paper No.* 2011-01-1339.
- [26] S. Bae, H. Heo, H. Lee, D. Lee, T. Kim, J. Park, *et al.*, "Performance Characteristics of a Rankine Steam Cycle and Boiler for Engine Waste Heat Recovery," *SAE Paper No.* 2011-28-0055.
- [27] P. N. Arunachalam, M. Shen, M. Tuner, P. Tunestal, and M. Thern, "Waste Heat Recovery from Multiple Heat Sources in a HD Truck Diesel Engine Using a Rankine Cycle - A Theoretical Evaluation," *SAE Paper No.* 2012-01-1602.

- [28] S. Edwards, J. Eitel, E. Pantow, P. Geskes, R. Lutz, and J. Tepas, "Waste Heat Recovery: The Next Challenge for Commercial Vehicle Thermomanagement," *SAE Paper No. 2012-01-1205*.
- [29] G. Latz, S. Andersson, and K. Munch, "Comparison of Working Fluids in Both Subcritical and Supercritical Rankine Cycles for Waste-Heat Recovery Systems in Heavy-Duty Vehicles," *SAE Paper No. 2012-01-1200*.
- [30] *Swash Plate*. Available: <http://www.earlmorse.org/steamboatingpages/steamhappens19/steamhappens19.htm>
- [31] T. Saitoh, N. Yamada, and S.-I. Wakashima, "Solar Rankine cycle system using scroll expander," *Journal of Environment and Engineering*, vol. 2, pp. 708-719, 2007.
- [32] G. Qiu, H. Liu, and S. Riffat, "Expanders for micro-CHP systems with organic Rankine cycle," *Applied Thermal Engineering*, vol. 31, pp. 3301-3307, 2011.
- [33] *Gerotor*. Available: <http://www.starrotor.com/Expanders>
- [34] D. A. Arias, T. A. Shedd, and R. K. Jester, "Theoretical Analysis of Waste Heat Recovery from an Internal Combustion Engine in a Hybrid Vehicle," *SAE Paper No. 2006-01-1605*.
- [35] S. Mavridou, G. Mavropoulos, D. Bouris, D. Hountalas, and G. Bergeles, "Comparative design study of a diesel exhaust gas heat exchanger for truck applications with conventional and state of the art heat transfer enhancements," *Applied Thermal Engineering*, vol. 30, pp. 935-947, 2010.
- [36] J. Lopes, R. Douglas, G. McCullough, R. O'Shaughnessy, A. Hanna, C. Rouaud, *et al.*, "Review of Rankine Cycle Systems Components for Hybrid Engines Waste Heat Recovery," *SAE Paper No. 2012-01-1942*.
- [37] S. H. Kang and D. H. Chung, "Design and Experimental Study of Organic Rankine Cycle (ORC) and Radial Turbine," *ASME 2011 Turbo Expo: Turbine Technical Conference and Exposition*, 2011.

- [38] W. Yagoub, P. Doherty, and S. Riffat, "Solar energy-gas driven micro-CHP system for an office building," *Applied thermal engineering*, vol. 26, pp. 1604-1610, 2006.
- [39] T. Yamamoto, T. Furuhashi, N. Arai, and K. Mori, "Design and testing of the organic Rankine cycle," *Energy*, vol. 26, pp. 239-251, 2001.
- [40] M. Mohd, N. Y. Tahir, and T. Hoshino, "Efficiency of Compact Organic Rankine Cycle System with Rotary-Vane-Type Expander for Low-Temperature Waste Heat Recovery," *International Journal of Environmental Science And Engineering*, vol. 2, pp. 11-16, 2010.
- [41] D. Mikielewicz, J. Mikielewicz, J. Wajs, and E. Ichnatowicz, "EXPERIENCES FROM OPERATION OF DIFFERENT EXPANSION DEVICES IN DOMESTIC MICRO ORC," *First International Seminar on ORC Power Systems*, 2011.
- [42] J. A. Mathias, J. R. Johnston Jr, J. Cao, D. K. Priedeman, and R. N. Christensen, "Experimental testing of gerotor and scroll expanders used in, and energetic and exergetic modeling of, an organic Rankine cycle," *Journal of Energy Resources Technology*, vol. 131, p. 012201, 2009.
- [43] V. Lemort, S. Quoilin, C. Cuevas, and J. Lebrun, "Testing and modeling a scroll expander integrated into an Organic Rankine Cycle," *Applied Thermal Engineering*, vol. 29, pp. 3094-3102, 2009.
- [44] R. Peterson, H. Wang, and T. Herron, "Performance of a small-scale regenerative Rankine power cycle employing a scroll expander," *Proceedings of the Institution of Mechanical Engineers, Part A: Journal of Power and Energy*, vol. 222, pp. 271-282, 2008.
- [45] K. J. Harada, "Development of a small scale scroll expander," M.S., Mechanical Engineering, Oregon State University, 2010.
- [46] D. Manolakos, G. Kosmadakis, S. Kyritsis, and G. Papadakis, "Identification of behaviour and evaluation of performance of small scale, low-temperature

- Organic Rankine Cycle system coupled with a RO desalination unit," *Energy*, vol. 34, pp. 767-774, 2009.
- [47] H. Kim, J. Ahn, I. Park, and P. Rha, "Scroll expander for power generation from a low-grade steam source," *Proceedings of the Institution of Mechanical Engineers, Part A: Journal of Power and Energy*, vol. 221, pp. 705-711, 2007.
- [48] H. Kim and J. Yu, "DESIGN OF A SCROLL EXPANDER FOR AN ORC APPLICABLE TO A PASSENGER CAR FOR FUEL CONSUMPTION IMPROVEMENT," *First International Seminar on ORC Power Systems*, 2011.
- [49] M. Orosz, "Comparison of scroll and piston expanders for small scale ORC applications," *First International Seminar on ORC Power Systems*, 2011.
- [50] S. Declaye, S. Quoilin, and V. Lemort, "Development of a waste heat recovery ORC prototype using an oil-free scroll expander," *First International Seminar on ORC Power Systems*.
- [51] S. T. Ro, *Engineering Thermodynamics*, 4 ed. Korea: Moonundang, 2008.
- [52] *IFP Engine Library Rev 11 User`s guide*: LMS IMAGINE, 2011.
- [53] M. Metghalchi and J. C. Keck, "Burning velocities of mixtures of air with methanol, isooctane, and indolene at high pressure and temperature," *Combustion and Flame*, vol. 48, pp. 191-210, 1982.
- [54] M. Boger, D. Veynante, H. Boughanem, and A. Trouvé, "Direct numerical simulation analysis of flame surface density concept for large eddy simulation of turbulent premixed combustion," *Symposium (International) on Combustion*, 1998, pp. 917-925.
- [55] *Thermal Library Rev 11 User`s guide*: LMS IMAGINE, 2011.
- [56] *Thermal Hydraulic Library Rev 11 User`s guide*: LMS IMAGINE, 2011.
- [57] H. Kang, "A study on the smart cooling system of the double loop coolant structure of a deisel engine with thermal management modeling," M.S., The school of mechanical and merospace engineering, Seoul National University, Korea, 2013.

- [58] T. K. Lee, Y. Kim, A. Stefanopoulou, and Z. S. Filipi, "Hybrid electric vehicle supervisory control design reflecting estimated lithium-ion battery electrochemical dynamics," *American Control Conference, 2011*, 2011, pp. 388-395.
- [59] D. Di Domenico, A. Stefanopoulou, and G. Fiengo, "Lithium-ion battery state of charge and critical surface charge estimation using an electrochemical model-based extended Kalman filter," *Journal of dynamic systems, measurement, and control*, vol. 132, 2010.
- [60] K. Smith and C. Y. Wang, "Solid-state diffusion limitations on pulse operation of a lithium ion cell for hybrid electric vehicles," *Journal of power sources*, vol. 161, pp. 628-639, 2006.
- [61] W. M. Kays and A. L. London, "Compact heat exchangers," 1984.
- [62] J. C. Chen, "Correlation for boiling heat transfer to saturated fluids in convective flow," *Industrial & Engineering Chemistry Process Design and Development*, vol. 5, pp. 322-329, 1966.
- [63] D. G. Wilson, "Design of high-efficiency turbomachinery and gas turbines," 1984.
- [64] Y. Gao, L. Chen, and M. Ehsani, "Investigation of the Effectiveness of Regenerative Braking for EV and HEV," *SAE Paper No. 1999-01-2910*.
- [65] H. Kim, "Design, Manufacture and Performance Test of Radial Turbine for an Organic Rankin Cycle," M.S., The school of mechanical and aerospace engineering, Seoul National university, Korea, 2010.
- [66] D. Kirk, "Optimal Control Theory An Introduction," ed: Prentice-Hall, 1970.
- [67] N. Kim, "Energy management strategy for hybrid electric vehicles based on Pontryagin's Minimum Principle," Ph.D., The school of mechanical and aerospace engineering, Seoul National University, Korea, 2009.
- [68] P. Rodatz, G. Paganelli, A. Sciarretta, and L. Guzzella, "Optimal power management of an experimental fuel cell/supercapacitor-powered hybrid vehicle," *Control Engineering Practice*, vol. 13, pp. 41-53, 2005.

- [69] G. Paganelli and Y. Guezennec, "Optimizing control strategy for hybrid fuel cell vehicle," *SAE Paper No. 2002-01-0102*.
- [70] G. Paganelli, T. Guerra, S. Delprat, J. Santin, M. Delhom, and E. Combes, "Simulation and assessment of power control strategies for a parallel hybrid car," *Proceedings of the Institution of Mechanical Engineers, Part D: Journal of Automobile Engineering*, vol. 214, pp. 705-717, 2000.
- [71] *Emission Test Cycle*. Available: [www.dieselnet.com/standards/cycle](http://www.dieselnet.com/standards/cycle)

## 초 록

최근 원유 가격의 지속적인 상승과 강력한 배기 규제가 자동차 산업에서 큰 화두가 되고 있다. 따라서, 배기 배출을 줄이고 높은 연비를 달성하기 위하여 많은 노력이 이루어 지고 있다. 하지만, 내연 기관이나 하이브리드 시스템과 같은 기존의 파워트레인 시스템으로는 효율을 높이는데 한계가 존재한다. 이러한 기존 파워트레인의 경우 최대 40 % 의 연료 에너지만이 차량을 구동하는데 쓰이고, 60 % 에 이르는 에너지는 냉각수나 배기가스로 손실되기 때문이다. 따라서, 손실되는 60 % 의 에너지를 추가로 사용하지 않는 이상, 더 높은 연료 변환 효율을 얻는 것은 거의 불가능 하다. 이러한 손실 에너지, 즉 버려지는 에너지를 회수하여 차량을 구동하거나 추가적인 전기 에너지를 얻는 기술을 폐열 회수 시스템이라 한다. 본 논문에서는 Rankine Cycle 을 폐열 회수 시스템으로 사용하였으며, 이를 시리즈 하이브리드 차량에 적용하여 연비를 높이는 연구를 진행하였다.

첫째로 다양한 열원에 대한 열역학적 분석을 수행하였다. 본 연구에서 분석 대상으로 고려한 열원은 배기가스, 냉각수, 압축 공기이다. 열역학적 분석을 통하여, 각 열원의 엔진 작동점에 따른 엑서지와 가용에너지를 분석하였다. 이러한 분석을 기반으로 폐열 회수 시스템을 설계하기 위한 기준을 얻을 수 있었다. 또한 각 열원이 폐열 회수 장치에 적용되기 위한 엔진 작동 조건을 분석 하였다.

두번째로 대상 시리즈 하이브리드 자동차에 폐열 회수 장치를 적용하기 위한 최적화를 진행하였다. 최적화는 설계와 제어에 대하여 진행하였다. 시스템 효율 분석을 통하여 최적 작동 유체를 선정 하였으며, 터빈을 작동 조건과 제한 조건을 고려하여 설계하였다. 또한 열교환기의 기하학적 구조와 크기를 최적화 하였다. 제어 알고리즘을 최적화 하기 위하여 전역 최적화 방법인 Dynamic

Programming 과 지역 최적화 방법인 Equivalent Consumption Minimization Strategy 를 적용하였다.

마지막으로 냉간 상태에서 배기가스의 상태는 폐열 회수 장치를 작동 시키기 위하여 꼭 알아야 할 조건이다. 이를 위하여 1-D 엔진 모델과 Engine Thermal Management 모델을 이용하여 과도 상태를 예측하였다. 이를 기반으로 엔진 시동 후 80 초 후에 폐열 회수 장치를 작동시켜야 한다는 것을 알 수 있었다.

이러한 연구를 수행함으로써 폐열 회수 장치를 차량에 적용하기 위한 설계 과정을 제시할 수 있었다. 또한 폐열 회수 장치를 적용을 위한 기본 구성의 최적화와 전체 시스템 운용을 위한 제어 최적화에 대한 방법을 제시 할 수 있었다. 또한 본 연구를 기반으로 다양한 동력원을 조합하여 새로운 에너지 시스템을 설계 할 경우, 설계 과정 및 방법, 최적화 기법 등을 적용할 수 있을 것이라 기대된다.

주요어 : 폐열 회수 시스템 (WHRS), 유기 랭킨 사이클 (ORC), 최적 제어, 최적화, 대형 직렬형 하이브리드 전기 자동차 (HSHEV)

학번 : 2007-20848